ABSTRACT

Title of dissertation: MAGNETIC ISLANDS IN THE HELIOSHEATH: PROPERTIES AND IMPLICATIONS

Kevin Schoeffler, Doctor of Philosophy, 2012

Dissertation directed by: Professor James F. Drake
Department of Physics

In the heliosheath there are sectors of magnetic fields separated by current sheets thinner than the ion inertial length and thus subject to the tearing instability. This instability allows the development of magnetic islands that grow due to magnetic reconnection. Using PIC (particle-in-cell) simulations, we show that these islands are relevant because they quickly grow to fill up the space between the sectors and in the meanwhile generate temperature anisotropies, accelerate particles, and form instabilities based on the anisotropies. The plasma β (the ratio of the plasma pressure to the magnetic pressure) of a system can have a large effect on its dynamics since high β enhances the effects of pressure anisotropies. In our PIC simulations, we investigate a system of stacked current sheets that break up into magnetic islands due to magnetic reconnection, which is analogous to the compressed heliospheric current sheet in the heliosheath. We find that for high β, and for realistic ion-to-electron mass ratios, only highly elongated islands reach finite size. The anisotropy within these islands prevents full contraction, leading to a final state of highly elongated islands in which further reconnection is suppressed.

In the heliosheath there is evidence that these elongated islands are present. We performing a scaling of the growth of magnetic islands versus the system size. We thus determine that the islands, although reaching a final elongated state, can continue growing via the merging process until they reach the sector width. The islands achieve this size in much less time than it takes for the islands to convect through the heliosheath. We also find that the electron heating in our simulations has a strong β dependence. Particles are dominantly heated through Fermi reflection in contracting islands during island growth and merging. However, electron anisotropies support the development of a Weibel instability which impedes the Fermi acceleration of the electrons. In the heliosheath, we predict that energization of particles in general is limited by interaction with anisotropy instabilities such as the firehose instability, and by the the Weibel instability for electrons in particular.

MAGNETIC ISLANDS IN THE HELIOSHEATH: PROPERTIES AND IMPLICATIONS

by

Kevin Michael Schoeffler

Dissertation submitted to the Faculty of the Graduate School of the
University of Maryland, College Park in partial fulfillment
of the requirements for the degree of
Doctor of Philosophy
2012

Advisory Committee:
Professor James F. Drake, Chair/Advisor
Dr. Michael M. Swisdak, Co-Advisor
Professor William D. Dorland
Professor Adil B. Hassam
Professor Eve C. Ostriker

Dedication

To my Dad.

One more step in me asking that familiar question:

“What if you had a magnet ... ?”

Acknowledgments

I am grateful to Jim Drake who helped me find out that I wanted to pursue a PhD in plasma physics and it was a pleasure working with him throughout the whole process. I am also grateful to Marc Swisdak who was always there to help answer questions. I would like to thank Adil Hassam who inspired me in my undergraduate math methods class to begin my studies in plasma physics, and Bill Dorland who got me started doing plasma physics research as an undergrad. I would also like to thank Eve Ostriker for letting me sit in on her radiation class. I would like to thank of of these people for taking the time to serve as my comittee for my thesis. I would also like to thank Mike Shay who helped me get started working on all the simulations that I do when I began working for Jim.

I would like to thank all my officemates past and present, who were all a valuable resource both in providing discussion and ideas on research as well as creating an office that was enjoyable for work and life in general. I would like to thank Paul Cassak, Muralidhar Yeddula, Haihong Che, Yi-Hsin Liu, Ray Fermo, Sanjeev Chauhan, Joel Dahlin, Lora McMurtrie, and Wrick Sengupta. Along with Tak Chu Li my academic sister who never ended up sharing and office with me.

I am also would like to thank all my housemates at IHoP (international house of physics), Jupiter Bagaipo, Prateek Agrawal, Kaushik Mitra, Dinko Ferenček and Zrinka Gregurić-Ferenček, Yiğit Subaşı and Shannon Brown, and the most recent Juraj Radic and Kanu Sinha. Each of them helped enrich my experience as a grad student at Maryland by supporting me throughout my time here, and making sure

that my time at home was always an enjoyable experience, even if it involved us being slacker(er)s.

I would also like to thank all my family especially my mom Jeanne, my dad Fred, and my brother Eric. They were there supporting me before my 11 years at University began, and they continue as I move on to new exciting chapters of my life.

There are many more people who throughout my time at Maryland have helped me to succeed and inspired me to continue with my work, including all my other previous roomates, friends from the Catholic Student Center, friends from graduate bible studies, friends from Communion and Liberation, and friends from conferences and meetings such as SHINE, and AGU. I would like to thank them all although there are too many to list here.

Table of Contents

List of Figures

List of Abbreviations

β	Plasma Beta (ratio of plasma pressure to magnetic pressure)
n	Particle Density
T	Temperature
P	Pressure
$\mathbb{P}$	Pressure Tensor
$\mathbf{B}$	Magnetic field
$\mathbf{E}$	Electric field
$\mathbf{v}$	Plasma Flow Velocity
$\mathbf{j}$	Current Density
m_e	Electron Mass
e	Elementary Charge
c	Speed of Light
d_i	Ion Inertial Length
c_A	Alfvén Speed
Ω_{ci}	Ion Cyclotron Frequency
ω_{pi}	Ion Plasma Frequency
S	Lundquist Number
k	Wave Number
γ	Growth Rate
η	Resistivity

ACR	Anomalous Cosmic Ray
AU	Astronomical Unit (distance from the Earth to the Sun)
FTE	Flux Tranfer Events
HCS	Heliospheric Current Sheet
HP	Heliopause
ISM	Interstellar Medium
ISEE	International Sun-Earth Explorer (spacecraft)
IMF	Interplanetary Magnetic Field
MHD	Magnetohydrodynamics
MRI	Magnetorotational Instability
PIC	Paritcle-in-cell
PUI	Pick-up Ion
SAD	Supra-arcade Downflows
SDO	Solar Dynamics Observatory (spacecraft)
TCR	Travelling Compression Region
TRACE	Transition Region and Coronal Explorer (spacecraft)
TS	Termination Shock

Chapter 1

The Heliosheath

At the outer edges of the solar system, plasma ejected from the sun, known as the solar wind, encounters extrasolar plasma, known as the interstellar medium (ISM). Before reaching the ISM the solar wind forms a shock known as the termination shock (TS). Beyond this shock is the region known as the heliosheath (See Figure 1.1).

In 1977 the spacecraft, Voyager 1 was launched into space with the primary objective to investigate Jupiter and Saturn. It set out flying by the planets, and some of their moons. After several years of fascinating photographs, including the rings of Saturn, it passed the orbits of Neptune and Pluto. There were no more planets left to see. Voyager 1 was now entering the vastness of empty space, relying on particle detectors, magnetometers, and plasma detectors, to see mostly the same signatures for many years. In 1990 Voyager 1 took one last look at Earth from its far away vantage point while entering the abyss. At this point, a photo was taken famously referred to by Carl Sagan as the "Pale Blue Dot." Voyager 2 followed in the footsteps of Voyager 1, and was able to investigate Uranus and Neptune as well, only to meet a similar fate.

In 2004, Voyager 1 encountered the TS [65], fulfilling predictions of theory. After decades of flying through space, it continued to send back data containing

vastly different signatures than previous data. In 2007 Voyager 2 joined in the excitement [9]. Some of the long held theories did not hold up to expectations when put to the test of reality with the new data from the two spacecraft. For example, it was predicted that the anomalous cosmic rays (ACRs), energetic particles $\sim 10-100$MeV, thought to be generated by acceleration at the TS, would peak at the TS. Now there was new data showing otherwise [65]. There are other examples where data confirmed predicted results [70]. The flow has been shown to be supersonic downstream of the TS [47] with respect to the thermal ions, because there is an additional population of pick-up ions (PUIs) that contributes to the sound speed[1]. With all of these new data both predicted and not predicted by theory, it is a particularly exciting time to discover new theories that might help us model and understand the outer edges of the solar system.

It has been predicted that the mostly laminar magnetic field carried along with the solar wind, after entering the heliosheath, begins to break up into a turbulent mix of so called "magnetic islands" [15, 41, 11]. The description of the reversed magnetic fields, and associated currents between them, which are required for the development of islands, will be described in a later section. Unlike the laminar magnetic field that can be traced back to the "mainland" of the sun, the magnetic fields of the islands are largely separated, much like islands in the sea. Throughout this thesis we will examine this break up due to a process known as magnetic reconnec-

[1]PUIs are generated when neutral atoms from the interstellar medium, which are unaffected by magnetic fields, are ionized and then "picked up" by the solar wind. This process generates a large velocity perpendicular to the magnetic field, giving a thermal energy of around 1keV.

tion, and how anisotropic velocity distributions contribute to the dynamics of these islands. We will look at computer simulations that help us understand more about these heliospheric magnetic islands in terms of their shape, rate of growth, and how they can accelerate particles. Chapters 4-6 are modified versions of papers either published [52, 53], or in press.

1.1 The solar wind and the heliosphere

Before 1951 it was thought that interplanetary space was a vacuum save for isolated clouds of plasma [1]. In 1951, Biermann showed that there is a tail associated with comets which always faces in the direction away from the sun, and claimed that the cause of this tail was a stream of charged particles coming from the sun, which we now call the solar wind [5]. By 1958 this concept of the solar wind was still not well regarded when Parker published a paper further developing the theory [43].

Parker considered different steady state solutions to a spherical symmetric plasma density distribution extending from near the surface of the sun to infinity. It happened that the only solution with a reasonable pressure at infinity also included a radial outflow of plasma. This radial outflow accelerated up to a constant speed at large radii.

Satellite measurements confirmed the existence of the solar wind and have identified a wide variety of dynamics ranging from large scale shocks from coronal mass ejections to small amplitude waves that heat the expanding plasma. Near Earth, at 1AU from the sun, the density is on the order of $1 - 10\text{cm}^{-3}$, with a

magnetic field on the order of $1-20$nT, and a velocity ranging from $300-1000$km/s. This density is a factor of 10^{-19} as dense as air, and the magnetic field is 10^{-6} as strong as a typical kitchen magnet. Although these numbers are very small, at large distance scales they play a significant role. When the solar wind reaches the heliosheath, the density and magnetic field drop to even smaller values; a factor of 1000 in density, and 10 in magnetic field.

The solar wind is not the only plasma in space. Between the stars are clouds of plasma generated from various astrophysical phenomenon. The matter found out between the stars is referred to as the interstellar medium (ISM). The solar wind carves out a bubble inside the local cloud in which the sun is located. This bubble is referred to as the heliosphere. The boundary between the heliosphere and the ISM is known as the heliopause.

Since the solar wind tends to blow radially outward at around 400km/s which is large compared to the sound speed of around 100km/s near 100AU, the plasma was predicted to form a shock before reaching the heliopause. This shock is referred to as the termination shock (TS), and was directly observed by both Voyager spacecraft [47].

It is possible that there is another shock formed by the relative motion of the heliosphere and the ISM. This shock is the heliospheric bow shock. Figure 1.1 is a cartoon showing each of these features: the heliosphere, heliopause, TS, heliosheath, ISM, and the bow shock. The figure also shows the trajectories of the two Voyager spacecraft which have been making in situ measurements of the heliosheath, and are now approaching the heliopause.

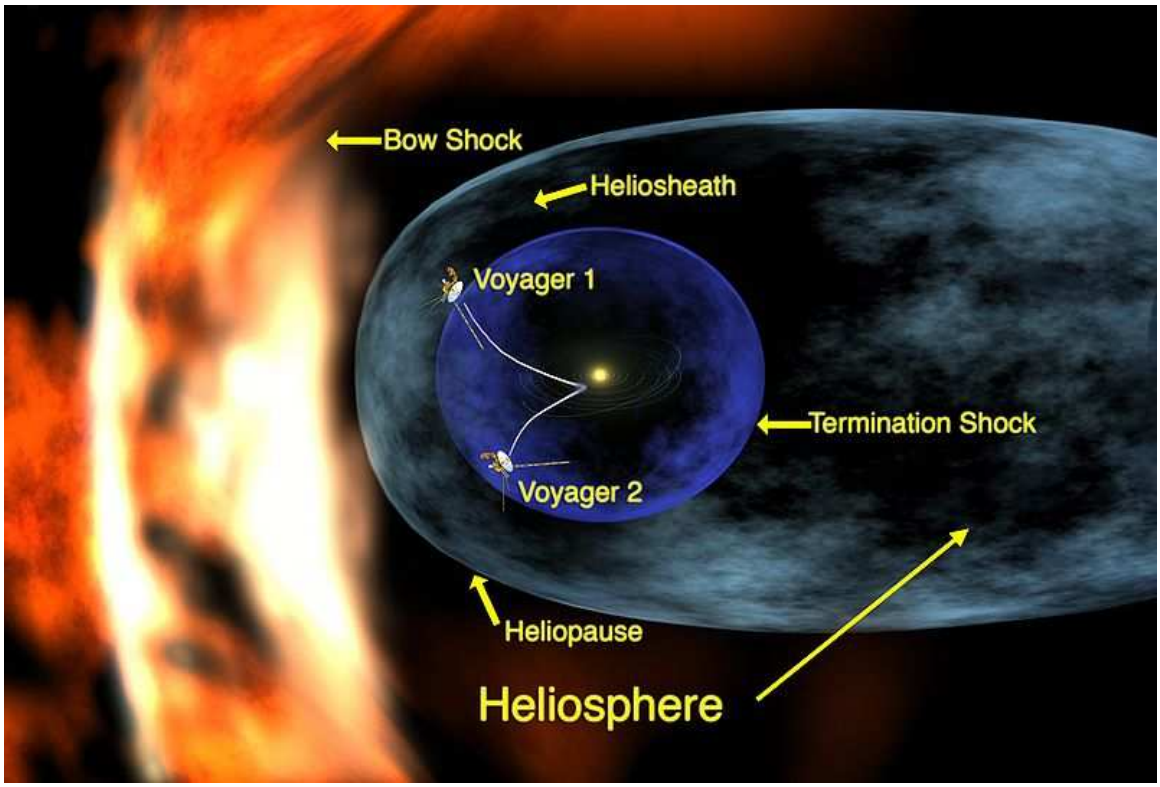

Figure 1.1: Cartoon picture of the heliosphere pointing out the heliopause, TS, heliosheath, ISM, and bow shock. The trajectories of Voyager 1 and 2 are also included. (image from NASA, courtesy of Walt Feimer)

The exact shape of the heliosphere remains unknown, but it is predicted that the magnetic field pressure, in addition to the ram pressure, of the ISM determines the shape. The heliosheath becomes elongated along the direction of the magnetic field [40]. Nevertheless it is still predicted that there is a tail as suggested in Figure 1.1. Regardless of the shape of the heliosphere, there is a region in between the TS and the heliopause known as the heliosheath which is the location of interest for this thesis.

1.2 The Parker spiral

So far we have only considered plasma flowing radially outward from the sun. In addition to this general concept of the solar wind, there are other important considerations. Namely, there is a magnetic field associated with the solar wind plasma that plays an essential role in the dynamics of reconnection and island formation, which will be outlined in the following chapters. The rotation of the sun causes the field to form a spiral structure, referred to as the Parker Spiral.

The magnetic field of the sun is said to be "frozen-in" to the plasma ejected from the solar surface. Due to the low resistivity and large spacial scales of the heliosphere, the magnetic flux that goes through a fluid element will remain constant as the fluid element propagates through space. A derivation of this frozen-in condition can be found in Appendix A. Because the flux is conserved, it is convenient to consider the magnetic field as a physical entity that moves along with the plasma, although it is important to keep in mind that the frozen-in condition must

be satisfied for this picture to hold.

The sun has an associated magnetic field which to first order can be approximated as a dipole. Like the Earth, the sun rotates around an axis. As the solar wind moves away from the sun it drags out magnetic fields with it, and these magnetic fields get wrapped around the sun as it rotates, generating spiral magnetic fields which point in opposite directions above and below the equatorial plane. Since the magnetic field at the equator of the sun currently points southward (i.e. the direction opposite to the axis of revolution of the planetary bodies), this implies clockwise fields (as viewed from the north) in the northern hemisphere and counterclockwise in the south. This concept of the spiral magnetic field was predicted in [43].

In Parker's paper he considers the very simple model of spherically symmetric outflow and takes a latitudinal cut at $\theta = \theta_0$, which has magnetic fields attached to the sun that go out to infinity. In this simple model, there is a steady state solution in the frame of rotation of the sun at frequency ω. Parker assumes a velocity profile of.

$$v_r = v_m, \quad v_\theta = 0, \quad v_\phi = \omega(r - b)\sin(\theta) \tag{1.1}$$

The radial velocity, v_r, is a constant, v_m, as predicted for the solar wind without magnetic fields. The azimuthal velocity, v_ϕ, is $\omega r \sin(\theta)$ since we are in the rotating frame plus the added constraint that the azimuthal velocity goes to zero at a location $r = b$ where the solar wind leaves the influence of gravitational forces as well as acceleration due to the hot corona. If you look at the equator, the outflow follows

streamlines given by the following equation after integrating the velocity profiles.

$$\frac{r}{b} - 1 - \ln\left(\frac{r}{b}\right) = \frac{v_m}{b\omega}\left(\phi - \phi_0\right) \tag{1.2}$$

For latitudes above or below the equator, $\theta > \pi/2$ and $\theta < \pi/2$, the magnetic fields either go into or out of the sun. For simplicity Parker looks at the equator, which gives qualitatively similar results to other latitudes. Since in the rotating frame the fields are anchored to the sun, and the plasma is frozen into the fields, the magnetic fields must be aligned with the streamlines of the velocity.

Figure 1.2 shows the streamlines described in Equation (1.2), which are also the magnetic field lines. In the non-rotating reference frame the spiral pattern spins transporting the solar wind radially outward at the speed v_m.

1.3 Sectored magnetic fields

The change in direction of the magnetic fields above and below the ecliptic plane must be accompanied by a electric current. This current is found in the solar wind and is referred to as the heliospheric current sheet (HCS). The solar axis of rotation and axis of the dipolar magnetic field are not aligned, which causes the HCS to flap in and out of the equatorial plane. In regions of low latitude, the magnetic field alternates between sectors of the northern clockwise magnetic field and southern counterclockwise magnetic field (at the current orientation of the solar magnetic field) [64].

A cartoon representation of the HCS is shown in Figure 1.3, and shows it sinusoidally oscillating in the radial direction. In reality, the sectors are not as regular

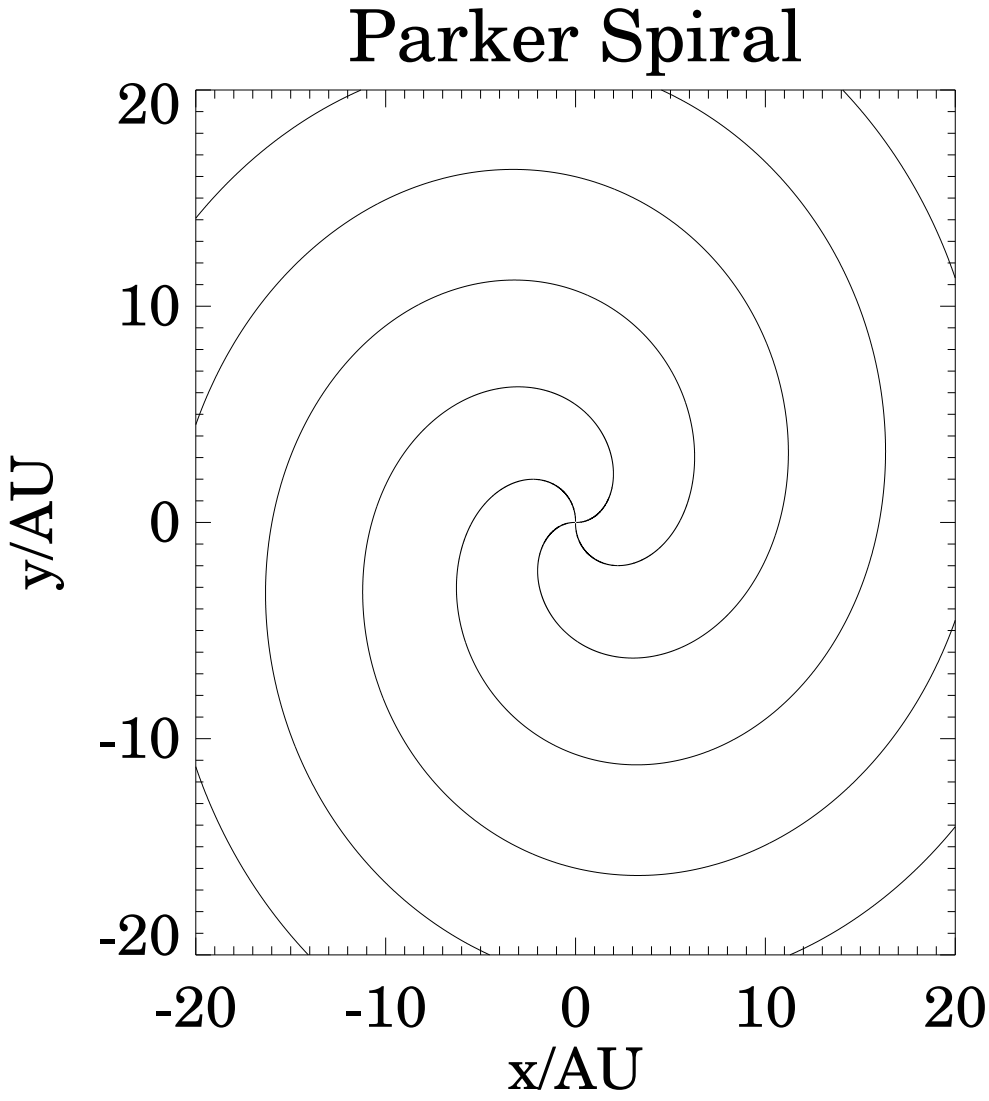

Figure 1.2: The Parker spiral viewed in the ecliptic plane. The lines are streamlines of the plasma flow, or alternatively magnetic field lines in the frame of rotation of the sun. These field lines are determined using the model described in Parker's paper that coined the term solar wind.

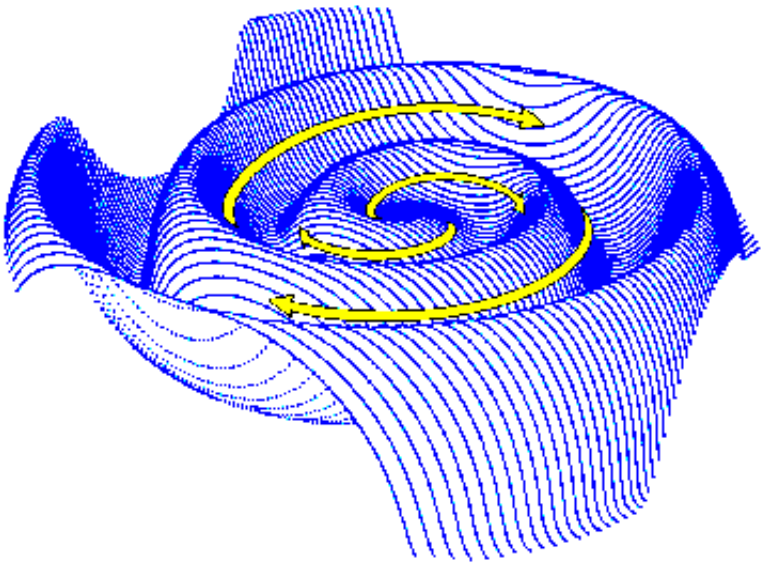

Figure 1.3: 3D cartoon of the HCS taking into account the discrepancy between the axis of rotation, and the axis of the dipolar magnetic field. The yellow arrows represent the direction of the magnetic field above the HCS. (image from NASA courtesy of J. Jokipii, University of Arizona)

in length, but they continue to exist throughout the heliosphere. The sectored fields are found near the equatorial plane but extend out to a significant latitudinal extent. The magnetic dipole of the sun switches directions roughly every 11 years. This periodic behavior is known as the solar cycle. The latitudinal extent of the sectored fields becomes largest while the dipole switches signs.

When the sectored fields separated by the HCS pass through the TS, the HCS thickness is compressed, and is further compressed as the solar wind velocity slows on its approach to the HP. This leads to conditions where the frozen-in condition is violated, and interesting physics, including magnetic reconnection and the formation of magnetic islands, is predicted to occur. These conditions and physical processes will be discussed in the next chapter. The computational work described throughout this thesis is inspired by this configuration found in the heliosheath.

Sectored magnetic fields, are not unique to the solar system. Any magnetized star with a stellar wind could potentially have them, as long as they have a magnetic axis, μ, which is not the same as the rotational axis, Ω. One system where sectored fields are predicted is in pulsar winds. A pulsar is a rapidly rotating neutron star which has a beam of radiation aligned with its magnetic axis.

Pulsars, analogous to the sun, can have a wind which allows the development of sectors of oppositely directed magnetic fields. These sectored pulsar winds are more commonly referred to as striped pulsar winds [62]. Figure 1.4 shows a picture of these striped pulsar winds, which is an equally valid description for the sectored fields of the solar wind.

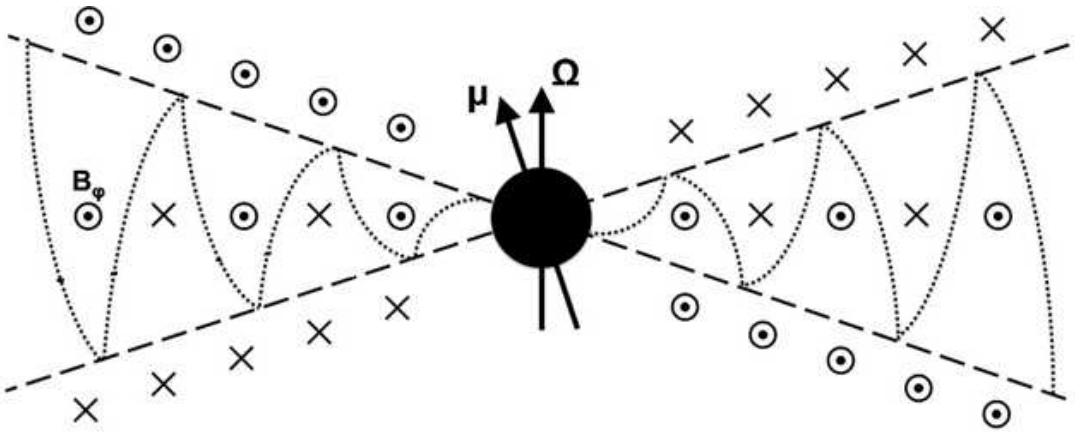

Figure 1.4: A cartoon of the magnetic field configuration in a striped pulsar wind. The dotted line is analogous to the HCS. The magnetic fields point inward above this line, and outward below it. μ represents the magnetic axis, while Ω represents the rotational axis. B_ϕ is the out of plane field. (Adapted with permission from Ref. [Sironi et al. (2011)] by the American Astronomical Society)

1.4 PUIs and plasma beta

Pick-up ions (PUIs) play an important role in the heliosheath and the development of reconnection. Throughout the heliosphere neutral ions are ionized and subsequently picked up by the solar wind and carried towards the heliosheath. Close to the sun the ions are generated mostly by photo-ionization. After 1AU charge exchange with solar wind ions dominates.

The density of PUIs increases with distance from the sun, while the density of cold solar wind ions drops with distance. At the heliosheath, the pressure is dominated by these PUIs. Although the cold solar wind density is still larger than the PUI density, the $\sim$ 1keV PUIs generate significantly more pressure than the

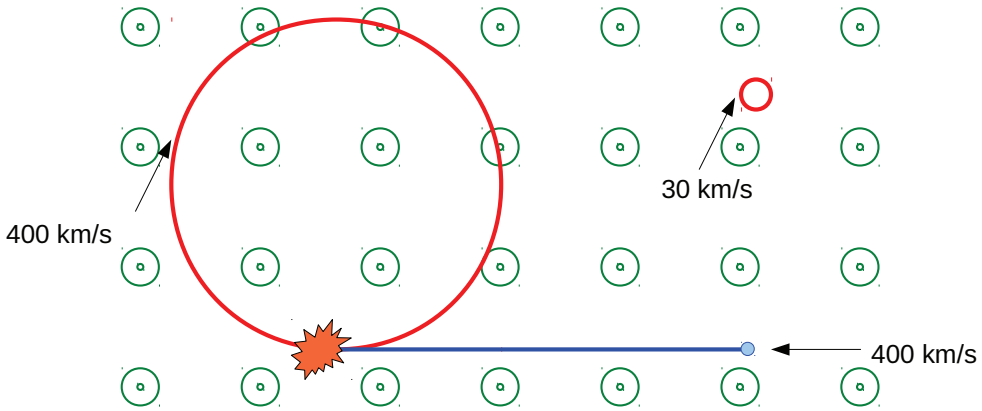

Figure 1.5: Picture in the solar wind frame of the trajectory of a neutral atom (blue), which is ionized and follows the new PUI trajectory (red). The green circles represent magnetic field lines coming out of the page. The small red circle is a cold solar wind ion trajectory.

$\sim$ 10eV solar wind ions.

In the solar rest frame the neutral atoms have a small velocity $\sim$ 25km/s. However in the rest frame of the solar wind, the neutral atoms are moving at the solar wind speed, $\sim$ 400km/s. After the atoms become ionized, they begin to orbit around the magnetic fields. This process can be seen in Figure 1.5 where the blue neutral atom, is picked up by the magnetic field after ionization. The new PUI

trajectory (red) has a circular orbit. The energy of the PUIs is much more than the cold solar wind ions.

An important parameter that determines the dynamics of the plasma in the heliosheath is the plasma beta,

$$\beta = \frac{8\pi P}{B^2}, \tag{1.3}$$

which is the ratio of the plasma pressure to the magnetic pressure. Due to the PUI population and its influence on the pressure, it is expected that β can be as large as 10 just past the TS. This means that the magnetic field does not dominate the dynamics, but rather that the pressure tensor, $\mathbb{P}$, described in Chapter 3 does. Many of the simulations performed during the work of this thesis investigate how these large values of β affect the dynamics of reconnection and island formation.

Although this work focuses on the development of magnetic islands in the heliosheath, the dynamics of island growth and interaction in any high β system should be similar. A relevant example of a high β system in nature is in accretion discs. Accretion discs are clouds of gas that orbit a compact object, such as a neutron star or black hole.

In order for the gas to accrete into the compact object, it must first shed angular momentum. Since most of these discs are nearly collisionless there is no significant viscosity to do this. However, most of these accretion discs have a population of ionized gas, and are subject to an instability known as the magnetorotational instability (MRI) [2]. The MRI uses small magnetic fields to transfer angular momentum outward. The gravitational energy lost as the plasma accretes inward

is converted into magnetic fields. The MRI thus generates a turbulent mixture of magnetic fields that can reconnect, form islands, and release magnetic energy in the form of heat and kinetic energy.

Chapter 2

Magnetic Reconnection and Magnetic Islands

In the heliosheath, the HCS is compressed to small scales. The conditions are right for the development of magnetic islands, and the process known as magnetic reconnection. Magnetic reconnection converts magnetic energy, such as that found in the sectored fields of the solar wind, into bulk flows, and the heating and acceleration of particles. In the process of reconnection, the large scale sectored magnetic fields separate into many individual magnetic islands.

2.1 Breaking the frozen-in condition

One requirement for reconnection to occur is that the frozen-in condition be violated. The frozen-in condition is derived based on the assumption that

$$\mathbf{E} = -\frac{\mathbf{v} \times \mathbf{B}}{c}, \tag{2.1}$$

where the electric field, $\mathbf{E}$, is expressed as a function of the flow velocity, $\mathbf{v}$, the magnetic field, $\mathbf{B}$, and the speed of light, c.

The full equation for the electric field, including resistivity, finite mass ratio effects, and non-Maxwellian particle distributions can be derived from the electron fluid equation of motion as follows:

$$\mathbf{E} = -\frac{\mathbf{v} \times \mathbf{B}}{c} + \frac{1}{nec}\mathbf{j} \times \mathbf{B} - \frac{1}{ne}\nabla \cdot \mathbb{P}_\mathbf{e} + \frac{m_e}{e^2}\frac{d\,\mathbf{j}/n}{dt} + \eta\,\mathbf{j}, \tag{2.2}$$

where we use the following additional symbols: the particle density, n, elementary charge, e, current density, $\mathbf{j}$, the resistivity, η, and the electron mass, m_e. $\mathbb{P}_\mathbf{e}$ is the electron pressure tensor, and is described in more detail in the next chapter.

In many circumstances the additional terms that are found in this equation beyond that shown in Equation (2.1) are small and thus the frozen-in condition is satisfied. However, for tearing the frozen-in condition must be violated, and hence these terms are important.

The four new terms are known as the Hall term, the pressure term, the inertial term, and the resistive dissipation term, respectively. Each of the last three terms can potentially break the frozen-in condition.

Although it seems that it might break the frozen-in condition, the Hall term can be absorbed into the second term transforming the $\mathbf{v}$ from the bulk motion of the ions, to the bulk motion of the electrons. The ions may not be frozen-in to the magnetic fields, but the electrons remain frozen-in.

2.2 Tearing instability

When there is a sharp change in the direction of magnetic fields over a short distance, which results in a thin but intense current sheet, an instability can develop that converts the energy in the magnetic fields into heat, and bulk flows. This instability is known as the tearing instability, and is the beginning of magnetic reconnection. Later in this section we will consider at what current sheet width the instability develops.

First we will examine the form of the instability. The sharp change in magnetic field can be modeled by a magnetic field, $\mathbf{B}$, and density, n, profile known as the Harris equilibrium [19],

$$\mathbf{B} = B_0 \tanh(y/w_0)\hat{\mathbf{x}} \quad \text{and} \quad n = n_0 \operatorname{sech}^2(y/w_0), \tag{2.3}$$

where w_0 is the half width of the current sheet. With a particular constant temperature, T=T_0, the total pressure is balanced, but it can be unstable to the tearing instability. If a perturbation field, $\tilde{\mathbf{B}} = \tilde{B}\sin(kx)\hat{\mathbf{y}}$, is added, the instability can grow. One should note that although the Harris equilibrium is often used in studies of the tearing instability, in the HCS the magnitude of the magnetic field stays relatively constant, while the direction rotates from the $\hat{\mathbf{x}}$ direction in the asymptotic region to the $\hat{\mathbf{z}}$ direction in the center of the current sheet.

Figure 2.1 illustrates the magnetic configuration of the tearing instability. The black lines represent the magnetic fields. Before tearing (with no perturbation field), the magnetic fields are all in the horizontal direction and switch signs in the center where the current is located. At this point the entire system consists of open field lines. After tearing begins (perturbation field included) there are two different topological regions, the open field lines as highlighted in yellow, and the closed field lines highlighted in green. This change in configuration cannot happen if the frozen-in condition holds because the magnetic flux can only transfer from one topological region to the other when the frozen-in condition is violated. The frozen-in condition is broken within a current sheet when the thickness becomes small enough, permitting the topology of the magnetic field to change.

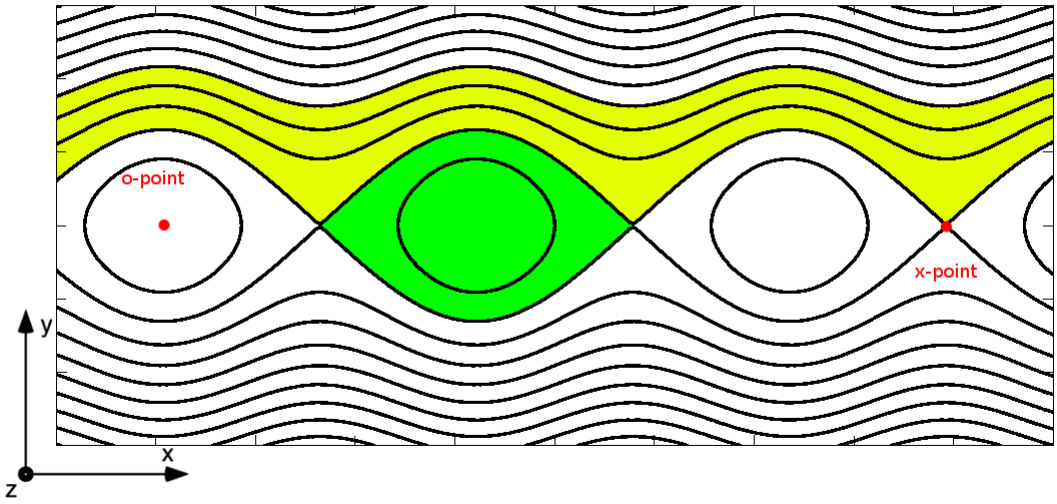

Figure 2.1: A plot of magnetic field lines around a region exhibiting the tearing instability. The aspect ratio is distorted so that features in both axes are clearly visible. The green region is an example of closed field lines, referred to as magnetic islands. The yellow region is an example of open field lines. An example of an x-point, and an o-point are labeled in red.

It is important to consider the different topological regions because they are important both in the early stages of the tearing instability, and the non-linear reconnection sites found later in time. The regions of closed magnetic field are known as magnetic islands, and we will discuss these further later in the chapter. At the center of each island is an o-point where the in-plane magnetic field goes to zero, and each island is separated by similar points with zero in-plane magnetic field called x-points. The field line that separates the two topological regions is known as the separatrix.

The aspect ratio in Figure 2.1 is exaggerated to show the details of the topology. In reality, the islands are much longer in the horizontal direction. The tension of the stretched out fields causes the islands to contract and pull more plasma towards the x-point from the open field line region. This tension drives the tearing instability.

The tearing instability was originally formulated assuming the frozen-in condition was broken due to collisional resistivity via the resistive dissipation term [18]. The growth rate of the instability scales as.

$$\gamma \sim S^{-3/5}, \tag{2.4}$$

where S is the Lundquist number,

$$S = \frac{4\pi w_0 c_A}{\eta c^2}, \tag{2.5}$$

and, $c_A = B/\sqrt{4\pi m_i n}$, is the Alfvén speed.

Therefore the instability is fastest when the thickness, w_0, is small compared to $\eta c^2/4\pi c_A$. However, even for large S the instability still occurs, so there is no thickness that prevents the development of tearing. In many systems in space the

resistivity is very small, and the system is considered collisionless. The more important constraint is that the instability only occurs when $kw_0 \leq 1$, so the current sheet must be long enough to contain wavelengths that satisfy this constraint. This constraint must be satisfied regardless of the term that breaks the frozen-in condition. A derivation of the growth rate of the tearing instability and restriction on k can be found in Appendix B.

In a collisionless plasma, the pressure term, and the inertial term are the major contributors towards breaking the frozen in condition, and thus allowing collisionless tearing. Although the pressure term may be large, only the non-gyrotropic part of the pressure tensor, described in the next chapter, plays a role. The inertial term is caused by the finite inertia of the electrons. For collisionless tearing to occur, a current sheet needs to be compressed to approximately the ion inertial scale [10, 69]. The ion inertial scale is defined as $d_i = c/\omega_{pi}$, where c is the speed of light, $\omega_{pi} = \sqrt{4\pi ne^2/m_i}$ is the ion plasma frequency, and m_i is the ion mass. An alternative formulation is $d_i = c_A/\Omega_{ci}$, where $\Omega_{ci} = eB/m_i c$ is the ion gyrofrequency. When $w_0 < d_i$ the current sheet becomes unstable to the collisionless tearing mode.

It is useful to know what length scale is expected for collisionless tearing by calculating the fastest growing wave number of the tearing mode, k. The ion gyroradius is defined as $\rho_i = v_{thi}/\Omega_{ci}$, where v_{thi} is the ion thermal velocity. In an analytic study [7], Brittnacher et al. showed that when $\rho_i/w_0 \approx 1$, the fastest growing linear mode occurs at $kw_0 \approx 0.5$. We will find that the collisionless tearing mode manifests itself at this length scale in simulations performed in later chapters.

As the tearing mode grows to the nonlinear stage, magnetic flux continues to

be transfered from the asymptotic field to the magnetic islands in a process known as magnetic reconnection. As the magnetic islands grow, they tend to merge with nearby islands and become larger.

2.3 Magnetic reconnection

As islands evolve, they may reach a steady state where the rate of flux transfer is constant with time. Growth can also be dynamic in which no period of steady growth appears. Nevertheless, it is instructive to look at the case of steady growth because it illustrates some important physics, and in some cases does occur in nature for extended periods of time [45].

Most of the magnetic energy is converted to kinetic energy in the form of heat, bulk flows, and energetic particles. Consider a flux loop in the shape of a stretched out oval with length, L, width, w, flux, $\psi = B_0 w$, and area $A = Lw$. The tension of the field contracts the island to a circular shape. The initial magnetic energy is $\sim B_0^2 A/8\pi$. After contracting, A and ψ are conserved. Therefore the magnetic field strength becomes, $B = \psi/\sqrt{A} = B_0\sqrt{w/L}$, and thus the new magnetic energy $\sim B^2 A/8\pi = (w/L)B_0^2 A/8\pi$. For a highly stretched island, where $w \ll L$, nearly all of the magnetic energy is released.

By equating the magnetic field energy lost to the outflow energy gained, $B_0^2 A/8\pi = m_i n v^2 A/2$, one finds that $v = B_0/\sqrt{4\pi m_i n} = c_A$. In other words outflows are Alfvénic. As the bent field lines accelerate away from the x-line at the Alfvén speed, a depression in the pressure develops at the x-line which pulls in new

plasma and flux from the upstream open field lines. The process continues, and so it is self driven and does not require an outside driving force.

For the tearing instability, the frozen-in condition is not satisfied within the current sheet where the magnetic field changes directions. However, once large islands develop the frozen-in condition is valid throughout much of the island. The frozen-in condition is broken only in a region around the x-point. In this dissipation region, flux can be transfered without a corresponding motion of the plasma.

Reconnection, like the tearing instability, was first formulated assuming the frozen-in condition was broken by the resistive dissipation term. A process first presented by Sweet [66], and later refined by Parker [42], described how reconnection could develop. In their description, the length of the dissipation region, L, is determined by the system size, while the width, w, is determined by the resistivity. Since the resistivity is often small in space systems, the aspect ratio was very large.

Due to conservation of mass, the flux into the dissipation region, Lv_{in}, is equal to the flux out wv_{out}, assuming constant density. Since the outflows are Alfvénic, we can say $v_{in} = (w/L)c_A$. Thus, for $w \ll L$, or large aspect ratio, the inflow of new flux is slow. We refer to this as slow reconnection.

A later formulation by Petschek [44] predicted an aspect ratio of order unity allowing for a much faster reconnection. This faster type of reconnection is referred to as fast reconnection, or Petschek type reconnection.

It turns out that for collisionless reconnection, when the current sheets are thin enough, as long as the Hall term in Equation (2.2) is accounted for, the aspect ratio becomes small enough for fast reconnection [6].

The rate of inflowing flux is referred to as the reconnection rate,

$$\frac{d\psi}{dt} = v_{in} B_{up}, \tag{2.6}$$

where B_{up} is the upstream magnetic field at the boundary of the dissipation region. In the MHD region outside of the dissipation region, where the frozen-in condition holds, Equation (2.1), the out-of-plane component of the electric field is equivalent to the reconnection rate. It can be shown that this out-of-plane electric field is the same all across a steady state reconnection region in 2D. For a 2D steady state system ($\partial/\partial z = \partial/\partial t = 0$), and using Faraday's law,

$$\frac{\partial \mathbf{B}}{\partial t} = -c\nabla \times \mathbf{E}, \tag{2.7}$$

it follows that,

$$\frac{\partial E_z}{\partial x} = \frac{\partial E_z}{\partial y} = 0. \tag{2.8}$$

Therefore, E_z is uniform across the steady state solution, and the value at the x-point, where the frozen-in condition is not valid, is also a good measure for the reconnection rate and is often used as such.

In reality however, reconnection is often not steady state but has secondary island formation in which dissipation region current layers develop magnetic islands. The motion and merging of islands then becomes an important feature of reconnection dynamics.

2.4 Islands in simulations

Islands form in many different types of simulations of reconnection. As described in the previous section, islands will form from small perturbations in a thin current sheet due to the tearing instability. Some examples of simulations that model the formation of these islands are particle-in-cell (PIC) simulations, fluid magneto-hydrodynamic (MHD) simulations with resistivity, and Hall MHD simulations.

Many simulations start with a large perturbation in the current sheet so that the non-linear stage develops quickly. Around the x-point of these simulations, secondary islands begin to form. These secondary islands have been found in PIC simulations [16, 12] and resistive MHD simulations [31, 49, 60].

In PIC simulations the tearing instability can form from the inherent noise generated by the particles [46, 36, 33]. Recently the formation of islands via this process has been investigated while working on the problem of reconnection and magnetic islands in the heliosheath. [15, 41, 52]. The simulations presented in this thesis are all PIC simulations that begin with a pure Harris sheet equilibrium, and develop islands from the noise.

In many of these simulations it is assumed that the system is two dimensional. This assumption implies there is no variation in the direction of the primary out-of-plane current (Note: There are also in-plane currents). There is often an out-of-plane magnetic field that threads through these magnetic islands causing helical shaped magnetic fields. These three dimensional magnetic islands, consisting of a bundle of wrapped up fields, are referred to as flux ropes.

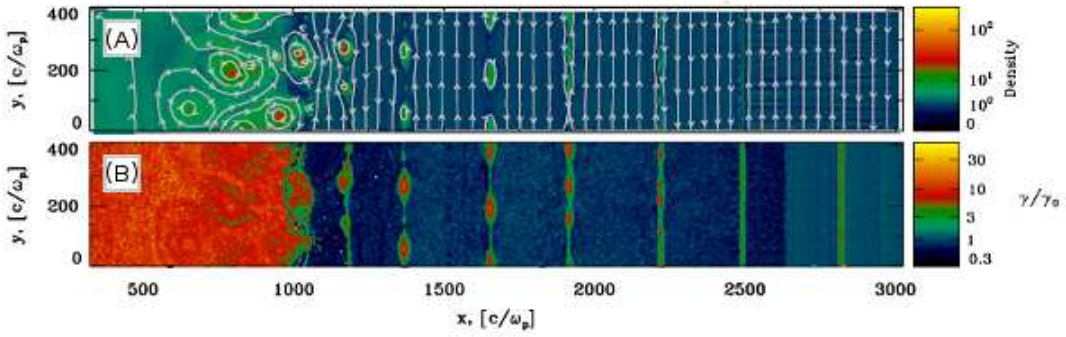

Figure 2.2: The plasma density (A) and the average particle energy (B), of a PIC simulation of a sectored electron-positron plasma. The white arrows represent the magnetic field lines. A shock that corresponds to the pulsar TS is located around $x = 1000c/\omega_p$. (Adapted with permission from Sironi et al. (2011) [62] by the American Astronomical Society)

The growth of magnetic islands and turbulence in the out-of-plane direction is a subject currently under investigation. For the bulk of this thesis we will assume a two dimensional system, although it can sometimes be helpful to picture the islands as long flux rope structures.

The striped pulsar winds described in the previous chapter have also been simulated using a PIC code [62]. Sironi et al. simulate a positron-electron plasma, and track the development of magnetic islands as striped fields approach the pulsar TS. Figure 2.2 shows the development of islands along the current sheets. The centers of the islands gain an enhanced density and thermal energy. After passing the shock, the islands are space filling. In a similar way, the islands simulated in this thesis become space filling, although at a small distance past the TS.

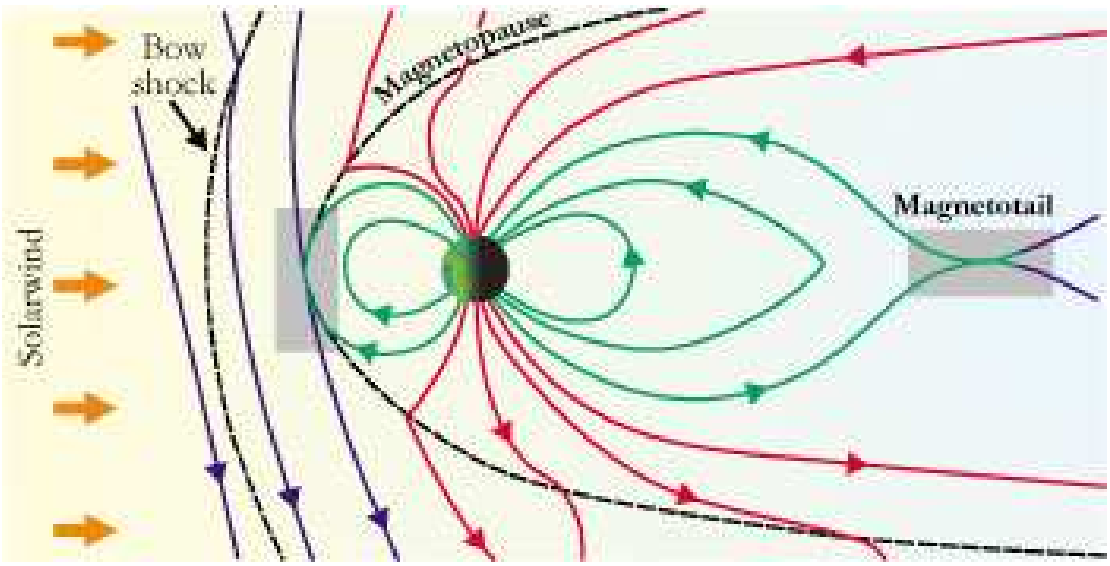

Figure 2.3: A cartoon picture the Earth's magnetosphere, bow shock, magnetotail, and regions, labeled in red, where reconnection are likely to occur. (Reprinted with permission from Day[13]. Copyright 2001, American Institute of Physics.)

2.5 Islands in nature

In nature islands can be found in many systems, from Earth's magnetic field to the farthest a man-made object has reached, in the heliosheath.

The magnetic field of the solar wind collides with the plasma contained in the Earth's magnetic field much like it does with the interstellar medium (ISM). A bow shock is generated, and the boundary between the solar wind and the plasma in the Earth's magnetic field, akin to the heliopause, is called the magnetopause. The region within the magnetopause is known as the magnetosphere. This configuration around the magnetosphere is illustrated in Figure 2.3.

When the interplanetary magnetic field (IMF) points southward, there is a sharp gradient in the magnetic field across the dayside magnetopause, and magnetic

reconnection can occur [17]. Islands can form in this system and propagate either north or south of the equator. In 1977 the ISEE spacecraft measured bipolar signatures of magnetic fields in the direction normal to the magnetopause, which are indicative of these magnetic islands [48]. These structures measured in the magnetopause are referred to as flux transfer events (FTEs).

The centers of the FTEs had hotter electrons. In addition the FTEs also contained an enhanced azimuthal magnetic field, which corresponds to a guide field that threads through the island allowing it to be a flux rope structure.

As magnetic flux from the sunward side of the magnetopause is reconnected and propagates over the poles, the night side of the Earth builds up flux. The solar wind stretches out this flux into a tail like structure known as the magnetotail. The northern and southern halves of the magnetotail have magnetic fields of opposite signs. This is another region where the conditions are right for reconnection, and island formation.

In the magnetotail islands are generated, and are often referred to as plasmoids. ISEE was also able to detect signatures of these plasmoids in the form of what they call traveling compression regions (TCRs) [63]. The TCRs consist of a bipolar signature of the northward component of the magnetic field. In addition the total magnetic field strength increases as the field is compressed. When the plasmoid travels away from the Earth, it compresses the fields above and below it.

Another important system where reconnection is believed to occur is in the solar corona. Massive discharges of energy occur in the solar corona, in events known as solar flares. The source of this energy is believed to come from magnetic

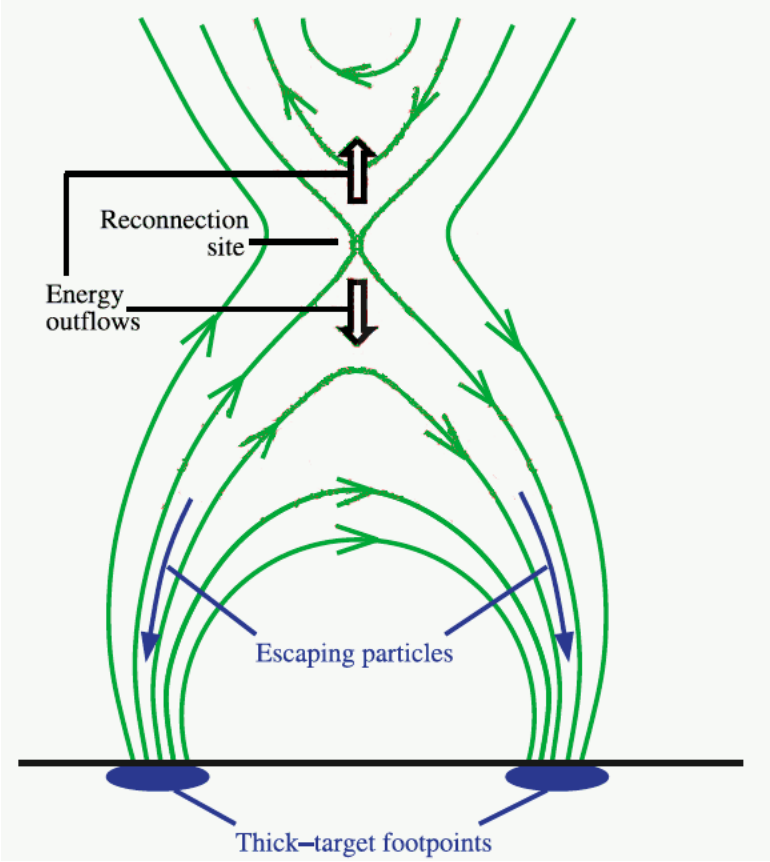

Figure 2.4: A cartoon picture of the standard model for solar flares. (Adapted with permission from Liu et al. (2008)[29] by the American Astronomical Society)

energy. This magnetic energy can be released through the process of reconnection. In the standard model of the release of magnetic energy in solar flares, shown in Figure 2.4, two open regions of magnetic flux (connected to the sun at one end) pointing in opposite directions compress together creating a current sheet. This current sheet becomes unstable to tearing, and can release magnetic energy via reconnection.

It is expected that islands should form in this current sheet and propagate, both towards and away from the sun. Recently signatures of these islands were detected by the TRACE spacecraft [59]. While looking at the 195Å filter, dark tadpole shaped structures propagate towards the postflare loops closer to the surface of the sun. The density of these signatures are much smaller than the surrounding plasma and they are unable to produce the same intensity of light.

Recently more detailed pictures of these islands have been detected, by the SDO spacecraft [51]. Savage refers to the island signatures as supra-arcade downflows (SADs), emphasizing that they are cavities rather than high density structures. She also predicts that the SADs are actually voids behind downward moving islands rather than the islands themselves, which are predicted to be much smaller. It is increasingly clear that these signatures are due to islands propagating sunward from a reconnection event higher up in the corona.

2.6 Islands in the heliosheath

In most regions in space, the plasma is considered collisionless. At 1AU, using a density of 6cm^{-3}, temperature of 12eV, and a Coulomb logarithm of 10, the electron collision frequency is about 3 days [22], and the ion collision frequency is even longer. For a particle moving at a solar wind speed of 400km/s this corresponds to a mean free path of $\sim$ 1AU. Since this density drops by a factor of 1000 in the heliosheath, and the collision rates are proportional to the density, the assumption of a collisionless plasma is very well satisfied. However, in the heliosheath the neutral density from the ISM can be as much as 100 times larger than that at 1AU, and can cause collisions by charge exchange. The mean free path for charge exchange in the heliosheath is $\sim 50 - 100$AU [39]. This scale is larger than the thickness of the heliosheath, and thus the collisionless assumption is still valid.

There has been research suggesting that the current sheets between the sectored fields found in the heliosheath are compressed to the point that collisionless reconnection begins to occur, resulting in the formation of magnetic islands [15, 11]. A turbulent MHD model of the reconnection of the sectored fields has also been proposed [27] although we will argue later that the Voyager data is inconsistent with this hypothesis.

At low latitude the solar wind is divided by the heliospheric current sheet into sectors of oppositely directed azimuthal magnetic fields. The thickness of the current sheet, λ, is around $10,000$km [64] at 1AU, and the separation between each sector, or the sector width, is around 1AU. The sector width remains nearly con-

stant, although increasingly variable, out to the termination shock (TS) at ~ 90AU, where the supersonic solar wind abruptly slows [4, 8]. For the essentially collisionless environment of the solar wind λ controls whether collisionless reconnection onsets. For λ greater than the ion inertial scale, d_i, reconnection via the collisionless tearing instability does not take place, while for $\lambda < d_i$ it does [10, 69]. Just upstream of the TS where the ion density is $\sim 0.001 cm^{-3}$, $d_i \sim 7200$km, which remains smaller than λ based on measurements at 1AU. Thus, the absence of significant reconnection of the sector field upstream of the TS is consistent with models, although a definitive study of λ upstream of the TS remains to be carried out. λ downstream of the TS is predicted to be $2,500$km based on measurements at 1AU and the shock compression, while d_i is $4,200$km based on ion density measurements of about 0.003cm^{-3} [47]. Thus downstream of the TS the current sheets should begin breaking up into magnetic islands and some Voyager 1 and 2 observations support this hypothesis [41]. The distributions of magnetic field density is different for regions with many magnetic islands and with sectored fields. We will touch on this and the β dependence of the magnetic field distributions in Chapter 4.

Chapter 3

Anisotropies and Instabilities

In the standard picture of an ensemble of particles making a non-relativistic plasma, collisions cause the distribution of momenta to become isotropic. The pressure is defined as the variance of the momentum. $P = \int d^3\mathbf{p}|\mathbf{p} - \mathbf{p_0}|^2/(2m)f(\mathbf{p})$, where $f(\mathbf{p})$ is the distribution function of particles with respect to momentum, $\mathbf{p}$, $\mathbf{p_0} = \int d^3\mathbf{p}\mathbf{p}f(\mathbf{p})/n$ is the average momentum, and m is the mass of the particles. The fluid is influenced by this pressure, by a force equal to the gradient of the pressure, $\mathbf{F} = -\nabla P$. In collisionless plasma, on the other hand, the lack of collisions allows the distribution of the momenta to develop anisotropy. The simple scalar value of pressure is not enough to describe how the fluid motion is influenced by the pressure. In this case it is convenient to define the pressure tensor.

$$\mathbb{P} = \mathbb{P}_{ij} = \int d\mathbf{p}^3 \left(p_i - p_{0i}\right)\left(p_j - p_{0j}\right)/(2m)f(\mathbf{p}) \tag{3.1}$$

The fluid is influenced by this pressure tensor, by a force equal to the divergence of the pressure tensor, $\mathbf{F} = -\nabla \cdot \mathbb{P}$.

3.1 Pressure anisotropies and their causes

The motion of particles in the direction perpendicular to the magnetic field is strongly influenced by the interaction with the magnetic field, due to the Lorentz

force,

$$\mathbf{F} = q\frac{\mathbf{v} \times \mathbf{B}}{c}. \tag{3.2}$$

The motion parallel to the magnetic field on the other hand is not affected by the Lorentz force. It is thus natural to suspect that the forces in the direction of the magnetic field, which can be described by a scalar pressure, $P_{\|} = \mathbf{B} \cdot \mathbb{P} \cdot \mathbf{B}/B^2$, would not necessarily be the same as the forces and associated pressures in the other two dimensions.

In MHD it is assumed that the distribution function is both isotropic and Maxwellian, $f(p) \sim e^{-p^2/2mT}$. The idea behind this assumption is that either classical collisions are large enough to maintain isotropy, or instabilities driven by anisotropy scatter particles sufficiently to maintain isotropy. In a nearly collisionless plasma, however, instabilities alone may be unable to maintain isotropy during reconnection.

One mechanism that can cause a pressure anisotropy is associated with Fermi reflection in reflecting particles. Once islands develop they begin to contract, simultaneously accelerating particles via a first-order Fermi process. This process is analogous to a ball bouncing between two inwardly moving walls. Each time the ball (ion or electron) collides with a wall (the end of a magnetic island) it gains energy. One of the signatures of Fermi acceleration is that the energy gain of a particle is proportional to energy. In the case of particles bouncing in a magnetic island, the energy gain occurs in the parallel velocity of the particle and leads to pressure anisotropies with $P_{\|} > P_{\perp}$. Two competing instabilities, Weibel and firehose, can

be generated by such an anisotropy.

The analogy of particles bouncing off contracting walls is useful, but the physical mechanism that accelerates the particles needs to be explained. Flow parallel to an electric field is required for energy gain. When charged particles gyrate around magnetic fields, the particles tend to drift due to inhomogeneities of the magnetic field. One such drift is known as the curvature drift,

$$\mathbf{v_{CD}} = \frac{mv_{\parallel}^2 c}{q} \frac{\kappa \times \mathbf{B}}{B^2}, \tag{3.3}$$

where $\kappa = \mathbf{B} \cdot \nabla \mathbf{B}/B^2$ is the curvature of the magnetic field. As the particles encounter the curved magnetic fields of the contracting island, they drift in the out-of-plane direction. Reconnection generates an out-of-plane electric field, which is present in regions of the island that satisfy the assumptions of ideal MHD. From Equation (2.1) it is evident that an electric field develops whenever plasma moves perpendicular to the magnetic field.

When particles undergo quasi-periodic motion, the period of the motion may slowly vary with time. If the rate of change is a much longer time scale than the period of the particles, there is an action variable that remains invariant,

$$J = \oint p dq, \tag{3.4}$$

where q is the variable that varies periodically, p is the canonical momentum associated with q, and the integral is done over one full period. These action variables are known as adiabatic invariants.

A common adiabatic invariant in plasma physics is the magnetic moment,

$$\mu = \frac{mv_{\perp}^2}{2B}. \tag{3.5}$$

In this case a particle gyro-orbits around the magnetic fields, and the action integral is over one gyroperiod. The adiabatic invariance of μ is another source of pressure anisotropy. As islands contract, the magnetic field strength within the island drops. As the field drops, so does the perpendicular velocity due to conservation of μ.

Due to the increase of the parallel velocity due to Fermi acceleration, and the drop of perpendicular velocity due to μ conservation, the pressure tensor becomes anisotropic such that $P_{\parallel} > P_{\perp}$.

3.2 The firehose instability

When a magnetized plasma has an anisotropic pressure such that $P_{\parallel} > P_{\perp}$, an instability known as the firehose instability can develop. This instability converts the free energy of the pressure anisotropy and converts it into magnetic fields. The instability is more prominent in systems with large plasma beta, β, the ratio of plasma pressure to magnetic pressure.

In order to understand the mechanism for the firehose instability it is helpful to first examine the terms of the standard MHD momentum equation. The MHD momentum equation is as follows:

$$m_i n \frac{d\mathbf{v}}{dt} = -\nabla \left(P + \frac{1}{8\pi} B^2 \right) + \nabla \cdot \left(\frac{\mathbf{BB}}{4\pi} \right), \tag{3.6}$$

where m_i is the mass of an ion, n is the ion density of the plasma, $\mathbf{v}$ is the bulk velocity, P is the plasma pressure, and $\mathbf{B}$ is the magnetic field. The left hand side is the acceleration of a fluid element, while the right hand side expresses the forces that cause acceleration. The first term is the force due to the gradient of the plasma

pressure and the magnetic pressure. The second term is caused by the tension force of the magnetic fields, and is equivalent to $\mathbf{B} \cdot \nabla \mathbf{B}/4\pi$. For the well known MHD waves termed Alfvén waves, the magnetic tension provides a restoring force for motion of plasma perpendicular to an equilibrium magnetic field.

When an anisotropy is formed with $P_\parallel \neq P_\perp$ it is necessary to use the pressure tensor, $\mathbb{P}$. For simplicity we will assume that the plasma is gyrotropic, which means that:

$$\mathbb{P} = \begin{bmatrix} P_\parallel & 0 & 0 \\ 0 & P_\perp & 0 \\ 0 & 0 & P_\perp \end{bmatrix} = \frac{\mathbf{BB}}{B^2} P_\parallel + \left(\mathbb{I} - \frac{\mathbf{BB}}{B^2} \right) P_\perp, \tag{3.7}$$

where $\mathbb{I}$ is the identity matrix. Since the particles rapidly gyro-orbit the magnetic field, the pressure along any direction perpendicular to the magnetic field is the same.

The fluid momentum equation along with this anisotropic pressure tensor in Equation (3.7) becomes

$$\rho \frac{d\mathbf{v}}{dt} = -\nabla \left(P_\perp + \frac{1}{8\pi} B^2 \right) + \nabla \cdot \left[\left(1 - \frac{\beta_\parallel - \beta_\perp}{2} \right) \frac{\mathbf{BB}}{4\pi} \right]. \tag{3.8}$$

For $\beta_\parallel = \beta_\perp$ the pressure equation reduces to the standard MHD equation. When $\beta_\parallel > \beta_\perp$ the tension force is reduced. At high β this reduction of tension force is noticeable for even slight anisotropies in the pressure. For $\beta_\parallel - \beta_\perp$ large enough, the tension force drops to zero, or even becomes negative. Since the tension of field lines acts as a restoring force for Alfvén waves in standard MHD, the negative sign causes this oscillation to become an instability known as the firehose instability [43]

for:

$$\beta_{\parallel} - \beta_{\perp} > 2. \tag{3.9}$$

This instability, fueled by the free energy contained in the pressure anisotropy, causes magnetic field lines to kink, which eventually relieves the pressure anisotropy by causing scattering. A more detailed derivation is shown in Appendix C.

3.3 The Weibel instability

The Weibel instability forms in the presence of a pressure anisotropy in regions with near zero magnetic field [67], and produces magnetic fields from the free energy contained in the pressure anisotropy of the unmagnetized plasma. In reconnection simulations an instability associated with the Weibel instability can form [32]. Weibel-produced magnetic fields form in the out-of-plane direction. These fields can scatter electrons, which isotropizes the electron pressure. Figure 3.1 shows a heuristic argument of why the instability occurs. The electrons moving to the left are deflected from the current that separates the oppositely directed fields. The electrons moving right are focused inward. These effects create a current moving to the left, which enhances the magnetic field. If there is a temperature anisotropy with higher temperature along the x direction, more particles are moving in similar trajectories along the x direction. Thus small magnetic fields perpendicular to the larger temperature are enhanced. A more detailed derivation is shown in Appendix D.

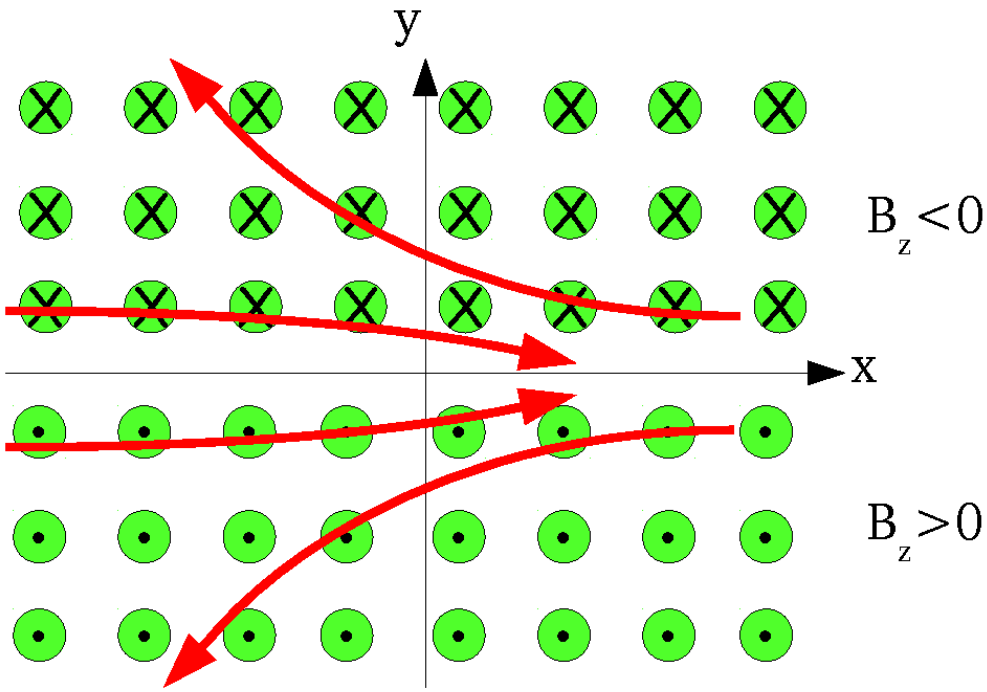

Figure 3.1: Cartoon picture of electron motions at a region where the magnetic fields change directions. The green circles with dots are magnetic field out of the plane. The circles with x's are into the plane. The red lines are electron trajectories.

3.4 Other instabilities

Alternatively, when $\beta_{\parallel} - \beta_{\perp}$ is negative and large enough in magnitude, other instabilities can occur. The mirror mode instability and the ion cyclotron instability both occur when $P_{\perp} > P_{\parallel}$. For larger $\beta_{\parallel}$ the mirror mode becomes unstable at smaller values of $|\beta_{\parallel} - \beta_{\perp}|$ than the ion cyclotron mode, so the marginal mirror mode criterion acts as the boundary between the stable and unstable regions. Based on fluid theory assuming $T_e = T_i$ [20], the mirror mode instability occurs when

$$\beta_{\perp} - \beta_{\parallel} > \frac{\beta_{\parallel}}{\beta_{\perp}}. \tag{3.10}$$

There are also kinetic modifications that can be made to the marginal instability criteria for firehose, mirror mode, and ion cyclotron which make them more accurate. Although a rigorous analytic theory is not available, there are models that approximate the instability very well [21, 3]. However, for simplicity we will just consider the conditions based on fluid theory. The changes due to kinetic theory are only quantitative rather than qualitative in nature.

Chapter 4

The Shape of Magnetic Islands in the Heliosheath

4.1 Question I: Does plasma β affect the formation of islands?

The previous chapters have described how, after crossing the TS, the HCS becomes compressed to below the inertial scale and is instable to the formation of magnetic islands. Reconnection happens at this scale in part because the solar wind can be well approximated as a collisionless plasma, and thus the reconnection and island generation should be treated as such. We have described how β is large in the heliosheath, however, many simulations of reconnection assume a low β.

The important question is whether the conventional treatment of collisionless reconnection [57] is valid in the heliosheath, where it was suggested that the pick-up ion (PUI) population increases the plasma pressure compared with values at 1 AU [70, 47, 68]. Although both Voyager spacecraft are currently taking data in the heliosheath, the energy range of the detectors does not cover the PUIs, so it is difficult to make a reliable estimate of the value for β [47]. Global magnetohydrodynamics (MHD) simulations suggest, however, that β varies from 8 to 0.5 between the termination shock and the interstellar medium with the highest β just downstream of the termination shock [15]. Although this simulation does not include a separate pick-up ion population, it provides a rough estimate for the expected values for β, and motivates the range of β in our study. In this chapter we investigate the impact

of β on the dynamics of reconnection and the formation of magnetic islands relevant to the sectored heliosheath. We find that the shape of the islands, in particular, the aspect ratio, is dependent on β.

In this study we simulate several stacked current sheets similar to the compressed sectored heliospheric fields and associated current sheets, and follow the development of reconnection and islands. We implement this system in a 2D particle-in-cell (PIC) code, and vary the temperature of the background plasma to test the dependence on β. We observe that in finite β_e systems ($\beta_e > 0.5$), very elongated islands form as opposed to the modest aspect ratio islands found at low β_e ($\beta_e < 0.5$), where β_e is the β based on the electron pressure. At high β the increased $P_{\|}$ due to the Fermi reflection of electrons within islands saturates the normal modest-aspect-ratio islands. Fermi reflection in highly elongated islands is less efficient because of the increased bounce time of the electrons so these islands are able to reach finite amplitude. At late time, however, even these elongated islands exhibit anisotropy instabilities, from Fermi reflection of both ions and electrons. As a result, late-time magnetic islands remain highly elongated and do not become round as in the low β regime. This result has significant implications for the structure of islands that would be measured in the heliosheath. Although β_e is rather moderate in the heliosheath, we find a mass ratio dependence suggesting long islands for a broad range of β_e in realistic mass ratios. A large β however may be necessary to sustain the elongation of these islands.

4.2 Computational model for sectored fields: Varying β

Our simulations are performed with the particle-in-cell code p3d. The initial conditions consist of 8 Harris current sheets [19] where the magnetic pressure balances the plasma pressure. Each Harris sheet consists of a magnetic field profile $\mathbf{B} = B_0 \tanh(y/w_0)\hat{\mathbf{x}}$, and a density profile $n = n_0 \operatorname{sech}^2(y/w_0)$. In addition there is a uniform background population that has a density of $n_b = 0.2n_0$. These simulations are done in 2 dimensions so $\partial/\partial z = 0$, where $\hat{\mathbf{z}}$ is out-of-plane, parallel to the initial current. The $\hat{\mathbf{y}}$ direction corresponds to the radial direction and the $\hat{\mathbf{z}}$ direction corresponds to the northward direction in the heliosheath picture of this system.

The code uses normalized units. The time scale is normalized to the ion cyclotron time Ω_{ci}^{-1}. The distance scales are normalized to the ion inertial length $d_i = c/\omega_{pi}$, and thus the velocity is normalized to the Alfvén speed v_A. The magnetic field is normalized to the asymptotic value of the reversed magnetic field B_0. The density is normalized to the peak value of the Harris profile, n_0 The pressure is normalized to $P_0 = n_0 m_i v_A^2 = B_0^2/4\pi$. The temperature is normalized to $T_0 = m_i v_A^2$.

In order to vary the β of these simulations we vary the temperature of the background population T_b. This background temperature is the same for both ions and electrons. The Harris equilibrium is used to balance the sharp change in the magnetic field strength across the current sheets, while the background represents the pick-up ions and has the greatest influence on late time reconnection dynamics. We performed simulations for β = 0.2, 1, 2, 3, and 4.8, where β is based on the

pressure in the asymptotic field with density n_b. Each simulation was advanced for a time of $120\Omega_{ci}^{-1}$ with a time resolution $dt = 0.004\Omega_{ci}^{-1}$. The simulations are on a $204.8d_i \times 102.4d_i$ domain with a grid scale resolution of $\Delta_x = \Delta_y = 0.05d_i$. In order to complete such large runs, unless otherwise specified, we used 25 for the mass ratio of the ions to electrons. This makes it easier to resolve small electron scales. In order to lessen the separation between the field and particle time scales, we set the ratio of the speed of light to the Alfvén speed, c/c_A, to 25 (in the heliosheath a more realistic value is near 6000). Reconnection is insensitive to the value of c/c_A. We start with a half thickness for the current sheet $w_0 = 0.5d_i$, so that collisionless reconnection can begin from particle noise. The temperature in the Harris sheet is $0.25T_0$ for both ions and electrons, and there is no guide field. The largest β we simulated was 4.8 since the electron thermal velocity $v_{the} \approx 0.7c$. Larger β would begin to have significant unphysical relativistic effects, due to our lowered ratio of c/c_A.

The simulation does not precisely describe the heliosheath but illustrates important physics that should be found there. The ion pressure in the heliosheath is much larger than the electron pressure, and thus β_e is actually quite moderate compared with that of the ions. We do not have a separate population of pick-up ions. The equilibrium magnetic field configuration in our simulation is a Harris sheet rather than the rotated field configuration (where $|B|$ is constant in a cut through the current sheet) that characterizes the heliospheric current sheet. However, the total out-of-plane flux from these layers is small because their width is very small compared with the total sector width. Thus, this flux should not significantly im-

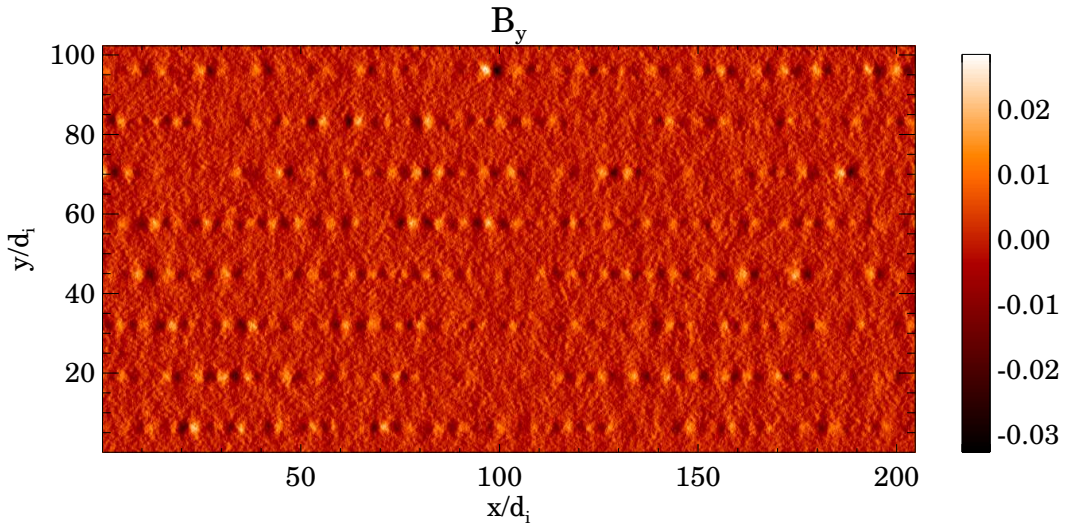

Figure 4.1: Normal component of the magnetic field, B_y, for $\beta = 2$, at $t = 15\Omega_{ci}^{-1}$. The bipolar signatures in the current sheet indicate the presence of x-lines arising from the collisionless tearing mode.

pact the dynamics. Future simulations tailored to the specific parameters of the heliosheath are planned.

4.3 The initial state: How do the islands form, and what sets their length?

The early development of a run with $\beta = 2$ is shown in Figure 4.1. Not surprisingly a wave mode with $k_x w_0 \approx 0.5$ clearly emerges. The finite β background plasma does not have a strong effect on the wavelength of linear tearing. During this time, within the current sheets, an anisotropy in the electron pressure begins to develop with $P_{e\parallel} > P_{e\perp}$. The electrons moving at the thermal velocity are able to bounce between the two ends of the islands which have lengths of $\sim 6d_i$.

Comparisons with runs at different β show that at this early time, the lengths of the islands appear to be insensitive to β.

There are two important time scales controlling the dynamics: the time it takes for the ions to accelerate to Alfvénic outflow speeds and the time it takes for a significant electron pressure anisotropy to develop. If electrons bounce several times between the two ends of a contracting island, an anisotropy develops which approaches the firehose instability boundary. This is because the bouncing electrons gain energy in the parallel direction. The time for an electron to bounce off the edge of an island and then return to its original position is thus a measure of the time for significant anisotropy to develop.

The tearing instability is driven by the tension in the newly reconnected magnetic fields. Since anisotropies cause a weakening of the magnetic tension, the tearing mode can be suppressed by strong anisotropy within an island.

Reconnecting magnetic field lines, by relaxing their tension, accelerate ions up to Alfvénic speeds. If several bounces occur during the time required for ions to be accelerated up to the Alfvénic outflow speed from the x-line, the developing anisotropy slows the ion outflow and essentially stops the growth of the tearing mode. However, since the bounce time is proportional to the length of the islands, the growth of sufficiently long wavelength tearing modes can continue.

Near an x-line adjacent to a growing island, the outflow velocity of ions, to first approximation, linearly increases with distance (see Figure 4.2) as

$$v_{ix} = \frac{1}{t_a} x. \tag{4.1}$$

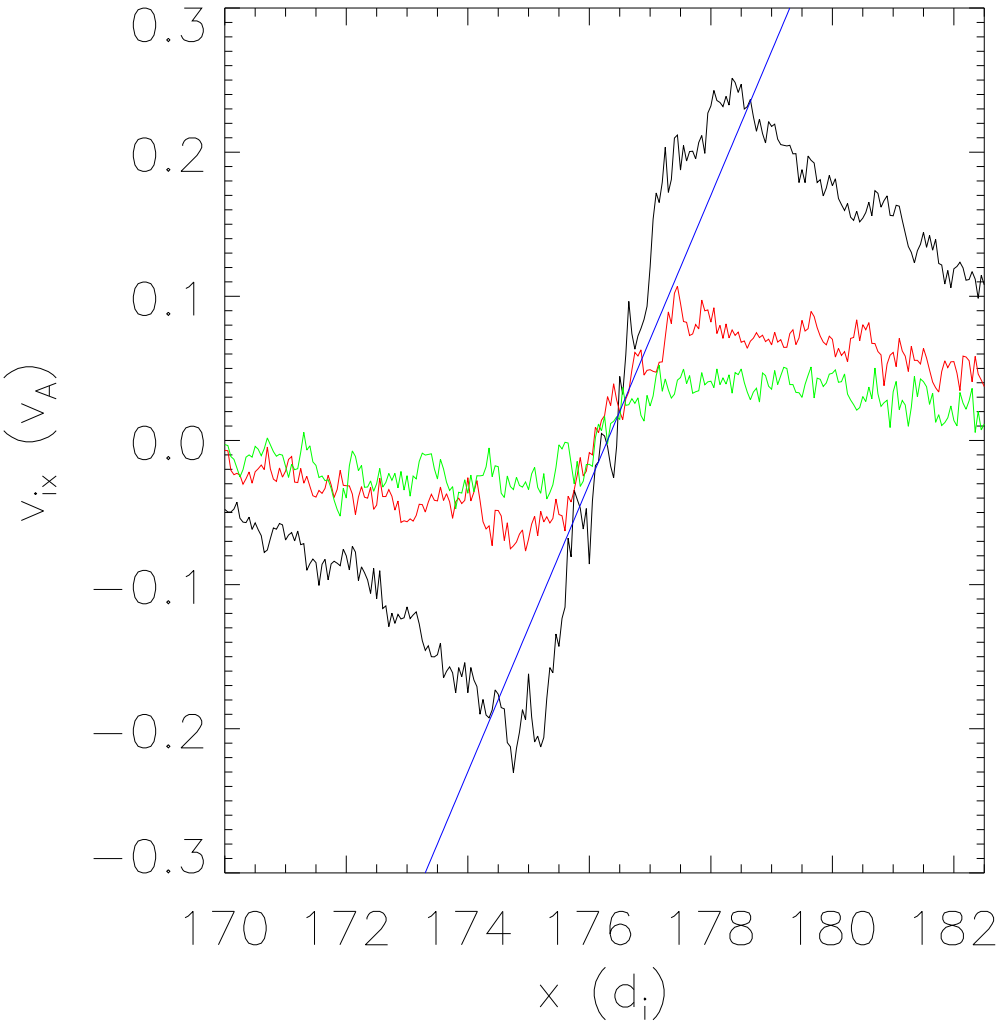

Figure 4.2: Ion outflow velocity, v_{ix}, versus the position x, for $t = 25\Omega_{ci}^{-1}$ (green), $30\Omega_{ci}^{-1}$ (red), and $35\Omega_{ci}^{-1}$ (black) for the $\beta = 2$ run. To reduce noise we do a 5 point smooth of v_{ix} in both the $\hat{\mathbf{x}}$ and $\hat{\mathbf{y}}$ directions. The blue curve is a line of slope 0.1, which corresponds to a convective growth time t_a of around $10\Omega_{ci}^{-1}$.

At this point t_a is just defined as the inverse slope of the relationship between v_{ix} and x. Since according to Figure 4.2 the slope is constant, this implies that ions accelerate away from the x-line in an exponential fashion. By integrating, the time, t, for an ion to accelerate from the initial position, x_0, to the final position, x_f, can be obtained.

$$t = \int_{x_0}^{x_f} \frac{dx}{v_{ix}} = \int_{x_0}^{x_f} \frac{t_a dx}{x} = t_a \ln \frac{x_f}{x_0}, \tag{4.2}$$

and thus

$$x_f = x_0 e^{t/t_a}. \tag{4.3}$$

An approximate measure for the characteristic time scale for acceleration away from the x-line up to the Alfvén speed is $t \approx t_a$, the acceleration time. As seen in Figure 4.2, the acceleration time at $t = 30\Omega_{ci}^{-1}$ is of order $\sim 10\Omega_{ci}^{-1}$. This acceleration time is approximate, can vary by a factor of as much as 2, and appears to be insensitive to β.

The bounce time can be estimated based on the thermal velocity of the electrons, v_{the}, and the length of the island, L:

$$t_b = \frac{L}{v_{the}} = \frac{L}{v_A}\sqrt{\frac{1}{\beta_e}\frac{m_e}{m_i}}, \tag{4.4}$$

where β_e is the β determined solely from the plasma pressure derived from the electrons.

Equating the empirical acceleration time $t_a = 10\Omega_{ci}^{-1}$, and the bounce time t_b, Eq. (4.4), a critical island length can be found:

$$L_{crit} \approx 10 d_i \sqrt{\beta_e \frac{m_i}{m_e}}. \tag{4.5}$$

For islands with $L < L_{crit}$, the anisotropy will stop the tearing instability. Islands smaller than L_{crit} can still form, but they quickly saturate. A similar saturation was found in [23]. However, in their simulations the size of the computational domain was $12.6\rho_i$ and $L_{crit} = 100\rho_i$, where ρ_i is the ion Larmor radius. Thus, the development of long wavelength islands was not observed.

For the case of $\beta = 2$ ($\beta_e = 1$) and $L \approx 6d_i$, $t_b \approx 1.2\Omega_{ci}^{-1}$. This time is much less than the acceleration time, so there is enough time for a significant anisotropy to develop before a significant x-line is established. This anisotropy can be seen in Figure 4.3a, which shows the regions from the $\beta = 2$ run that are unstable to the firehose instability. The unstable regions occur inside the islands and stop further growth of the short wavelength tearing modes. The islands that continue to grow correspond to longer wavelength, with $L \approx 40d_i$ and $t_b \approx 8\Omega_{ci}^{-1} \approx t_a$. Thus, the anisotropy develops slowly enough for reconnection to develop. This can be seen in Figure 4.3b.

4.4 Comparing length prediction with simulation data

As can be seen in Figure 4.4, by $t = 51\Omega_{ci}^{-1}$, β has a significant influence on the structure of islands. The islands for $\beta = 0.2$ have much shorter wavelength than for $\beta = 2$ and 4.8. In other words there are more locations where reconnection proceeds in the case of low β. This phenomenon is expected based on the previous analysis, $L_{crit} \propto \sqrt{\beta_e}$. Since L_{crit} is proportional to the square root of the mass ratio $\sqrt{m_i/m_e}$, we expect to find much longer islands in the real mass ratio limit.

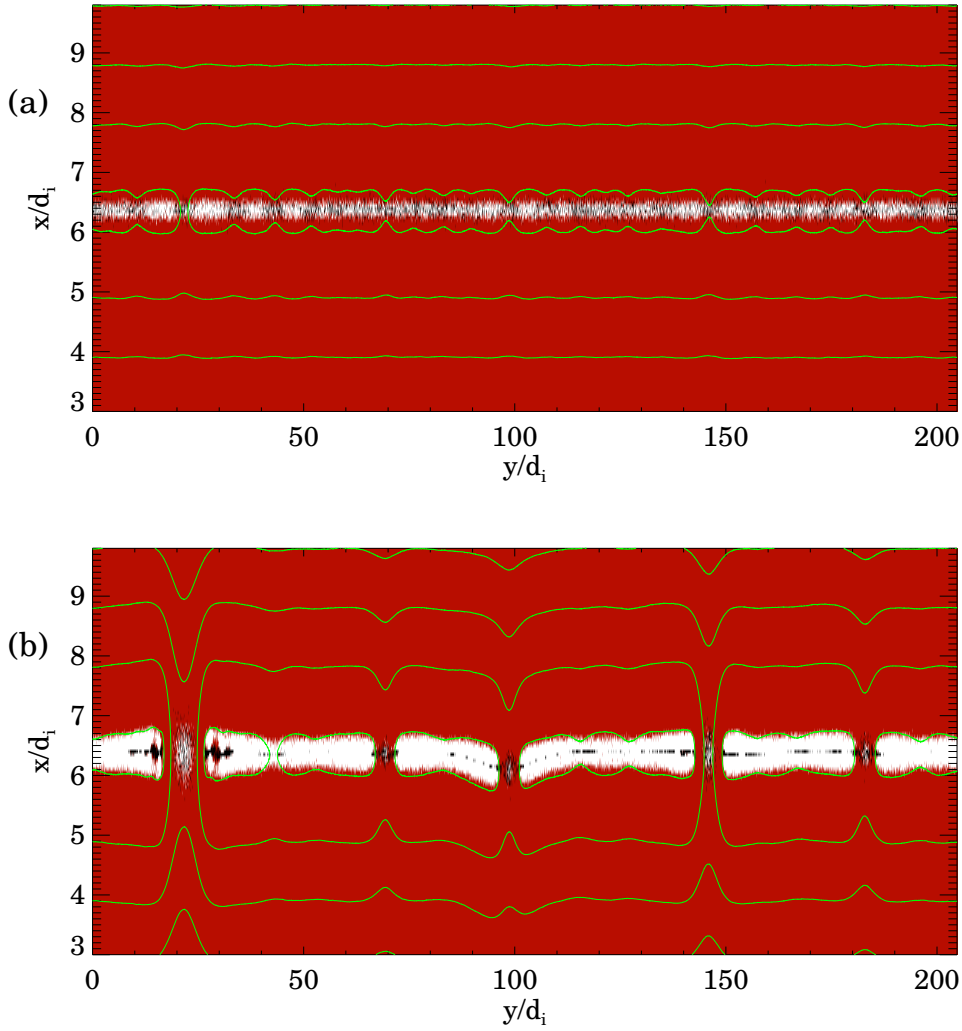

Figure 4.3: Regions where the plasma anisotropy causes instability. White regions are unstable to the firehose, black regions are unstable to the mirror mode, and red are stable. The green lines are magnetic field lines. This plot shows one current layer taken from the $\beta = 2$ run at (a) $t = 25\Omega_{ci}^{-1}$ and (b) $t = 40\Omega_{ci}^{-1}$. The aspect ratio is distorted to make the islands more visible.

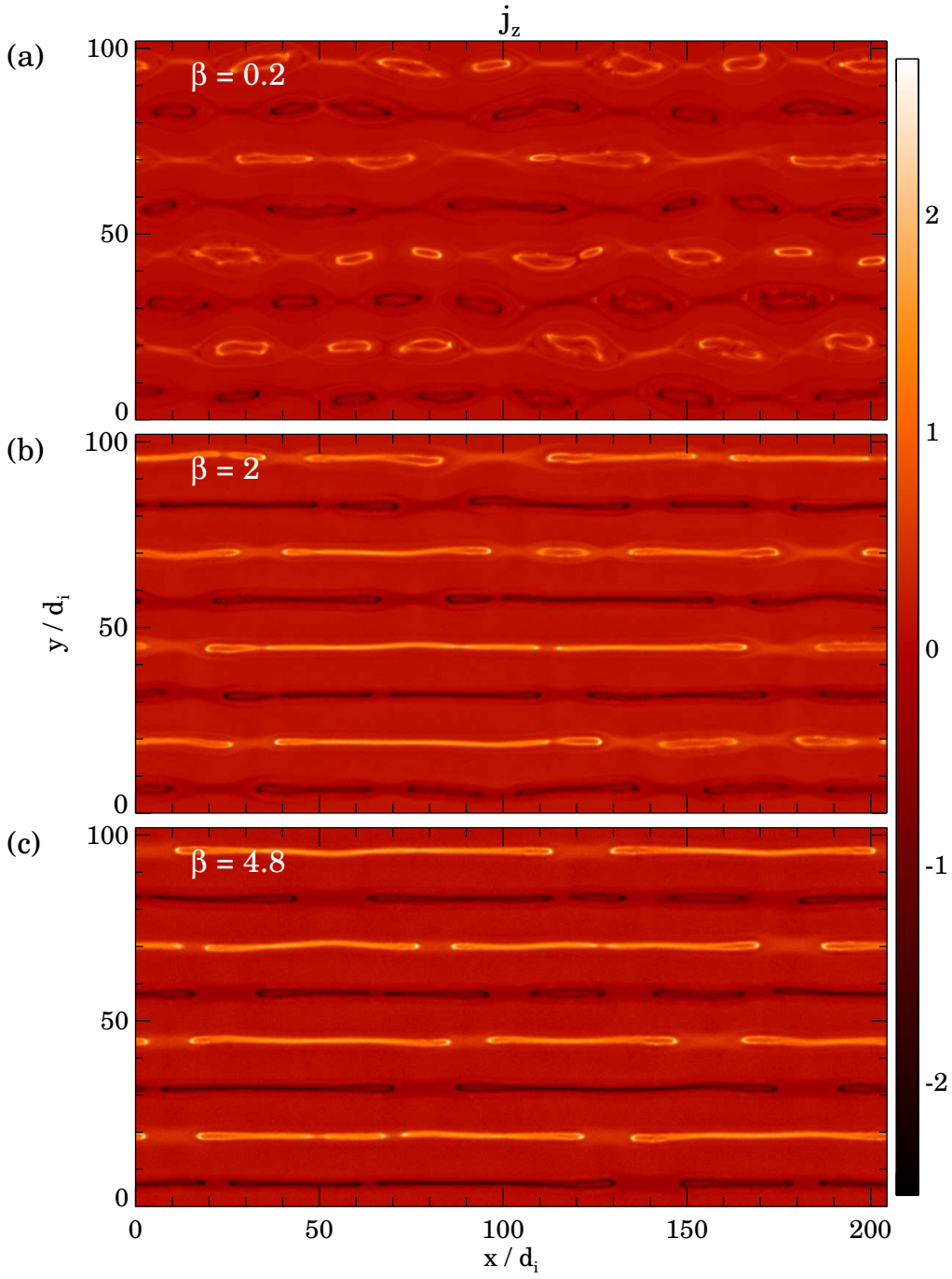

Figure 4.4: Out-of-plane current, j_z, at $t = 51\Omega_{ci}^{-1}$ for β of (a) 0.2, (b) 2, and (c) 4.8.

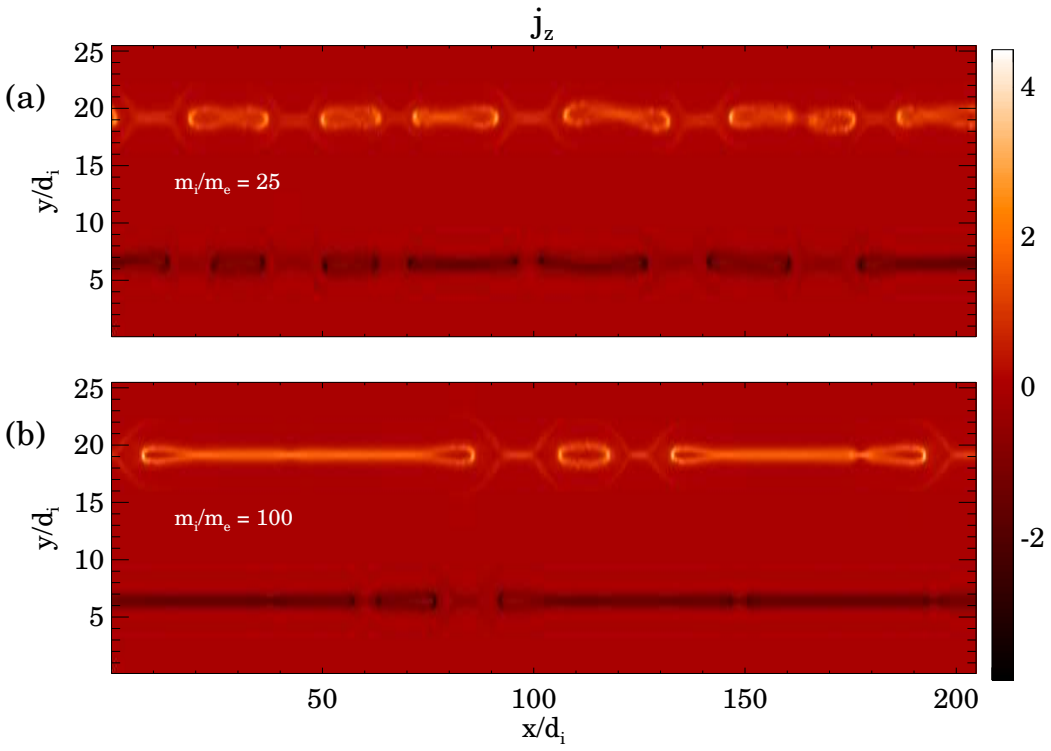

Figure 4.5: Out-of-plane current, j_z, $\beta = 0.2$ at (a) $t = 40\Omega_{ci}^{-1}$ for $m_i/m_e = 25$, and (b) $t = 60\Omega_{ci}^{-1}$ for $m_i/m_e = 100$. The aspect ratio is distorted to make the islands more visible.

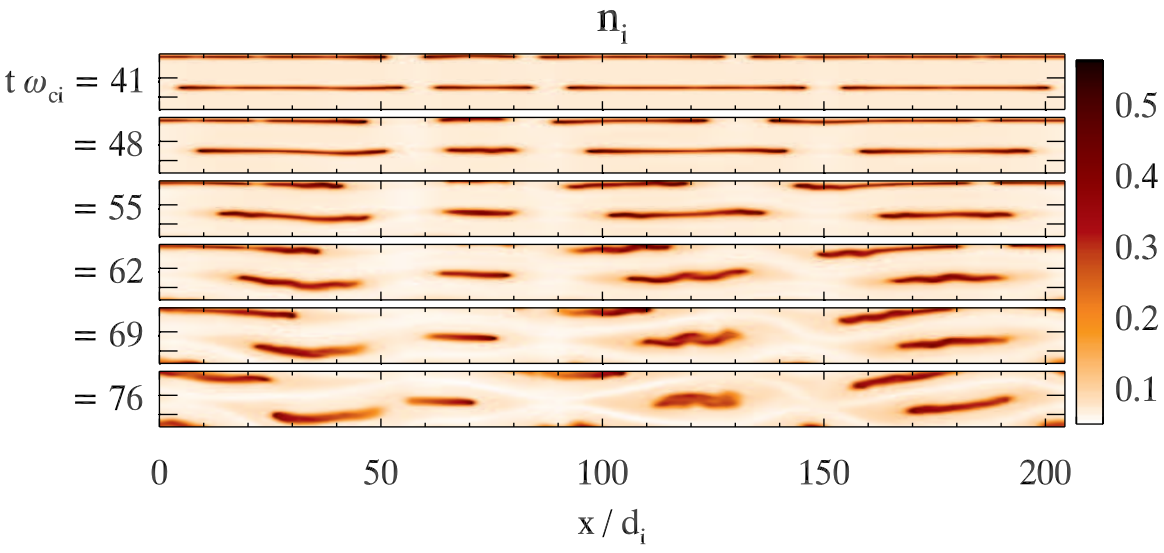

Figure 4.6: Ion density, n_i, for $\beta = 2$, along one current sheet between $t = 41$ and $66\Omega_{ci}^{-1}$.

To test this, we perform a $\beta = 0.2$ simulation with $m_i/m_e = 100$. In this case we reduce the y-domain by a factor of 4 with respect to Figure 4.4a, examining only two current sheets. We double the resolution in order to resolve the small electron scales, and reduce the ratio of the speed of light to the Alfvén speed to 15. There is a clear dependence on m_i/m_e shown in Figure 4.5, where we compare the bottom two current sheets of Figure 4.4a to the new simulation. We find the islands to be significantly longer, confirming our prediction. Since $m_i/m_e \gg 100$ in the heliosphere, long islands are almost always expected, unless β_e is very small.

4.5 Anisotropies: Growth and saturation

As elongated islands grow at high β, anisotropies within them also develop even though the anisotropies do not suppress island growth. The anisotropy surpasses

the firehose condition in the center of the islands. These anisotropies are likely caused by the Fermi mechanism [14]. The dynamics of this acceleration mechanism will be discussed in chapter 6. The contraction of islands can be seen in Figure 4.6. The higher density regions inside of the islands move inward at Alfvénic speeds. At around $t = 61 - 66\Omega_{ci}^{-1}$ the islands begin to kink, which indicates the onset of an anisotropy instability.

The short wavelength mode is caused by the temperature anisotropy due to the outflow from the x-line streaming through the plasma entering the exhaust across the separatrix, and the Fermi acceleration of electrons bouncing in the island. Based on the similarities in growth rate and other signatures that will be discussed in chapter 6, this mode appears to be associated with the Weibel instability.

The anisotropies that develop during the reconnection simulation do not grow without bound. In Figure 4.7 we plot the fraction of grid points that are unstable to the firehose instability. As time advances and the anisotropies begin to form, the number of grid points unstable to the firehose instability increases. However, at $t \sim 80\Omega_{ci}^{-1}$, the number of unstable grid points begins to saturate. Since it takes place soon after the onset of the kinking of the islands, the saturation is likely because the anisotropy is reduced via scattering by the Weibel and firehose instabilities. Additionally the saturation occurs soon after the unreconnected flux is exhausted. By $60\Omega_{ci}^{-1}$ the islands have grown enough so that the islands on adjacent current sheets begin to interact. This is an additional reason for the saturation of the firehose unstable area: there is no more space into which the firehose unstable islands can expand.

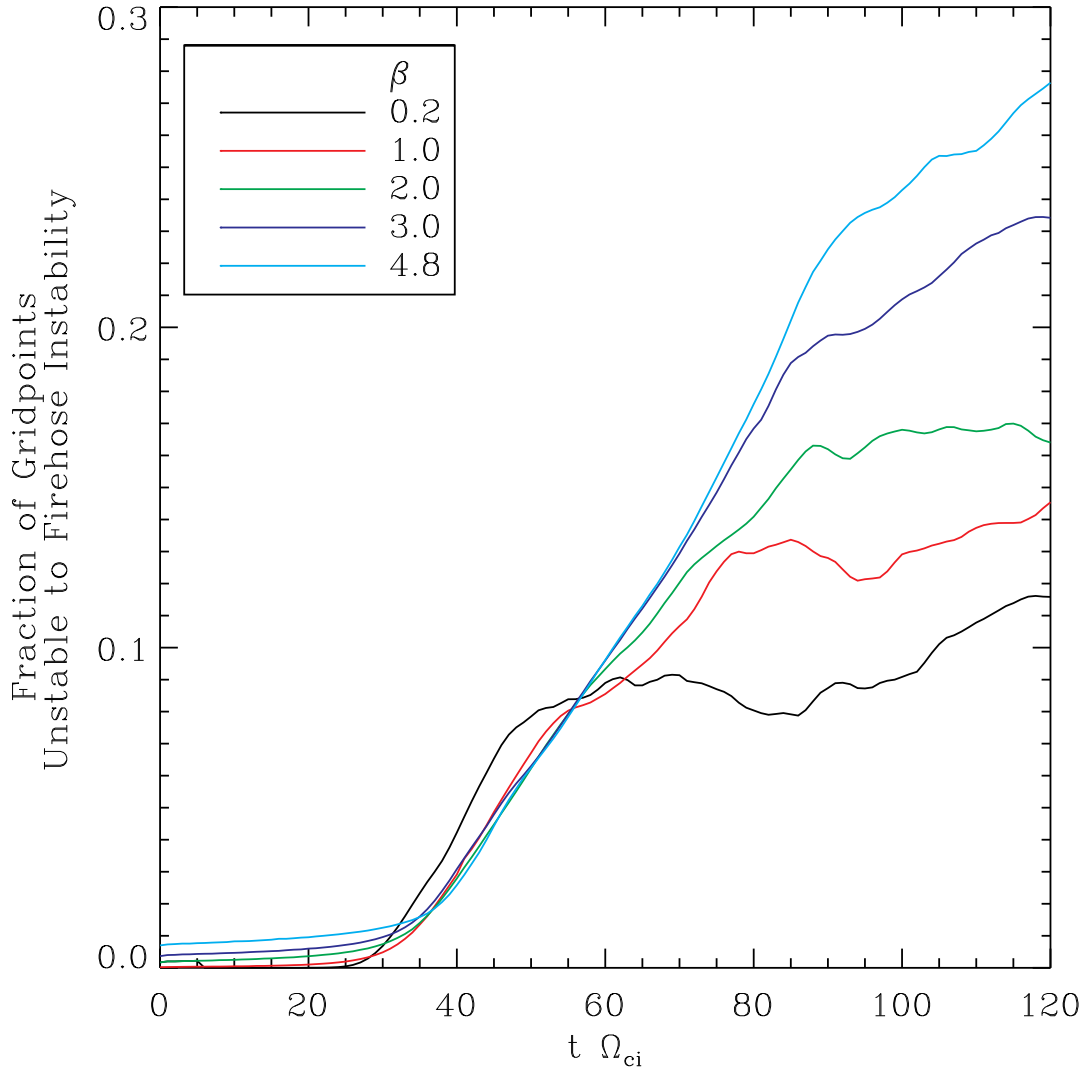

Figure 4.7: Fraction of grid points unstable to the firehose instability vs. time for $\beta = 0.2, 1, 2, 3$, and 4.8.

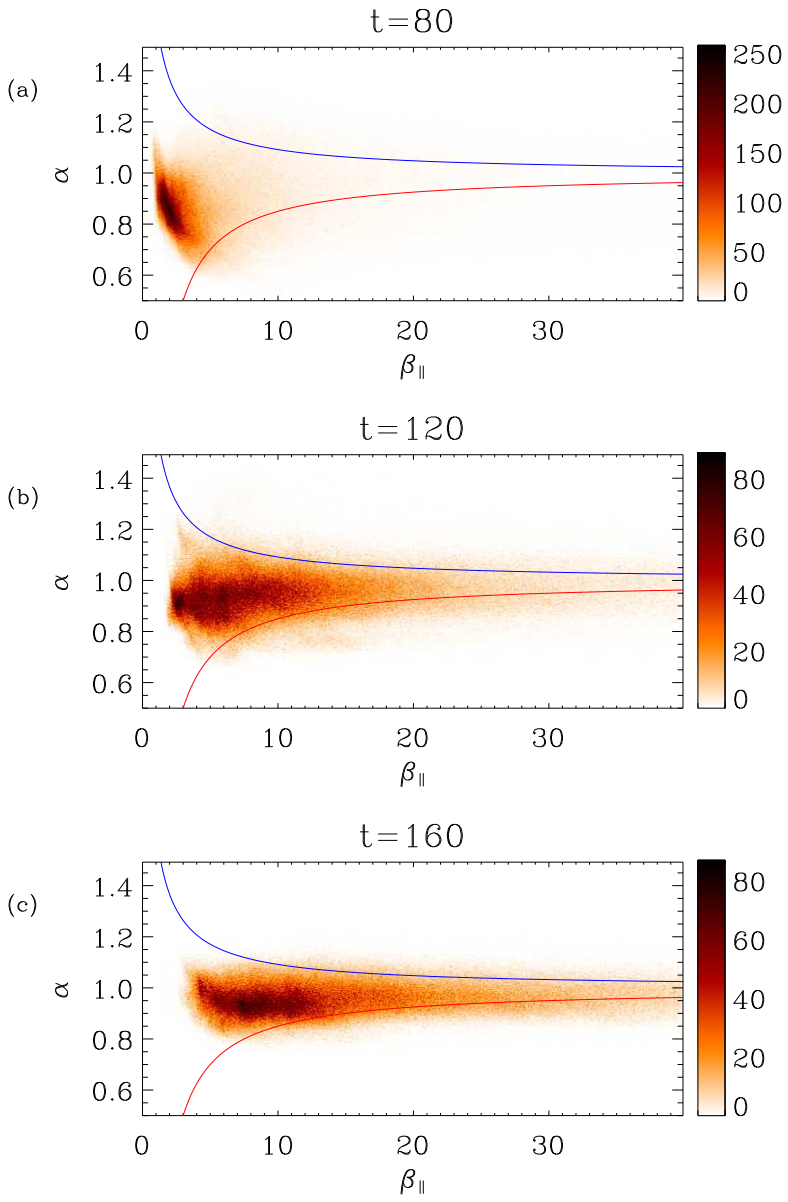

Figure 4.8: 2d histogram of anisotropy ($\alpha = P_\perp/P_\|$) vs. $\beta_\|$ for $\beta = 2$ at times from top to bottom $t = 80, 120$, and $160\Omega_{ci}^{-1}$. The blue line represents the marginal condition for mirror mode instability. Points above this curve are unstable. The red line represents the firehose marginal stability condition. Points below this curve are unstable. The color bar represents the number of points with a particular α and $\beta_\|$.

At late time the anisotropy of the system is confined within the boundaries of the marginal firehose (Eq. (3.9)) and mirror mode instabilities (Eq. (3.10)) in a manner similar to that seen in observations of the solar wind [21, 3] and in earlier low β current sheet simulations [15]. Figure 4.8 shows the data for our system in the space of (α,$\beta_\parallel$) where $\alpha = P_\perp/P_\parallel$. This plot is generated by calculating the anisotropy α and the $\beta_\parallel$ for each grid point. The plot is a 2-dimensional histogram of grid points in (α,$\beta_\parallel$) space, where $\beta_\parallel$ is calculated based on $P_\parallel$. The parallel and perpendicular pressures are calculated by taking the diagonal components of the pressure tensor after rotating into the frame of the local magnetic field, such that the two perpendicular components are equal. We look at the distribution at $t = 80, 120,$ and $160\Omega_{ci}^{-1}$. At early times the anisotropies have not yet fully developed and the plasma still occupies a small region in (α,$\beta_\parallel$) space. By $t = 120\Omega_{ci}^{-1}$ the anisotropy has reached the two stability boundaries, and continues to be confined between these two boundaries at $t = 160\Omega_{ci}^{-1}$, even as the average β increases. The anisotropy reaches the stability boundaries at a time after the short wavelength Weibel modes have dissipated. Since at this point there are no longer large regions with essentially zero magnetic fields, the firehose and mirror mode instabilities are what determine the boundaries of the temperature anisotropies. There are no clear signatures of the classical mirror mode instability at this time. The firehose and mirror mode instabilities may be hard to distinguish among the turbulent interacting magnetic islands, or the islands may just stop generating anisotropy as they approach the instability boundaries.

4.6 Do long islands last long?

The islands maintain an elongated form for the simulation shown in Figure 4.4c clear until $t = 120\Omega_{ci}^{-1}$, the latest time simulated for $\beta = 4.8$. This is shown in Figure 4.9a showing the out-of-plane current for $t = 120\Omega_{ci}^{-1}$. Since the edges of the islands are pushing against the firehose instability, the tension force in the magnetic fields is eliminated. This can be seen in Figure 4.9b which shows the regions that are unstable to the firehose instability.

4.7 Conclusions about islands at high β

The magnetic islands that reach a significant amplitude are much more elongated at high β_e than at low β_e. These elongated islands should be found even for moderate values of β_e at realistic mass ratios. Island elongation is caused by the suppression of the shorter wavelength tearing modes by pressure anisotropies ($P_{\parallel} > P_{\perp}$) that develop due to the Fermi acceleration of electrons. Later in time the plasma develops pressure anisotropies of both ions and electrons that are limited by the firehose and Weibel instabilities. A Weibel mode develops that kinks the magnetic field lines. In the regime with a real mass ratio we would expect even longer islands to form, where multiple wavelengths of the firehose instability could develop. At late time the fraction of points unstable to the firehose instability saturates, and the anisotropy is confined between the mirror mode and firehose instability boundaries. The long islands persist due to the low requirement of anisotropy to reach the marginal firehose condition at high β. For even small anisotropies the tension

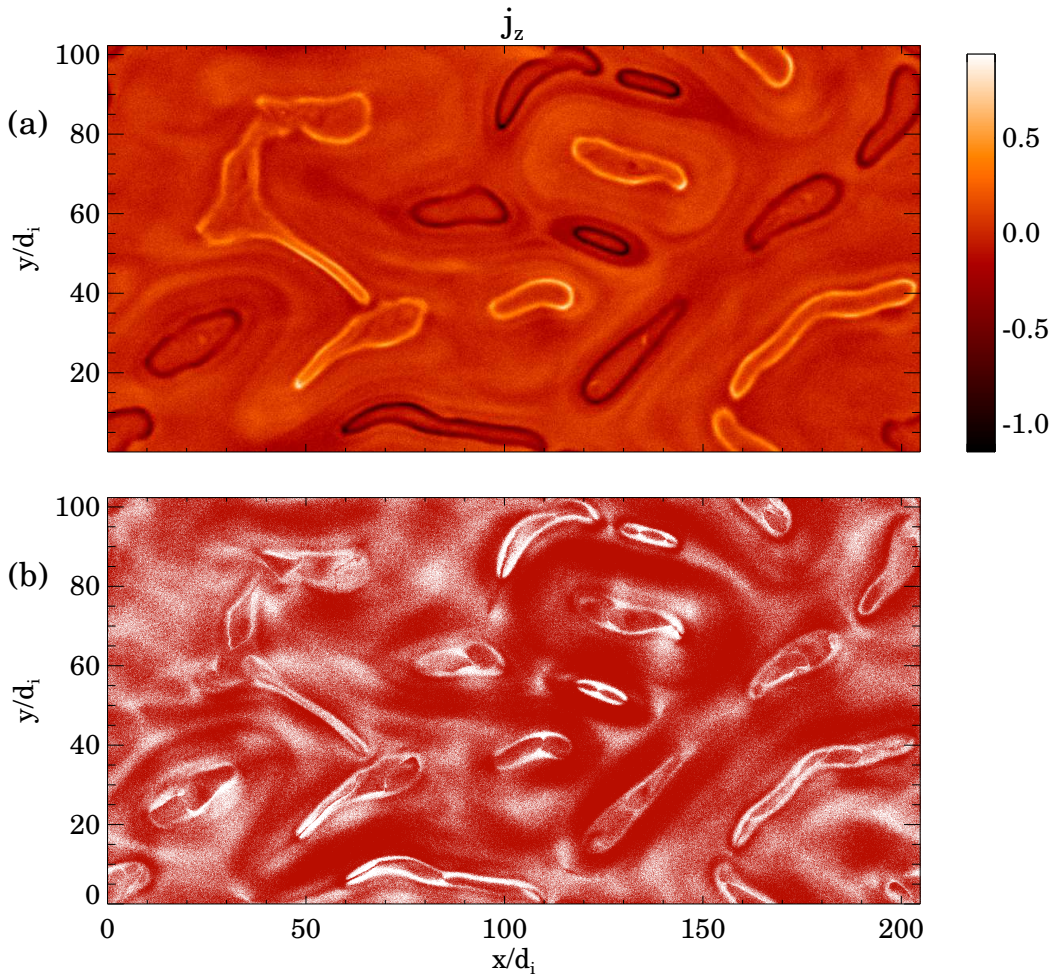

Figure 4.9: Out-of-plane current, j_z(a), and Stability(b) at $t = 120\Omega_{ci}^{-1}$ for the $\beta = 4.8$ case. White regions in part (b) are unstable to the firehose, and red are stable.

in the magnetic fields is removed.

When encountering magnetic islands in the heliosheath, we predict the formation of similar extended, sausage-shaped islands rather than the more round islands found in low β simulations [15]. The cores of these islands should also be at the marginal firehose condition, so the magnetic tension that drives them to become round vanishes. We would thus expect these sausage shapes to persist long after the islands have ceased growing, and thus could be found even in regions where reconnection is no longer occurring.

For the simulations in this chapter there was no out-of-plane guide magnetic field. In the heliospheric current sheet, the magnetic field rotates from one direction to the other keeping a constant magnitude rather than passing through zero [64]. A guide field would cause the center of the islands to have a much lower β since the magnetic field does not go to zero. Because of this magnetic field, we would not expect the Weibel instability to develop. In real systems there is frequently a guide field, so this would be worth further investigation.

4.8 Comparing long island result with Voyager data

These elongated islands exhibit signatures that can be seen in Voyager data. In particular Voyager measures all three components of the magnetic field. Of particular interest for the explorations of islands that grow in the ecliptic plane is the angle $\lambda = \tan^{-1}(B_T/B_R)$ where B_T and B_R are the azimuthal and radial magnetic fields, respectively. $\lambda = 90^\circ$ and 270° correspond to the azimuthal unreconnected

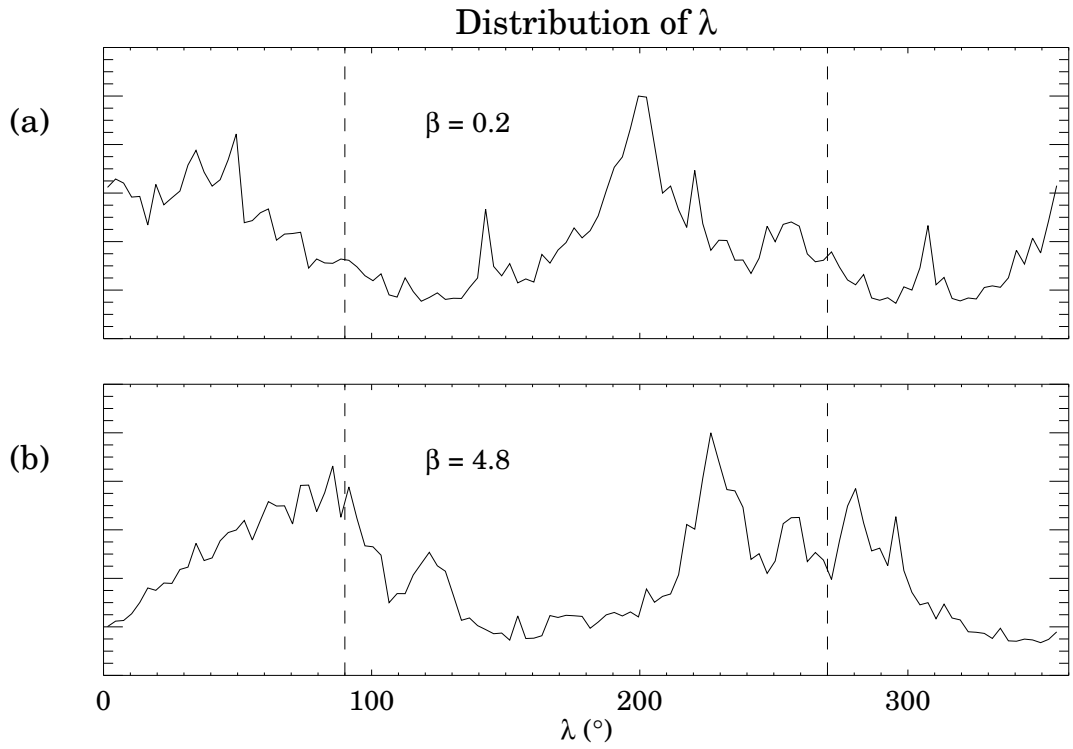

Figure 4.10: Distribution of λ, at $t = 110\Omega_{ci}^{-1}$ for the (a) $\beta = 0.2$ case and (b) $\beta = 4.8$ case. The dotted lines are at $\lambda = 90°$ and $270°$ where we expect to find peaks in the distribution.

sectored heliosheath magnetic fields. Deviation of λ from 90° and 270° indicates some process is distorting the sectored field. Voyager data shows the distribution of λ is peaked in the two azimuthal directions $\lambda = 90°$ and 270° [41]. These peaks are significantly broader in the heliosheath than upstream, indicating that reconnection or another mechanism is disturbing the heliosheath field. The observed Voyager distribution of λ is consistent with that found in high β simulations[41]. Since the islands are elongated, the magnetic fields tend to remain primarily in the azimuthal direction even well after the islands begin to interact with each other. Round islands, such as would be expected from an MHD model or a low β kinetic model, are not consistent with observations since they produce much broader λ distributions. Thus, MHD reconnection [27] in the heliosheath seems to be ruled out. Shown in Figure 4.10 is the distribution of λ from the simulations at $\beta = 0.2$ (Figure 4.4a), and $\beta = 4.8$ (Figure 4.4c) at $t = 110\Omega_{ci}^{-1}$. The high β simulation which has elongated islands retains the two peaks at $\lambda = 90°$ and $\lambda = 270°$. The long islands have a larger magnetic field in the azimuthal direction than the radial, resulting in peaks in the λ distribution, but the shorter islands become round having a magnetic field with similar strength in both directions, resulting in a broad distribution in λ. The loss of tension in a finite β plasma prevents the complete release of magnetic energy that would be expected in an MHD model. A complete understanding of the β dependence of magnetic islands is essential in order to obtain reliable signatures that can be compared with Voyager data.

4.9 Other applications of high β elongated islands

In astrophysical accretion discs, reconnection plays a role in determining the saturation of the magnetorotational instability (MRI) [50]. The saturation of MRI is strongly dependent on the dissipation of the magnetic field due to reconnection. For the high β in accretion discs, suppression of the most strongly growing small islands may significantly impact the saturation of the MRI. Since β is typically larger than 100 in these structures, the the only surviving islands would be so long that it is likely that much of the magnetic free energy would not be dissipated. Further, since the MRI requires magnetic tension, the absence of tension could limit the development of the instability. Sharma et al. [55] perform a simulation showing an enhancement of the growth of MRI due to anisotropies with $P_\perp > P_\parallel$, which enhances the magnetic tension, caused by μ conservation as a magnetic field develops. They do not capture the physics of reconnection and Fermi acceleration in magnetic islands that would generate anisotropies with $P_\perp < P_\parallel$, which removes magnetic tension. These two competing sources of anisotropy both affect the tension and thus the growth of the MRI. The relative importance of these mechanisms needs to be explored.

Reconnection at high β, although relatively rare in the terrestrial magnetosphere, is also found in the magnetosphere of Saturn [34]. Magnetic islands were discovered in a region where β is larger than 10. The β dependence of the growth of finite sized magnetic islands may lead to a better understanding of these findings.

Since the development of elongated islands requires only moderate β, we expect to see the development of longer islands than expected in lower β systems such as the

magnetosphere. In contrast to [23], these longer islands can grow to a large enough size to play a role in magnetospheric dynamics. Since the β of the magnetosphere is not exceptionally large it is unlikely that the persisting anisotropy is enough to keep the islands from eventually becoming round.

Chapter 5

The Scaling of Island Growth

5.1 Question II: Are the islands relevant in the heliosheath?

The growth of islands in the finite plasma β (the ratio of the plasma pressure to the magnetic pressure) heliosheath has been investigated in particle-in-cell simulations [15, 41, 52]. The predicted island length in the initial phase of reconnection is around $190d_i$, much smaller than the sector width, $8900d_i$, so it is uncertain whether islands will grow to the full sector width. Due to computational limitations it is not possible to realistically simulate the disparate ion inertial and sector scales. In this chapter, we perform a scaling study of the growth of islands, in which the inter-current sheet separation (equivalent to the sector width) varies, in order to understand what happens in the real system. Even our largest simulations have sector widths that are much smaller than in the actual sectored heliosheath.

The current sheets separating the sectored regions begin to form islands after crossing the termination shock (TS). As the islands grow, the current sheets are convected towards the heliopause. The plasma flows outward at around 80km/s and steadily decreases in speed for 20AU, at which point the radial flow remains close to zero [26]. The important question which we seek to answer is whether the islands are able to expand to the sector width before the current sheet reaches the heliopause. If the islands expand to the sector width, there would be no more

laminar field that can shield cosmic rays, and cosmic rays could percolate through the system consisting solely of islands. In addition, the full expansion of the islands would imply that acceleration mechanisms due to the growth of islands may play a significant role.

5.2 Simulation setup for scaling

We simulate the growth of magnetic islands using a particle-in-cell code, p3d. The initial conditions consist of two oppositely directed current sheets in Harris [19] equilibrium, with a superimposed background density. The initial magnetic fields are in the $\hat{\mathbf{x}}$ direction, which corresponds to the azimuthal direction in the heliosheath. The current flows in the $\hat{\mathbf{z}}$ direction, which corresponds to the north-south direction. The $\hat{\mathbf{y}}$ direction corresponds to the radial direction of the heliosheath. In the heliosheath the islands are predicted to be highly elongated due to the development of pressure anisotropy [52]. The elongation is dependent on both the ion-to-electron mass ratio and the electron temperature. Typical simulations use a reduced mass ratio in order to reduce computational expenses, which produces much shorter islands than expected for the real system. We therefore use an enhanced temperature of both the ions and the electrons in the background in order to form more realistic elongated islands. The ratio of the proton to electron mass in this simulation is 25, and the background temperature is 15 times the Harris sheet temperature of $0.25 m_i c_A^2$ where m_i is the ion mass and c_A is the Alfvén speed based on the asymptotic magnetic field, B_0. The ratio of the speed of light to the Alfvén speed is 25.

Each simulation has a grid scale resolution of $\Delta_x = \Delta_y = 0.05d_i$ and a time resolution of $dt = 0.004\Omega_{ci}^{-1}$, where Ω_{ci} is the ion cyclotron frequency. The half thickness of the current sheet is set to $w_0 = 0.5d_i$ so that collisionless reconnection can begin from particle noise. We simulate a 2 dimensional system. In 3 dimensional systems islands form at different z locations and grow along z, eventually stagnating likely due to interactions with other islands [58, 54]. The significance of this effect in the heliosheath is unknown.

5.3 Do islands keep growing? Can they reach the sector width?

The time evolution of the largest of these simulations, with dimensions of $409.6d_i \times 102.4d_i$, can be seen in Figure 5.1. By $t = 60\Omega_{ci}^{-1}$ the current sheet has broken into elongated magnetic islands as predicted in [52] (Figure 5.1(a)). The length of the islands is smaller than the separation between the two current sheets, so it is expected that they could not grow to the sector width since circular islands do not have tension to drive reconnection. However, as can be seen at the subsequent times (Figure 5.1(b,c,d)), the islands on a given current sheet begin to merge. Merging lengthens the islands which enables further growth until they approach the neighboring current sheet.

5.4 How long does it take to reach the sector width?

The islands found in the heliosheath, which are predicted to be much shorter than the current sheet separation, should in principle grow to the sector width as

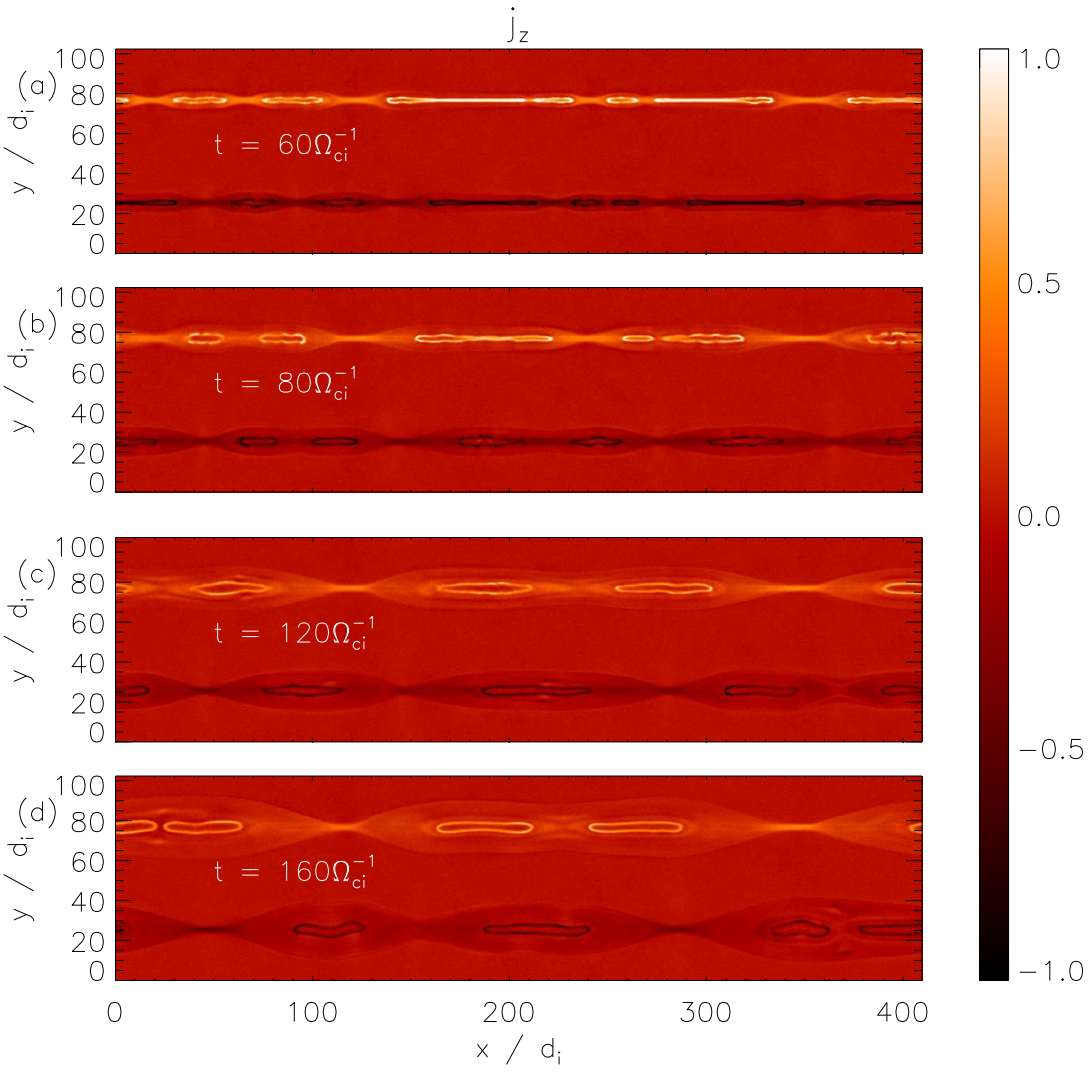

Figure 5.1: Out-of-plane current density, j_z, for t = (a) $60\Omega_{ci}^{-1}$, (b) $80\Omega_{ci}^{-1}$, (c) $120\Omega_{ci}^{-1}$, and (d) $160\Omega_{ci}^{-1}$ For better contrast, all points with $|j_z| > 1$ are assigned the colors shown for 1 or -1.

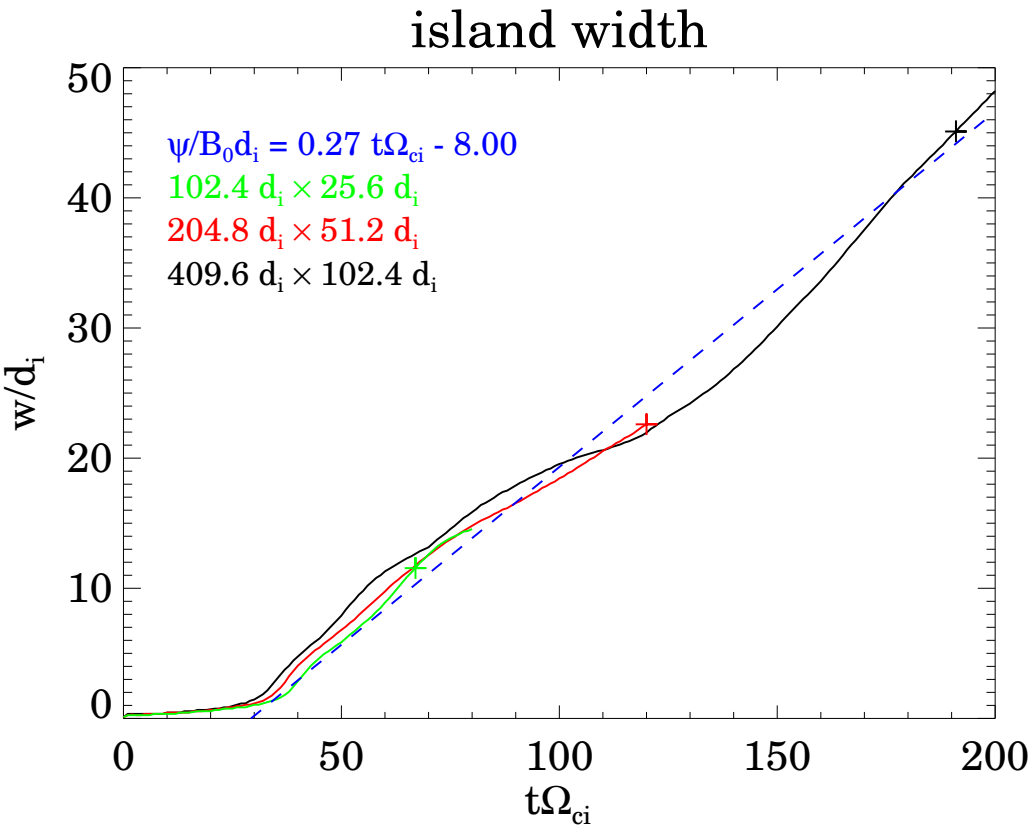

Figure 5.2: Width of the largest island in the lower of the two current sheets versus time for simulations with dimensions of $102.4d_i \times 25.6d_i$ (green), $204.8d_i \times 51.2d_i$ (red), and $409.6d_i \times 102.4d_i$ (black). The plus signs denote the point where the island width reaches 44% of the system size and represents the time when the island begins to interact with the other current sheet. The blue dashed line is a line of best fit between these three points. The slope of this curve is the rate of growth at which the island expands, $0.12c_{Ab}$.

long as the islands are able to continue merging. The aspect ratio of our simulation box is 4, which was sufficient for islands to continue merging up to the time that they begin interacting with the neighboring current sheet. We also carried out a simulation with aspect ratio 2 where the islands stopped merging when their length approached the system size. The islands saturated and stopped growing when there was no longer enough magnetic tension to maintain reconnection. The size of the heliosheath in the azimuthal direction greatly exceeds the sector width. Islands should therefore grow to the sector width. The next question is how long it takes for these islands to reach the sector width. In order to establish this time we carry out a scaling of the time required to grow to the sector width for system sizes $102.4d_i \times 25.6d_i$, $204.8d_i \times 51.2d_i$, and $409.6d_i \times 102.4d_i$.

To determine the size of the island we find the minimum of the flux function , ψ where the magnetic field, $\mathbf{B} = \hat{\mathbf{z}} \times \nabla\psi\left(x, y\right) + B_z\left(x, y\right)\hat{\mathbf{z}}$, along the center of the lower initial current sheet at a particular time. This minimum corresponds to the most developed x-point. The upper current sheet has x-points at the maxima. The line of constant flux that crosses an x-point is known as the separatrix. The distance between the maximum and minimum y-locations of the separatrix is defined as the island width, w. Figure 5.2 shows the island width versus time for each of the simulations. We use the time when the island reaches 44% of the size of the box as a measure for when the island reaches the neighboring current sheet. At 50% the island begins to be affected by the presence of the neighboring current sheet. The best fit line connecting the times when the islands reach the neighboring current sheet fits very well with the island width versus time for all the simulations.

The results of Figure 5.2 suggest that the islands grow at a nearly constant rate that is independent of the system size. Keeping in mind that this number is based on only three data points, using the slope of the best fit curve we can obtain an estimate for the rate of growth of the island of around $0.12c_{Ab}$, where c_{Ab} is the Alfvén speed based on the background density, which is distinct from the normalization of the code, c_A, which uses the peak density of the Harris equilibrium. If we extrapolate the growth rate to a very large system we can predict a time for the islands to reach the sector width. Based on a magnetic field, B, of 0.15nT and density, n, of 0.003cm^{-3} the Alfvén speed just downstream of the TS is 60km/s. Using this speed for c_{Ab}, and the sector width, $W = 0.25$AU, we obtain a growth time, t_g, of about 60 days, much less than the plasma convection time across the heliosheath.

$$t_g = 60 \text{ days} \left(\frac{W}{0.25 \text{ AU}}\right) \left(\frac{n}{0.003 \text{ cm}^{-3}}\right)^{1/2} \left(\frac{B}{0.15 \text{ nT}}\right)^{-1} \tag{5.1}$$

Assuming the radial velocity of the solar wind inside the heliosheath is 70km/s during island growth, this time corresponds to a distance of 2.5AU past the TS.

In addition to the rate of change in the island width being nearly constant, we find that the reconnection rate is also independent of system size. In Figure 5.3 we look at a similar plot to Figure 5.2, but of the reconnected flux. To find the reconnected flux we take the difference between the maximum and minimum of the flux function along the center of the initial current sheet. Based on the slope of the best fit curve, the reconnection rate was 0.079. Previous scalings of

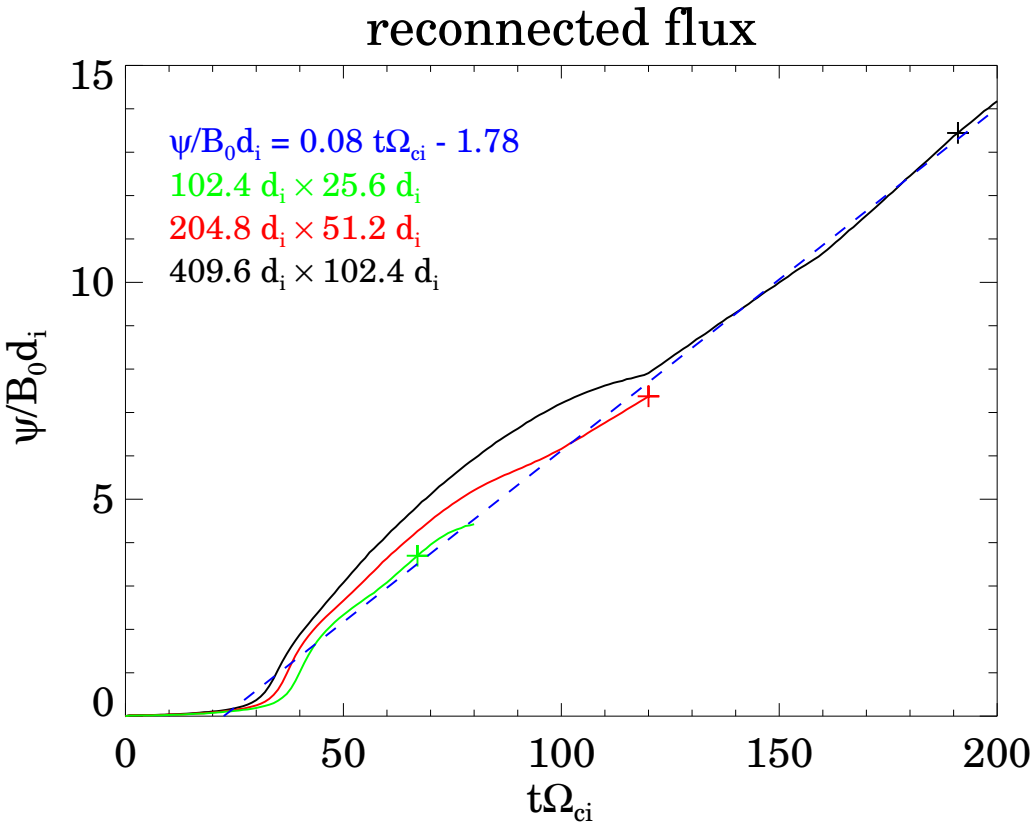

Figure 5.3: Reconnected flux in the lower of the two current sheets versus time for simulations with dimensions of $102.4d_i \times 25.6d_i$ (green), $204.8d_i \times 51.2d_i$ (red), and $409.6d_i \times 102.4d_i$ (black). The plus signs denote the point where the island width reaches 44% of the system size and represents the time when the island begins to interact with the other current sheet. The blue dashed line is a line of best fit between these three points. The slope of this curve is the reconnection rate $0.079B_0c_A$.

reconnection rate versus system size for conditions with lower plasma β, relevant to the Earth's magnetosphere and the 1AU solar wind, have shown comparable rates [56, 57]. However it is important to note that the reconnection rates shown in [56, 57] are associated with a steady state reconnection, as opposed to the rate shown here which includes the complicated dynamics of the merging process as well.

5.5 Conclusions on scaling

In the range of sizes simulated the rate of flux reconnection and the rate of island growth is nearly constant once reconnection begins. The growth rates are independent of the system size. It is reasonable to conclude that in a larger system these trends would continue. The merging of magnetic islands allows the islands to maintain a high aspect ratio, which maintains the magnetic tension necessary to drive reconnection. The steady reconnection rate allows for a constant rate of island growth, resulting in islands with a width that scales like the current sheet separation. These islands would be fully grown long before reaching the heliopause. The growth of these islands in the heliosheath is vital for the generation of anomalous cosmic rays (ACRs) by Fermi acceleration in islands [15]. Since these islands are expected to be present in the sectored region, and the flux of ACRs is greatly reduced outside of the sectored region [41] both observations and models suggest that the sectored heliosheath has broken into magnetic islands.

Chapter 6

Particle Acceleration in Magnetic islands

6.1 Brief introduction to particle acceleration in reconnection

Energetic particles are often associated with magnetic reconnection. Their presence is inferred from observations [28] of gamma rays and x-rays that are generated by the collisions of accelerated electrons and ions with the solar atmosphere [28]. Direct detections of energetic electrons in reconnection outflows have been made in the magnetotail [37]. When reconnection occurs, many magnetic islands can form. This can be seen in observations of flux transfer events in the magnetopause [48], bursty bulk flows in the magnetotail [63], and in supra-arcade downflows in the solar corona [59, 35, 51]. Recent simulations have revealed energization in this context through mechanisms such as Fermi reflection within islands[38, 15, 52]. Reconnection has been suggested as a source for the anomalous cosmic rays found in the heliosheath [15].

6.2 Question III: Does plasma β affect particle energization in islands?

An effective method for examining the energization of particles is to simulate several stacked current sheets, which leads to large numbers of interacting magnetic

islands. This method is particularly relevant to the sectored magnetic fields found near the ecliptic in the heliosheath [15, 11]. We implement this system in a 2D particle in cell (PIC) code, and vary the temperature of the background plasma to test the dependence on β, where β is the ratio of plasma pressure (ion plus electron) to the magnetic pressure.

Once islands develop they begin to contract, simultaneously accelerating particles via a first-order Fermi process. This process is analogous to a ball bouncing between two inwardly moving walls. Each time the ball (ion or electron) collides with a wall (the magnetic edge of an island) it gains energy. One of the signatures of first-order Fermi acceleration is that the energy gain of a particle is proportional to energy. In the case of particles bouncing in a magnetic island, the energy gain occurs in the parallel velocity of the particle and leads to temperature anisotropies with $T_{\parallel} > T_{\perp}$. Two competing instabilities, Weibel and firehose, can be generated by such an anisotropy.

The particle acceleration due to the Fermi mechanism should in principle depend on β [14]. The Fermi mechanism accelerates particles in the direction parallel to the magnetic field and thus creates a temperature anisotropy. As the anisotropy grows, the system approaches marginal firehose stability, where the tension of the bent magnetic fields, and along with it the Alfvén speed, reduces to zero. The firehose instability occurs when.

$$1 - \frac{\beta_{\parallel} - \beta_{\perp}}{2} < 0$$

Particles gain energy in the Fermi mechanism by bouncing off the Alfvénic flows

associated with island contraction, which is driven by magnetic tension. As tension decreases, the outflow velocity from the x-line is reduced and acceleration does as well. In higher β systems a smaller anisotropy is needed before reaching the firehose stability boundary and thus particle acceleration should be inhibited. The reduction of the outflow speed, however, plays less of a role than expected on the β dependence of acceleration. The tension of the fields goes to zero in some regions, but the regions where the tension is still large maintain island contraction near the Alfvén speed.

We find that the more important factor is the development of an other anisotropy instability driven by electrons, the Weibel instability. The Weibel instability develops in the presence of a temperature anisotropy in regions with near zero magnetic field [67], and produces magnetic fields from the free energy contained in the pressure anisotropy of the unmagnetized plasma. In reconnection simulations an instability associated with the Weibel instability can develop [32]. Weibel-produced magnetic fields form in the out-of-plane direction. These fields can scatter electrons, which isotropizes the electron temperature and disrupts the Fermi reflection process and associated energy gain.

We find that β has a strong effect on the electrons, while ion acceleration is nearly independent of β, within the range of β studied. Both the electrons and the ions are accelerated mostly by a first-order Fermi process in contracting islands. The electrons, however stop accelerating due to the onset of the Weibel instability. The out-of-plane magnetic fields generated by the Weibel instability keep the electrons from freely bouncing back and forth and Fermi accelerating. Since the ion gyroradius is large compared to the length scales of the Weibel generated fluctuations of the

magnetic field, ions are not significantly affected.

In this paper we first describe the computational model and the parameters used in our simulations. Next we show individual tracked particles accelerating and eventually interacting with the Weibel magnetic fields. In addition, we show the development of the Weibel instability in the simulations along with the confirmation of the signatures of the Weibel instability in smaller simulations. Finally we draw some conclusions about what this means for real systems such as the heliosheath and accretion flows.

6.3 What's new about the computational model

Our initial setup described in chapter 4 is convenient for examining the growth of many islands and how particles can be accelerated in this context. In this chapter we will be discussing the same simulations described in in chapter 4, with additional identical simulations where we track the most energetic electrons, and ions.

Our full simulations track $\approx 10^9$ particles. Recording the trajectories of all these particles is not feasible. However, we have recently made upgrades to p3d [24] that allow us to track the trajectories of selected particles. We used the upgraded particle tracking code to follow the trajectories of approximately 200 of the most energetic electrons and ions (178 electrons and 275 ions) for the $\beta = 2$ run.

6.4 Particle heating and β: There is a correlation

In our simulations we investigate the effect of β on a system of stacked current sheets. Figure 4.4 shows the results of three of these simulations after magnetic islands begin to develop. The difference in the island lengths is discussed in Chapter 4[52]. However, we also find that there is a β dependence on the heating of the electrons. The β dependence can be seen in the bulk change in pressure of the electrons, see Figure 6.1. Individual trajectories of accelerated electrons imply a scattering mechanism that suppresses acceleration in large β systems. Out-of-plane magnetic fields generated by a Weibel instability play a role in the scattering of the electrons.

We explore the heating of the electrons and ions by looking at the average pressure of the system, P, which can be calculated by taking the trace of the pressure tensor and dividing by 3. Over time this pressure increases, which is reasonable since magnetic energy dissipates during reconnection. Strikingly, there is a big difference between the pressure gains of the ions and the electrons. The pressure gain of electrons is 4 times less for $\beta = 4.8$ than for $\beta = 0.2$, while the ion pressure gain is hardly changed. Since the number of particles is constant, average pressure gains imply average temperature gains. As seen in Figure 6.1, the amount of heating of the ions (change in average pressure from that at $t = 0$), ΔP_i, is nearly independent of β. The slight dependence observed is expected due the slowing of the outflow caused by the approach to firehose instability. The electron heating, ΔP_e, on the other hand is strongly dependent on β. This observation leads to the conclusion

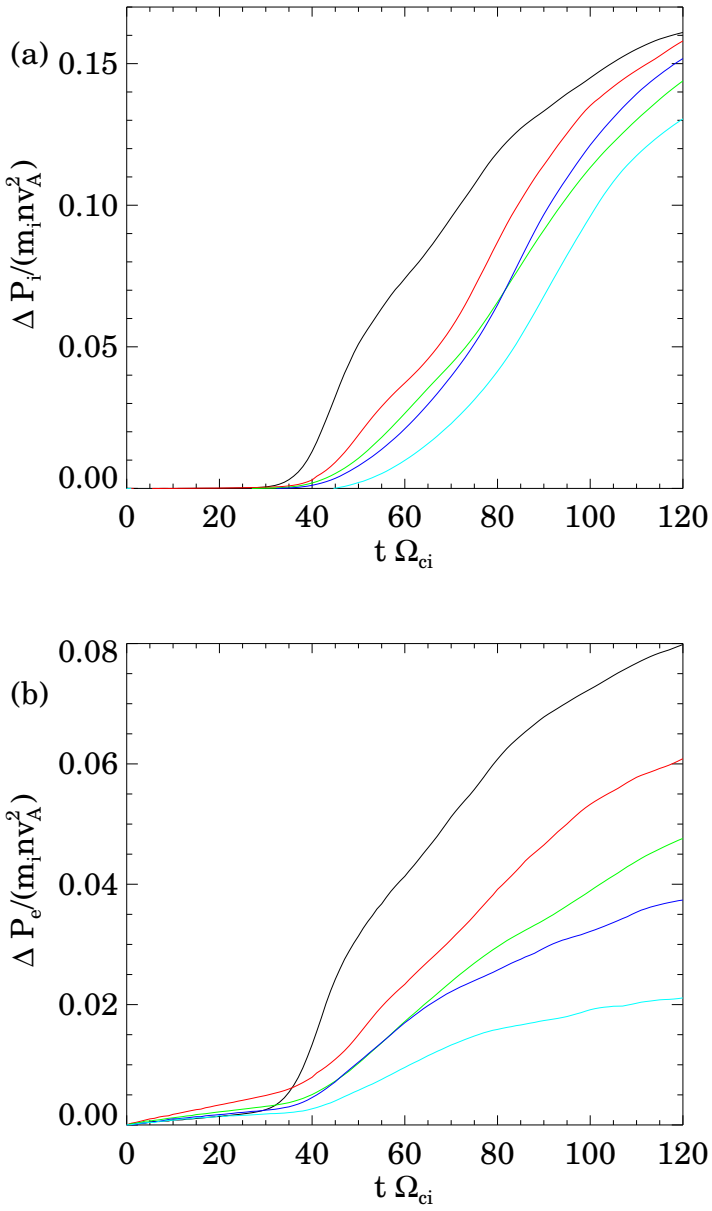

Figure 6.1: The change in average pressure for $\beta = 0.2, 1, 2, 3$, and 4.8, (black, red, green, blue, cyan respectively) contained in the ions (a) and the electrons (b), where the pressure is calculated as the trace of the pressure tensor / 3.

that something is occurring on the spatial scale of electrons.

6.5 Tracking the particles: What energizes them, and what keeps them under control?

We will examine the trajectory of a typical electron, but in order to understand the trajectory of the electron itself, we need to look at what the island in which the electron is located is doing. Figure 4.6 shows islands contracting in the $\beta = 2$ simulation for a particular current sheet. The walls of the islands move inward at Alfvénic speeds, and after $t = 60\Omega_{ci}^{-1}$ the islands begin to show evidence of the Weibel instability, which will be discussed in the next section. The electron of interest is located in the island between $x = 100$ and $150d_i$.

Figure 6.2 shows the trajectory of the electron. As shown in Figure 6.2 (a,b), before $t = 60$, whenever the electron changes directions by bouncing off the end of the island, there is an increase in its energy. As shown in Figure 6.2 (c) the x-velocity switches to z-velocity each time the bounce occurs. The $\hat{\mathbf{x}}$ direction is essentially the parallel direction, since the magnetic fields are mostly in the $\hat{\mathbf{x}}$ direction. The gain in energy is caused by the reconnection electric field which is parallel to the out-of-plane velocity during the bounce.

After the Weibel instability begins to grow around $t = 60\Omega_{ci}^{-1}$, the energy stops increasing. The structure of B_z is shown in Figure 6.2 (e). The structures near the ends of the island at $t < 55\Omega_{ci}^{-1}$ is first onset of the Weibel instability. The structure near the center of the island after $t = 55\Omega_{ci}^{-1}$ is the more developed B_z signature

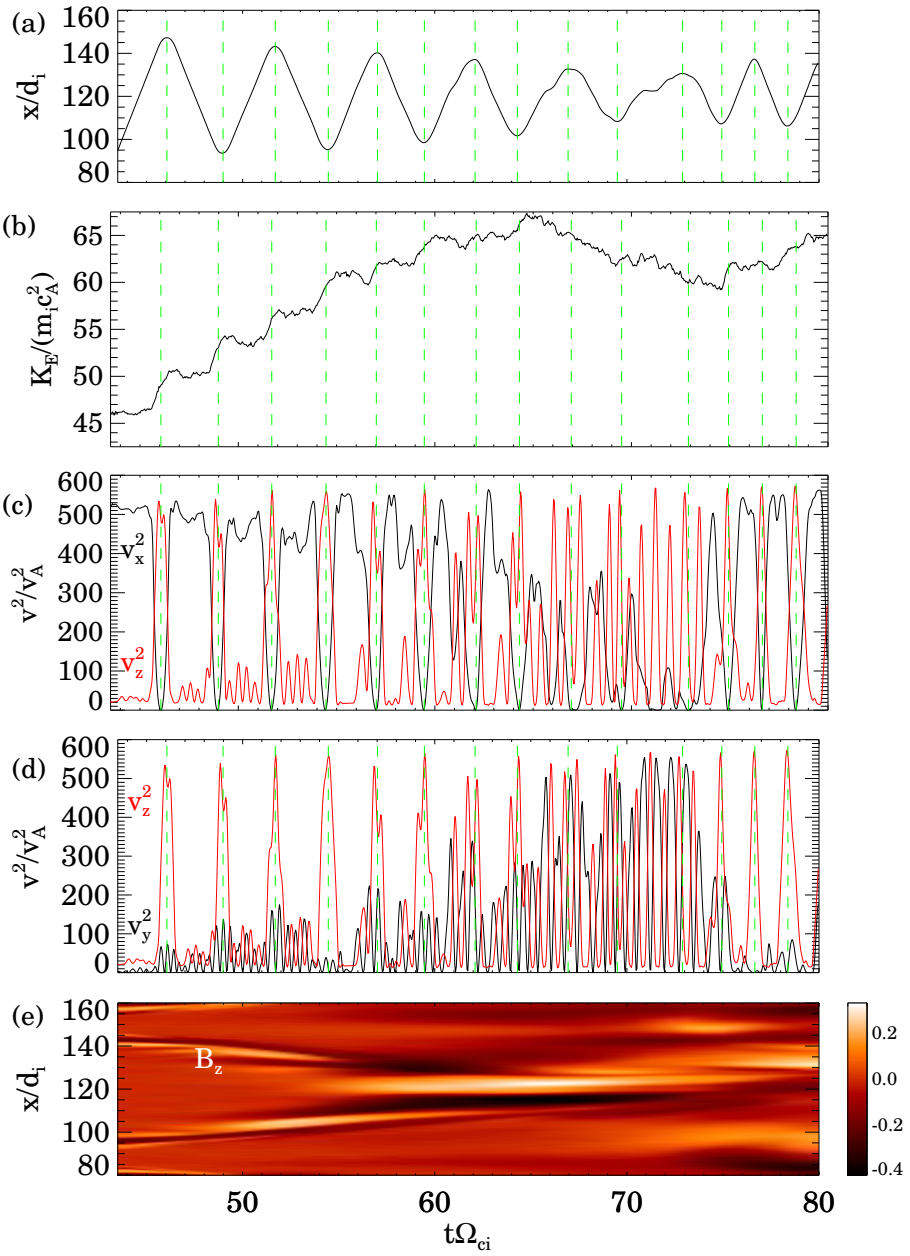

Figure 6.2: The trajectory of an electron; with (a) the x position vs. t, (b) the kinetic energy vs. t, (c) v_x^2 (black) and v_z^2 (red) vs. t, (d) v_y^2 (black) and v_z^2 (red) vs. t, and (e) the out-of-plane magnetic field B_z in a cut along the center of the current sheet of the island vs. t. The tracked particle is from a run with $\beta = 2, t = 43.5 - 80\Omega_{ci}^{-1}$. The green dotted lines are the times where the x velocity changes sign.

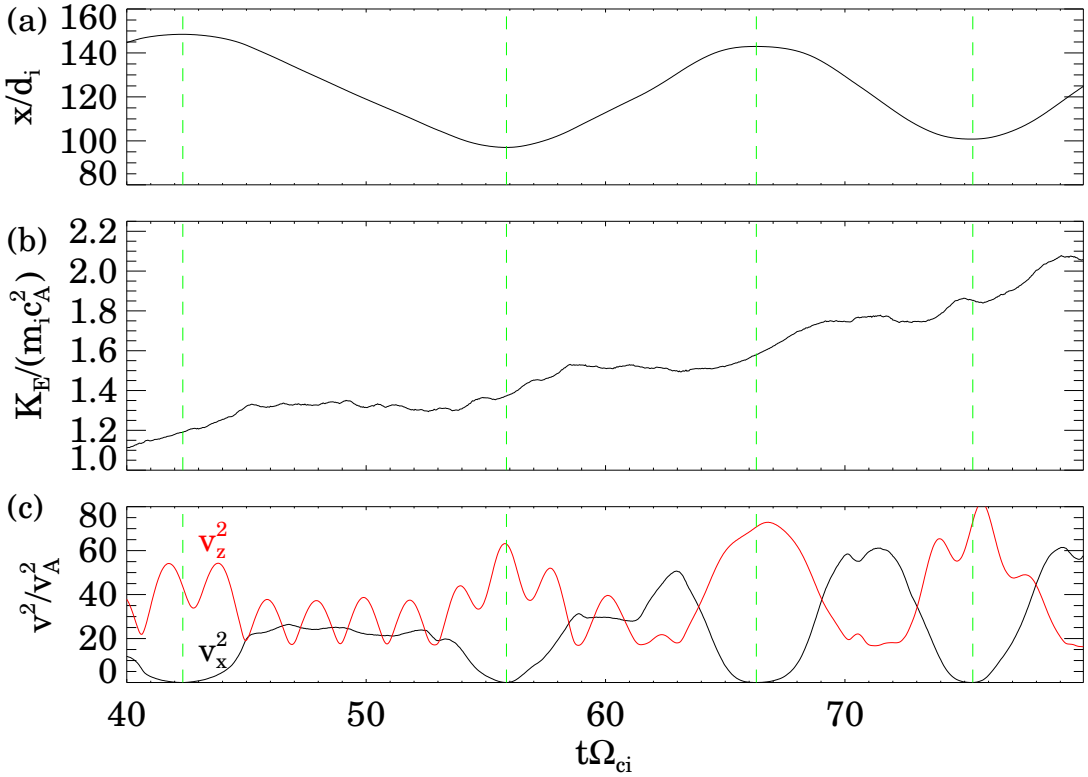

Figure 6.3: The trajectory of an ion; with (a) the x position vs. t, (b) the kinetic energy vs. t, and (c) v_x^2 (black) and v_z^2 (red) vs. t. The tracked particle is from a run with $\beta = 2, t = 43.5 - 80\Omega_{ci}^{-1}$. The green dotted lines are the times where the x velocity changes sign.

of the Weibel instability. The Weibel magnetic fields divert v_x, which is parallel to the reconnecting field, into v_y, which is perpendicular. The primary B_x then rotates the perpendicular velocity as the particle travels in Larmor orbits. The signature of this perpendicular velocity can be seen in the y-velocity shown in Figure 6.2 (d).

Figure 6.3 shows the trajectory of an ion in the same island. This ion, unlike the electron, continues to gain energy throughout the time period where the Weibel

instability is present. The ion acts in the same way as the electron did before $t = 60$. The higher inertia of the moving ions causes the Larmor radius to exceed the length scale of the out-of-plane Weibel field, allowing the ions to pass through without being deflected into the $\hat{\mathbf{y}}$ direction.

The trajectory shown in Figure 6.2 is a typical example of energetic electrons in the system. Nearly all of the tracked electrons are trapped within islands and gain energy. Many of them are deflected in a similar way. The ion in Figure 6.3 was chosen to be in the same island as the electron from Figure 6.2, but its behavior is generally similar to others in the system. Like the electrons nearly all of the ions were trapped within islands, and gained energy.

6.6 But why is heating β dependent?

To better understand the dependence of the heating with β we examine the change in the average of the components of the electron pressure tensor from that at $t = 0$, ΔP_{eij}. In Figure 6.4 we see the growth of the pressure in the $\hat{\mathbf{x}}$ direction P_{exx} for both small and large β. Within islands where much of the temperature anisotropy develops, the magnetic field is predominantly in the $\hat{\mathbf{x}}$ direction. So again, $\hat{\mathbf{x}}$ corresponds to the parallel direction in which the Fermi process accelerates particles. In Figure 6.4 we see that in both low and high β the growth of the parallel pressure significantly drops around $\Delta P_{exx} = 0.05 m_i n v_A^2$. This drop occurs at around $t = 50\Omega_{ci}^{-1}$. In each simulation this drop in growth coincides with the onset of the Weibel instability. Although the onset is not presented for all values of

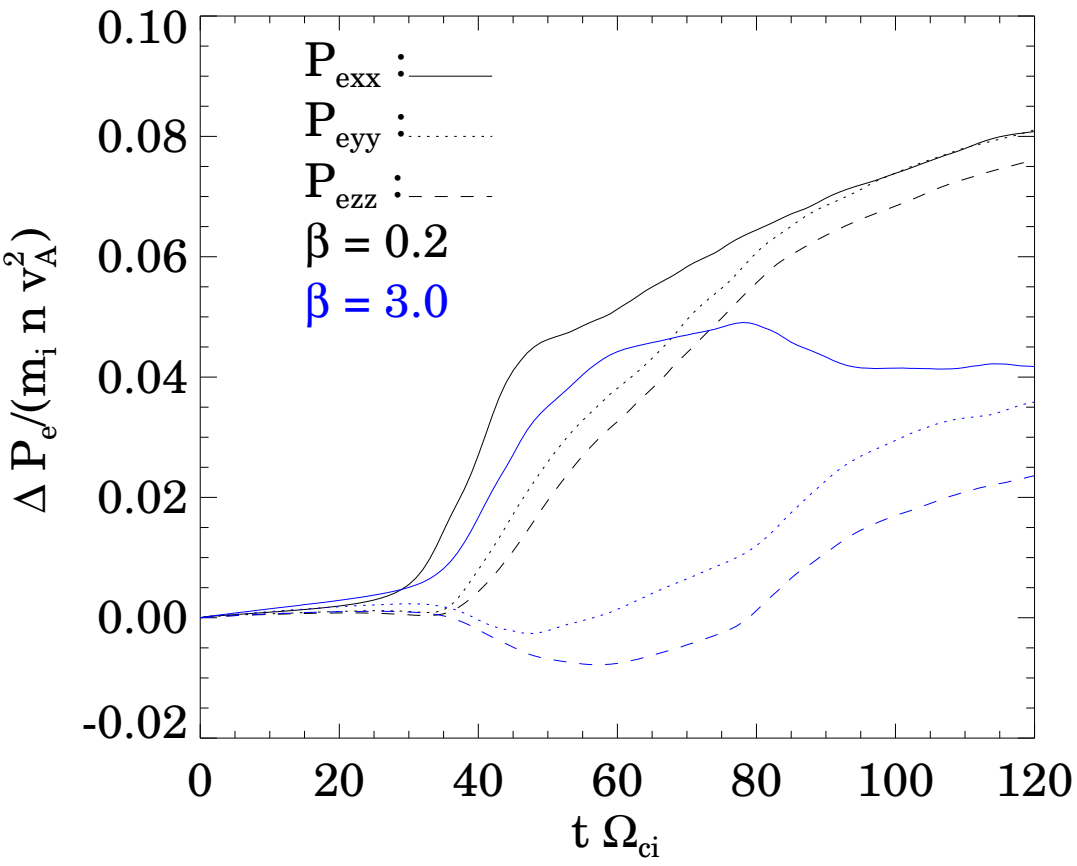

Figure 6.4: The change in average pressure for the electrons for $\beta = 0.2$ and 3, (black and blue respectively), where the diagonal components of the pressure tensor are shown; P_{exx} (solid), P_{eyy} (dotted), and P_{ezz} (dashed).

β, an example of the $\beta = 2$ run is seen in Figure 6.2 (e) for one particular island.

The Weibel instability develops for the same value of ΔP_{exx} for several values of β, two of which are shown in Figure 6.4. After the drop in growth of the parallel pressure, the perpendicular pressure begins to rise for all β, two of which are shown in Figure 6.4. This perpendicular pressure rise is due to the scattering of particles moving parallel to the magnetic field by the Weibel instability. For the $\beta = 3$ case (the blue curves in Figure 6.4), the scattering causes the growth of the parallel pressure to essentially stop. For $\beta = 0.2$ on the other hand, the scattering is not sufficient to completely stop the growth. This difference in scattering implies the heating of particles depends on β.

6.7 Weibel instability spotted

In the regions near the reconnection sites, the outflow streams through the background plasma, giving rise to an anisotropy. In addition, due to Fermi acceleration, anisotropies develop within magnetic islands. In regions of high pressure anisotropy where the magnetic field is nearly zero, a short wavelength mode grows (Figure 6.5). This mode is associated with the Weibel instability. A similar Weibel instability has been found in reconnection simulations [32]. The region of weak magnetic field is a location where the Weibel instability is more likely to develop since the instability normally develops in an unmagnetized plasma with anisotropy. The Weibel instability has a wavevector perpendicular to the direction with higher temperature. Since the weak magnetic field region is confined above and below by

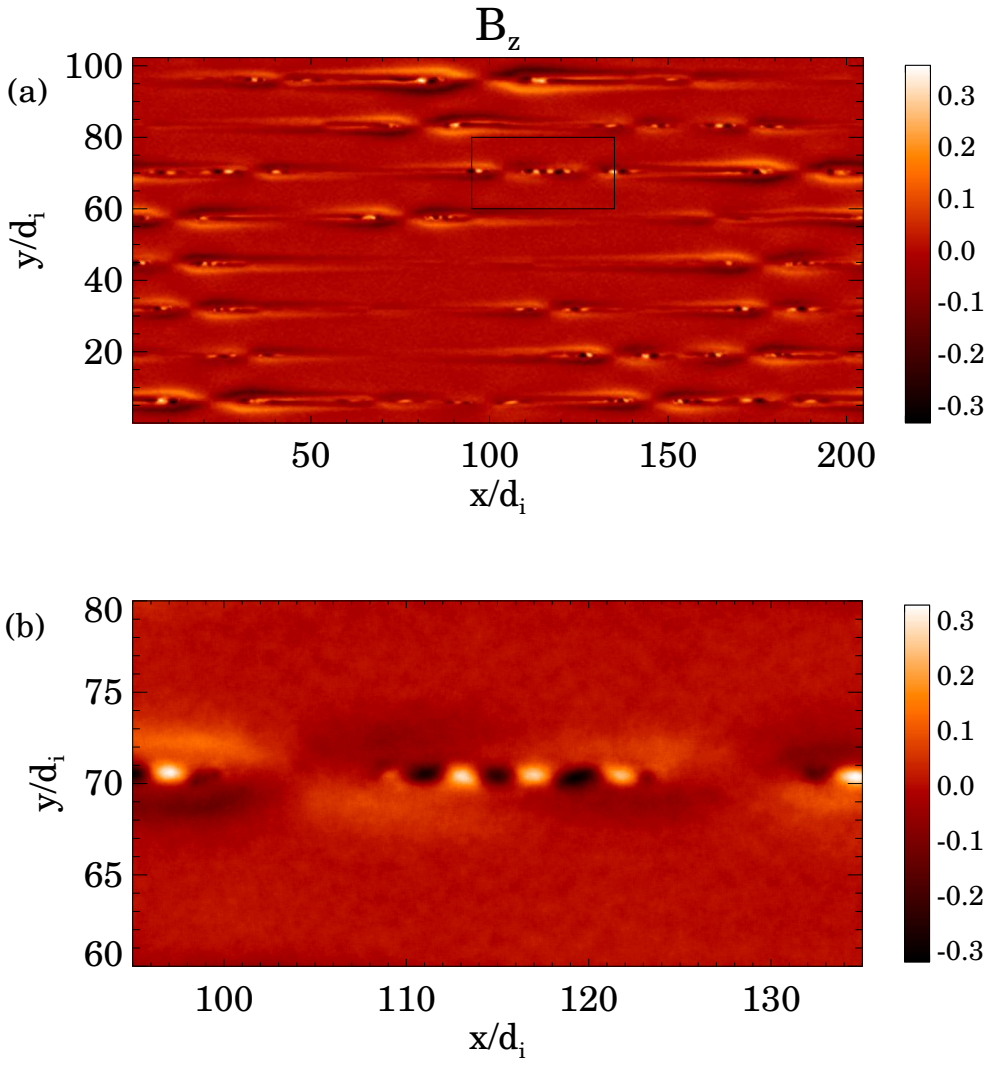

Figure 6.5: Out-of-plane magnetic field, B_z. Short wavelength structures are visible in the low magnetic field regions where the outflow streams through the background plasma. Zoomed in region is shown in (b). Black box in (a) indicates zoomed in region. These structures are due to a Weibel instability. This plot is taken from the $\beta = 2$ case at $t = 45\Omega_{ci}^{-1}$.

magnetic fields, only half a wavelength can form. The conventional linear theory of the Weibel instability does not predict the wave vector in the $\hat{\mathbf{x}}$ direction. However, as shown in Liu et al. [30], a wavevector along the direction of higher temperature can form such that the gyroradius associated with the magnetic field of the mode matches the wavelength. In this case the relevant scale is the electron gyroradius. The out-of-plane magnetic field is approximately $0.3B_0$, $v_{the} \approx 8$, and $m_e = 0.04$ so the gyroradius is about $1d_i$. This is a quarter of the observed wavelength, consistent with the prediction of Liu et al.[30].

As anisotropies grow due to the Fermi process, the entire center of the island becomes unstable to the Weibel instability. As the instability grows into the region where the magnetic field becomes significant but the length scales are still below d_i, whistler dynamics causes the out-of-plane Weibel magnetic fields to rotate into the page, causing small scale kinking, as shown in Figure 4.6.

6.8 Weibel without reconnection

We have performed small, $25.6d_i \times 51.2d_i$, simulations with a specific initial temperature anisotropy in order to better understand the development of the Weibel instability. We use the same space and time resolution as in the larger runs. In these runs we employ a modified Harris sheet with an initial temperature anisotropy with higher initial temperature along the $\hat{\mathbf{x}}$ direction (Note that $T_\parallel$ plays no part in ensuring pressure balance, so varying it does not change the initial equilibrium). We take parameters from the late time $\beta = 2$ simulation, where the Weibel instabil-

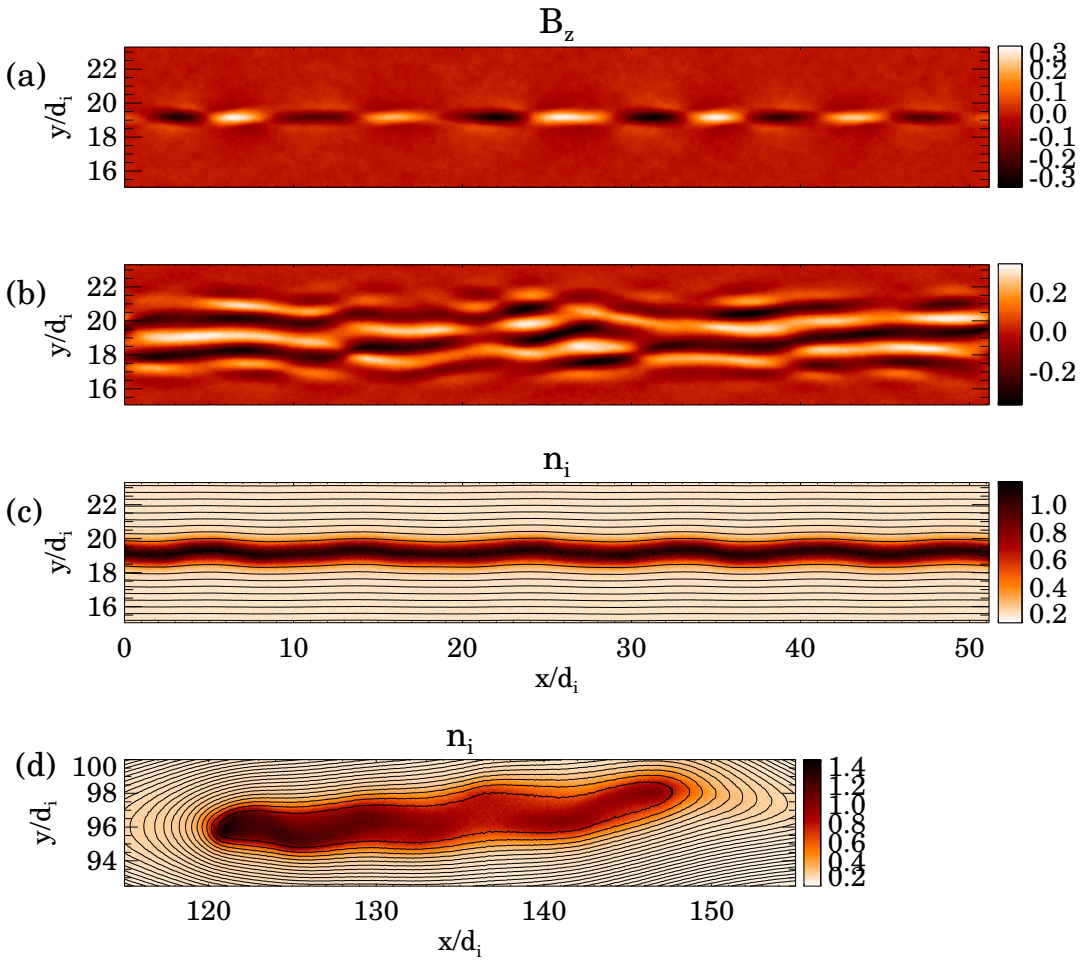

Figure 6.6: Panels, (a),(b), and (c) are taken from a simulation with a modified Harris sheet configuration with initial $T_{\parallel}/T_{\perp} = 3.52$. The B_z structure of the Weibel instability at $t = 0.2\Omega_{ci}^{-1}$ is shown for $w_0 =$ (a) $0.5d_i$ and (b) $4d_i$. The k_y expected from the Weibel instability is clearly visible in (b) while only half a wavelength fits in (a) and a non-zero k_x becomes evident. In (c), a kinking structure in the ion density, n_i, that appears to be an instance of the Weibel instability at $t = 5\Omega_{ci}^{-1}$ is shown, for $w_0 = 0.5d_i$. In (d), plot reveals a similar kinking structure to that seen in (c) for the $\beta = 2$ run at $t = 61\Omega_{ci}^{-1}$. The overplotted curves in (c) and (d) are contours of constant magnetic flux.

ity develops, for which $T_b = 1.75T_0$ (see Figure 6.6). However, in order for the anisotropy to fully grow, the anisotropy was doubled from $T_\parallel/T_\perp = 1.76$ to 3.52. The anisotropy was initiated by varying the temperature in the parallel direction of the Harris population of both the electrons and the ions, as this is what is observed in the $\beta = 2$ reconnection simulation. Note, however, that the Weibel instability is only driven by the electron anisotropy. Finally, we performed more simulations with a variety of anisotropies, for current sheets of width $0.5d_i$ and $4.0d_i$, with both relativistic effects turned on and off. The goal was to demonstrate that the growth rate of the instability in the simulations matches that of the Weibel instability.

We have reproduced this Weibel phenomenon in our small simulation with an initial anisotropy. With the enhanced anisotropy the instability develops until the magnetic fields kink much like what is seen in the larger self generated anisotropy run. (Figure 6.6c,d).

We had to artificially increase the anisotropy in the small simulation to ≈ 3.5 in order to reproduce the Weibel phenomenon. In the $\beta = 2$ reconnection simulation the anisotropy, $T_\parallel/T_\perp \approx 1.8$, is constantly replenished by an influx of plasma from the x-line, and Fermi acceleration. This enables the instability to grow to finite amplitude. Since the anisotropy in the test run is quickly exhausted, a much larger initial anisotropy is needed for the instability to reach large amplitude.

6.9 Is this instability really Weibel?

The instabilities found in the simulations can be identified as the Weibel instability based on agreement with the predicted Weibel growth rates. The non-relativistic growth rate of the Weibel instability is determined from

$$k_y^2 c^2 - \omega^2 + \sum_\alpha \omega_{p\alpha}^2 \left(1 - \frac{T_{\alpha x}}{T_{\alpha y}}\right) = \sum_\alpha \omega_{p\alpha}^2 \frac{T_{\alpha x}}{T_{\alpha y}} \xi_\alpha \, \mathrm{Z}(\xi_\alpha), \tag{6.1}$$

where

$$\xi_\alpha = \frac{\omega}{k_y \sqrt{2T_{\alpha y}/m_\alpha}}, \tag{6.2}$$

Z is the plasma dispersion function,

$$\mathrm{Z}(\xi_\alpha) = \frac{1}{\sqrt{\pi}} \int_{-\infty}^{\infty} \frac{\exp(-x^2)dx}{x - \xi_\alpha}, \tag{6.3}$$

and α is the species [25]. The growth rate is measured as the imaginary part of the frequency, ω.

Since the half width of the current sheet is smaller than the predicted wavelength of the Weibel instability, a clear wave vector along the $\hat{\mathbf{y}}$ direction is not found. To be certain we are seeing the Weibel instability, we performed a run with a current sheet half width, $w_0 = 4d_i$. In this case we observe several wavelengths in the $\hat{\mathbf{y}}$ direction as predicted for the Weibel instability (see Figure 6.6b). We checked the growth rate versus anisotropy and it fits very well with the predicted Weibel growth rate (Figure 6.7). The growth rate in Equation 6.1 depends on both the temperature anisotropy and the wavelength of the mode. We use the observed k_y in the comparison, although it is generally close to the maximally growing wavenumber, $k_y d_i \approx 3$. The growth rate for $w_0 = 0.5d_i$ is a bit smaller than predicted by

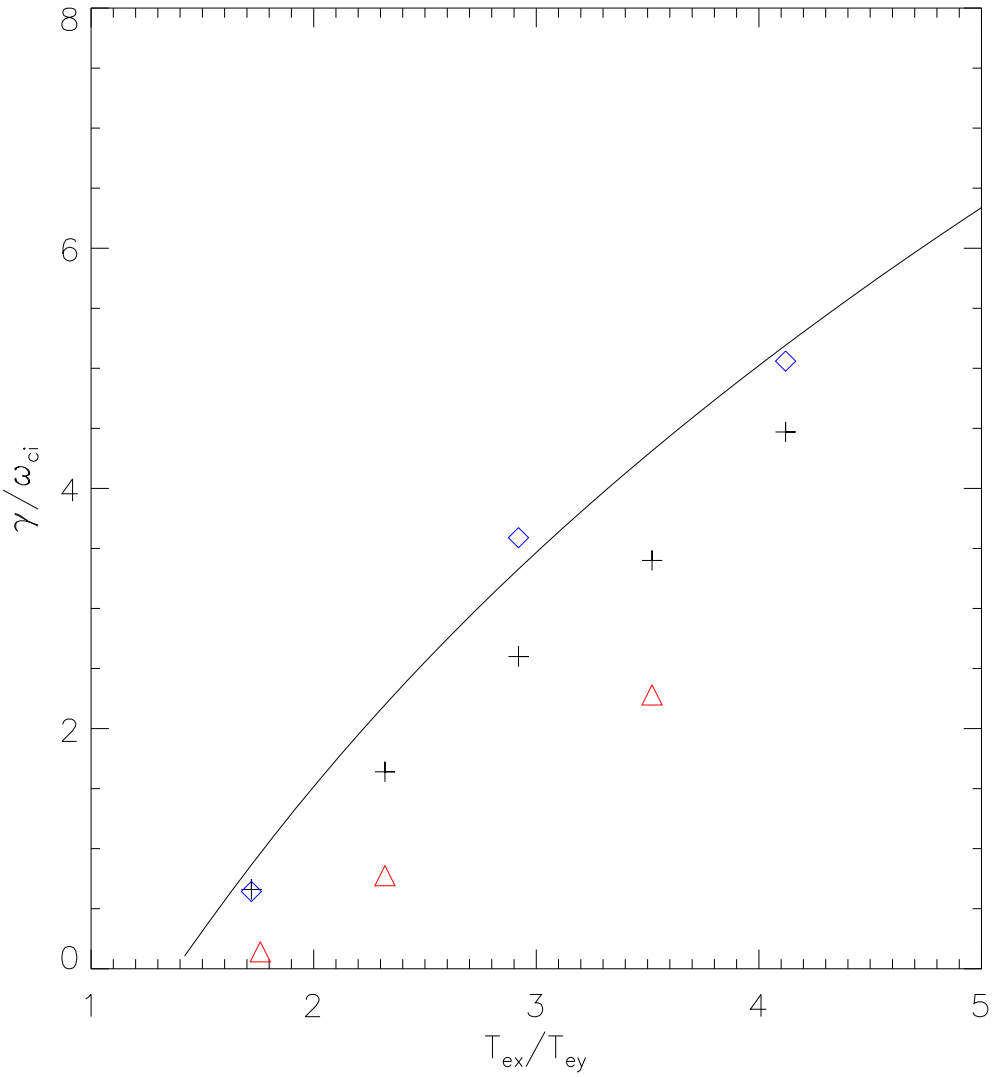

Figure 6.7: Growth rate vs. anisotropy, T_{ex}/T_{ey}. The black plus signs are the growth rate for $w_0 = 4d_i$. The blue diamonds have the same w_0 but the relativistic effects in the code are turned off. The red triangles are for $w_0 = 0.5d_i$. The black curve is the theoretical non-relativistic prediction for the Weibel growth rate.

homogeneous theory because the bounding magnetic fields suppress the growth. We also find that relativistic effects (our electrons have $v_{the}/c = 0.4$) also suppress the growth.

6.10 Conclusions on particle acceleration in high β islands

We find that, based on particle trajectories, first-order Fermi acceleration is the major source of energetic particle acceleration in our simulations of collisionless magnetic reconnection. There is a difference between the ion and electron acceleration because the ions are unaffected by the Weibel generated magnetic fields within the islands while the electrons are scattered. Although we have shown this is the case for the most energetic electrons, in principle nearly all electrons that have high enough velocities to bounce between the ends of an island during its formation and therefore gain energy via the Fermi process. This occurs as long as the speed is super-Alfvénic. For our simulation with $\beta = 0.2$ the thermal velocity $v_{th} = 2.5c_A$ so that most of the electrons are energetic enough to gain energy through the Fermi process.

In the heliosheath, the fields are closer to a force free configuration around the current sheet. This means the field strength stays relatively constant rather than going to nearly zero at the center of the islands. This suggests that the Weibel instability plays a smaller role. However, since the separation between the current sheets is rather large (The ratio of the separation to the width is about 17,000 just upstream of the termination shock), the total out-of-plane flux is rather small. As the

islands grow, the out-of-plane field is swept away and replaced by the anti-parallel flux. The anti-parallel flux leaves a long region with relatively small magnetic field along the current sheet where the Weibel instability can still develop.

We have demonstrated that at the electron scale, anisotropy instabilities can limit the acceleration of electrons. In principle, at larger scales, ion scale instabilities such as the firehose instability would likely develop causing a similar effect on the ions. However, such an anisotropy also suppresses reconnection and reduces the drive for anisotropy. Thus, it is unclear whether strong firehose instability sufficient to scatter ions will take place. We have not yet seen significant ion scattering.

We would thus expect to see a dependence of β on the energetic particles measured from the Voyager spacecraft. Regions with larger β would be expected to have fewer energetic particles, since acceleration would be suppressed in that region.

3D MHD simulations of the global heliosphere [15] had predicted that the pileup of the magnetic field at the heliopause would lead to a region of low β so that the predictions of the present model could be tested. However, even though the radial flows of Voyager 1 have dramatically decreased, no buildup of the magnetic field has been measured. Our interpretation is that reconnection is preventing the buildup of magnetic field. The unfortunate implication is that no direct comparison of particle acceleration in different β regimes will be possible with the Voyager measurements alone.

In accretion discs, the gravitational energy is released, and the plasma gets heated generating radiation and energetic particles that can be measured. The gravitational energy release is proportional to the radial-azimuthal component of

the stress tensor, which transports angular momentum outward and thus allows the release of gravitational energy. The stress however, is not proportional to the increase in thermal energy. Rather, it is proportional to the magnetic energy. The generation of magnetic field energy is caused by the magnetorotational instability (MRI), which is also the source of the stress. The total magnetic field produced as a result of the release of gravitational energy by the MRI is more than 3 times the kinetic energy [61]. Since magnetic reconnection is the dominant mechanism for releasing magnetic energy, our simulations should thus shed light on the how heating and particle acceleration develop, which would allow comparison with measurements.

Chapter 7

Conclusion

7.1 Summary of results

We have shown that there is a vastly different picture in the heliosheath than the conventional understanding. Much of the heliosheath consists of a sea of elongated magnetic island structures. Throughout the course of this thesis we have shown that magnetic islands in the heliosheath are relevant and are strongly affected by pressure anisotropies, and enhanced levels of β due to the PUI population. The shape of the islands is affected, the islands quickly grow to the point of being volume filling in most of the heliosheath, and energization of particles is limited.

We have shown that at large β, pressure anisotropies form that have a major impact on the dynamics of island formation, and evolution. The extent of these anisotropies is limited by the anisotropy levels where anisotropy instabilities begin to occur. The length of islands forming from a Harris equilibrium is proportional to the square root of both the electron plasma beta, β_e, and the mass ratio, m_i/m_e. At high β islands are capable of sustaining large aspect ratios without contracting into a circle.

These magnetic islands take up a significant portion of the heliosheath, because they continue to grow until they fill the sectored region. We have shown through a scaling argument that islands should grow to the separation width of magnetic

sectors in the heliosheath. Note that this means the islands become thousands of times bigger than the initial d_i scale islands that form initially. If a current sheet is long enough compared to the separation width, islands will continue to grow with large aspect ratios by merging.

Finally we have shown that due to the same pressure anisotropies that cause high aspect ratio islands, anisotropy instabilities can form. The instabilities can limit the energization of particles which are energized by the Fermi process in contracting islands. We also find that there is a β dependence on this limiting of energization. We identify the Weibel instability, one of these anisotropy instabilities, as growing in our simulations. The electron energization is limited by the eventual scattering by Weibel magnetic fields. The anisotropy, $P_{\parallel}/P_{\perp}$, cutoff is smaller for large β because, the instability begins to develop at a value of ΔP_e which is relatively constant.

7.2 Implications and future work

These results imply that magnetic islands should be prevalent in the heliosheath. The elongated islands should cause anisotropic distributions of magnetic fields, so that more magnetic energy is in the azimuthal direction. This is both something that can be measured, and may have an effect on the transport of the energetic ACRs. ACRs should diffuse through the heliosheath if it consists of a bath of magnetic islands. In the case of elongated islands, ACRs should diffuse faster in the azimuthal direction.

We have concluded that the acceleration of particles should be limited by

anisotropy instabilities. We should thus be able to see limits on ACR and energetic electron energy distributions. It is still an open question which instabilities should play the more significant role. A quantitative measure for the maximum energy a particle will gain before being scattered by instabilities is yet to be determined.

As mentioned earlier there are other possible systems where magnetic islands should develop at high β. Theses systems include accretion discs, where the MRI develops and turbulent generated magnetic fields release energy via reconnection, in the magnetosphere of Saturn, and even at certain places in the Earth's magnetosphere.

Appendix A

The Frozen-in Condition

The frozen in theorem states that the magnetic flux through a particular fluid element remains constant. This means that if you integrate the flux through a surface, Σ, and follow the motion of that surface due to flow perpendicular to the magnetic field, the flux remains constant. In other words the total derivative of the flux is zero,

$$\frac{d}{dt}\Phi = 0 \tag{A.1}$$

, where the flux is defined as:

$$\Phi = \int \mathbf{B} \cdot \mathbf{dA}. \tag{A.2}$$

The total derivative of the flux can then be broken up into the local time derivative, and the change due to motion of integrated surface,

$$\frac{d}{dt}\Phi = \int \frac{\partial \mathbf{B}}{\partial t} \cdot \mathbf{dA} + \oint B\mathbf{v} \cdot \left(\mathbf{dl} \times \hat{\mathbf{b}}\right), \tag{A.3}$$

where $\hat{\mathbf{b}}$ is the unit vector in the direction of the magnetic field. The first term is the change in flux contained in the present surface, Σ. The second term is the flux added or lost due to the motion of Σ. The flux added is the product of the component of the magnetic field perpendicular to the normal of the curve enclosing Σ, $\mathbf{dl} \times \hat{\mathbf{b}}$, and the fluid velocity. Equation (A.3) can be simplified using the vector identity $\mathbf{A} \cdot (\mathbf{B} \times \mathbf{C}) = \mathbf{C} \cdot (\mathbf{A} \times \mathbf{B})$.

$$\frac{d}{dt}\Phi = \int \frac{\partial \mathbf{B}}{\partial t} \cdot \mathbf{dA} - \oint \mathbf{v} \times \mathbf{B} \cdot \mathbf{dl} \tag{A.4}$$

Now that we have established a condition for the magnetic fields to be frozen into the velocity field, we will show that this is the case for a reasonable set of assumptions. Before making any assumptions, we start with Faraday's law.

$$\frac{\partial \mathbf{B}}{\partial t} = -c\nabla \times \mathbf{E} \tag{A.5}$$

For resistive MHD, the generalized Ohms law is:

$$\mathbf{E} = -\frac{\mathbf{v} \times \mathbf{B}}{c} + \eta \mathbf{j}. \tag{A.6}$$

Inserting Equation (A.6) in Equation (A.5), and integrating over an area, we obtain:

$$\int \frac{\partial \mathbf{B}}{\partial t} \cdot \mathbf{dA} = \int \nabla \times (\mathbf{v} \times \mathbf{B} - \eta c \mathbf{j}) \cdot \mathbf{dA}. \tag{A.7}$$

Using Stokes' theorem,

$$\int \frac{\partial \mathbf{B}}{\partial t} \cdot \mathbf{dA} = \oint (\mathbf{v} \times \mathbf{B} - \eta c \mathbf{j}) \cdot \mathbf{dl}. \tag{A.8}$$

Therefore using the expression for the change in flux from Equation (A.4) we find that

$$\frac{d}{dt}\Phi = -\oint \eta c \mathbf{j} \cdot \mathbf{dl}. \tag{A.9}$$

For small η the flux following a particular field line is conserved. Generally η is very small in the solar wind, including the heliosheath. Other terms not present in the MHD equations, although generally small, can play a role in the breaking the frozen-in condition in special cases such as regions of reconnection. These terms are found in the Generalized Ohms law, Equation (2.2).

Appendix B

The Resistive Tearing Instability

When there is a sharp change in the direction of the magnetic field in a plasma, an instability known as the tearing instability can form. The tearing instability is a linear instability that can be derived from the basic incompressible resistive MHD equations. The two relevant equations are the momentum equation,

$$mn\frac{\partial \mathbf{v}}{\partial t} = -\nabla P + \frac{\mathbf{j}\times\mathbf{B}}{c}, \tag{B.1}$$

where $\mathbf{j} = c\nabla\times\mathbf{B}/4\pi$, and the induction equation,

$$\frac{\partial \mathbf{B}}{\partial t} = \nabla\times(\mathbf{v}\times\mathbf{B}) + \frac{\eta c^2}{4\pi}\nabla^2\mathbf{B}. \tag{B.2}$$

We start with the equilibrium conditions, $\mathbf{v_0}$, $\mathbf{B_0}$, n_0, and P_0. $\mathbf{B_0}$ is directed in the $\hat{\mathbf{x}}$ direction and depends only on y. The equilibrium velocity, $\mathbf{v_0}$, is zero everywhere. n_0 and P_0 are chosen such that the pressure in the current sheet balances the magnetic pressure associated with the asymptotic magnetic field. Since P_0 is not part of any nonlinear terms, the pressure profile does not play a role in the instability.

Taking only the first order terms in $\mathbf{v}$, $\mathbf{B}$, n, and P, we obtain the first order momentum equation,

$$mn_0\frac{\partial \mathbf{v_1}}{\partial t} = -\nabla P_1 + \frac{(\nabla\times\mathbf{B_1})}{4\pi}\times\mathbf{B_0} + \frac{(\nabla\times\mathbf{B_0})}{4\pi}\times\mathbf{B_1}, \tag{B.3}$$

and the first order induction equation,

$$\frac{\partial \mathbf{B_1}}{\partial t} = \nabla \times (\mathbf{v_1} \times \mathbf{B_0}) + \frac{\eta c^2}{4\pi} \nabla^2 \mathbf{B_1}. \tag{B.4}$$

We can assume that the fluid is incompressible because for small perturbations in velocity, the velocity is small compared to the sound speed. We thus can use the properties:

$$\nabla \cdot \mathbf{v_1} = 0, \quad \nabla \cdot \mathbf{B_1} = 0. \tag{B.5}$$

Taking the curl of Equation (B.3) conveniently eliminates the pressure term, so Equations (B.3) and (B.4) are left with two vector equations, and two unknowns, $\mathbf{v_1}$ and $\mathbf{B_1}$. We therefore have a closed set of equations. We assume a perturbation of the form,

$$A = A(y) e^{ikx + \gamma t}. \tag{B.6}$$

After taking the z component of the curl, Equation (B.3) becomes

$$\gamma 4\pi m n_0 \left(i k v_{y1} - \frac{\partial}{\partial y} v_{x1} \right) = -ikB_{x0} \frac{\partial}{\partial y} B_{x1} - B_{y1} \left(k^2 B_{x0} + \frac{\partial^2}{\partial y^2} B_{x0} \right). \tag{B.7}$$

Using Equation (B.5), we can multiply both sides by k and substitute, kv_{x1} with $i\partial v_{y1}/\partial y$, and kB_{x1} with $i\partial B_{y1}/\partial y$. We are now left with

$$\gamma 4\pi m n_0 \left(i k^2 v_{y1} - i \frac{\partial^2}{\partial y^2} v_{y1} \right) = kB_{x0} \frac{\partial^2}{\partial y^2} B_{y1} - B_{y1} \left(k^2 B_{x0} + \frac{\partial^2}{\partial y^2} B_{x0} \right). \tag{B.8}$$

After reorganizing, we obtain.

$$\gamma B_{x0} \left(\frac{\partial^2}{\partial y^2} - k^2 \right) v_{y1} = ikc_A^2 \left(\frac{\partial^2}{\partial y^2} - k^2 - \frac{1}{B_{x0}} \frac{\partial^2}{\partial y^2} B_{x0} \right) B_{y1}, \tag{B.9}$$

where $c_A^2 = B_{x0}^2 / 4\pi m n_0$. The y component of Equation (B.4) is

$$\gamma B_{y1} = ikB_{x0} v_{y1} + \frac{\eta c^2}{4\pi} \left(\frac{\partial^2}{\partial y^2} - k^2 \right) B_{y1}. \tag{B.10}$$

If you examine Equations (B.9) and (B.10), you may notice that B_{y1}, and v_{y1} are now serendipitously decoupled from the other variables.

The problem is still a set of two second order differential equations, with coefficients that depend on y, and thus is difficult to solve analytically. To help solve the problem, we make the assumption that there are three timescales that can be ordered as follows, $\tau_H \gg \tau_{Hb} \gg \tau_R$[18]. These are the hydrodynamic, hybrid, and resistive timescales, respectively. Since there is a sharp change in magnetic field across the current sheet, this can be treated as a boundary layer problem.

Outside of the current sheet, the frozen-in condition holds, and we can neglect the term that has a factor of η in Equation (B.10), this term changes at a timescale of $\tau_R = 4\pi w_0^2/\eta$, compared to the growth rate, γ, which changes as τ_{Hb}. In addition we can neglect the he left hand side of Equation (B.9), because it changes as τ_{Hb}, which is slow compared to the right hand side, which changes as $\tau_H = w_0/c_A$. We can solve for the solution on either side of the current sheet and match them together.

We can solve this equation using the constraint that the perturbation must go to zero as y approaches the asymptotic magnetic field region, where B_{x0} is constant with respect to y. In addition B_{y1} must be continuous across the current sheet, while the derivative does not. For the Harris sheet equilibrium configuration Equation (2.3), the solutions for positive and negative y are:

$$B_{y1\pm} = C_0 e^{\mp ky}\left(1 + \frac{\tanh(\pm y/w_0)}{kw_0}\right). \tag{B.11}$$

This solution has an unspecified multiplicative constant, C_0. In order to remove the unspecified constant, it is natural to measure the discontinuous jump in

the slope of B_{y1} as:

$$\Delta' = \left[\frac{1}{B_{y1}}\frac{\partial B_{y1}}{\partial y}\right]_{0_-}^{0_+}. \tag{B.12}$$

This term is also known as the tearing stability index. If it is larger than zero the mode is unstable, while if it is negative the mode is stable. We will show this is the case below.

For the Harris sheet,

$$\Delta' = -2k\left[1 - \frac{1}{k^2 w_0^2}\right]. \tag{B.13}$$

Modes are thus unstable when $kw_0 < 1$. This is approximately the case for all equilibrium conditions.

At this point we have not looked into what breaks the frozen-in condition. What happens inside the current sheet determines the growth rate. Since we are using resistive MHD to derive the tearing mode, resistivity breaks the frozen-in condition, so we will examine the resistive tearing mode.

Inside of the current sheet the y derivative reaches its maximum, such that $\partial^2/\partial y^2 \gg k^2$ and $\partial^2/\partial y^2 \gg B''_{x0}/B_{x0}$. At this point the resistivity is breaking the frozen in condition, and thus we are looking at the resistive tearing instability. Equations (B.9) and (B.10) are reduced to

$$\gamma B_{x0}\frac{\partial^2}{\partial y^2}v_{y1} = ikc_A^2\frac{\partial^2}{\partial y^2}B_{y1}, \tag{B.14}$$

and

$$\gamma B_{y1} = ikB_{x0}v_{y1} + \frac{\eta c^2}{4\pi}\frac{\partial^2}{\partial y^2}B_{y1}. \tag{B.15}$$

These equations are not trivial to solve, but after some effort involving Γ

functions, an expression of the growth rate can be obtained.[1]

$$\gamma \approx 0.55 \frac{(\Delta' w_0)^{4/5}}{\tau_{Hb}} \tag{B.16}$$

We use the hybrid scale we had defined earlier for the time scale of the growth of the tearing instability. The hybrid scale now has a more rigorous definition,

$$\tau_{Hb} = \tau_H^{2/5} \tau_R^{3/5} = \tau_H S^{3/5}. \tag{B.17}$$

The growth rate in Equation (B.16) is also a function of the stability parameter, Δ'. Since for a negative number taken to the 4/5 power, the real part is always negative, the system is damped and therefore stable when $\Delta' < 0$.

The previous γ is calculated assuming the resistivity breaks the frozen-in condition. This problem can also be solved assuming other terms break the frozen-in condition, and in that case the growth rate of the collisionless tearing instability is obtained.

[1]The 0.55 term comes from the expression, $(\Gamma(1/4)/2\pi\Gamma(3/4))^{4/5}$

Appendix C

The Firehose Instability

When there is a pressure anisotropy in the direction of the magnetic field in a plasma, such that $P_\parallel > P_\perp$, an instability known as the firehose instability can develop. The firehose instability is a linear instability that can be derived from the basic MHD equations with an anisotropic pressure tensor. The two relevant equations are the momentum equation, Equation (3.8),

$$mn\left(\frac{\partial \mathbf{v}}{\partial t} + \mathbf{v}\cdot\nabla\mathbf{v}\right) = -\nabla\left(P_\perp + \frac{B^2}{8\pi}\right) + \nabla\cdot\left[\left(1 - \frac{\beta_\parallel - \beta_\perp}{2}\right)\frac{\mathbf{BB}}{4\pi}\right], \tag{C.1}$$

and the induction equation,

$$\frac{\partial \mathbf{B}}{\partial t} = \nabla\times(\mathbf{v}\times\mathbf{B}) \tag{C.2}$$

We start with the equilibrium conditions, $\mathbf{v_0}$, $\mathbf{B_0}$, n_0, $P_{\parallel 0}$, and $P_{\perp 0}$. $\mathbf{B_0}$ is directed in the $\hat{\mathbf{x}}$ direction and is uniform. The equilibrium velocity, $\mathbf{v_0}$, is zero everywhere. n_0, $P_{\parallel 0}$, and $P_{\perp 0}$ are all uniform and can be of arbitrary value.

Taking only the first order terms in $\mathbf{v}$, $\mathbf{B}$, n, and P, and defining

$$\epsilon = \left(1 - \frac{\beta_\parallel - \beta_\perp}{2}\right), \tag{C.3}$$

we obtain the first order momentum equation,

$$mn_0\frac{\partial \mathbf{v_1}}{\partial t} = -\nabla\left(P_\perp + \frac{\mathbf{B_1}\cdot\mathbf{B_0}}{4\pi}\right) + \nabla\cdot\left(\epsilon_0\frac{\mathbf{B_0B_1} + \mathbf{B_1B_0}}{4\pi} + \epsilon_1\frac{\mathbf{B_0B_0}}{4\pi}\right), \tag{C.4}$$

and the first order induction equation,

$$\frac{\partial \mathbf{B_1}}{\partial t} = \nabla\times(\mathbf{v_1}\times\mathbf{B_0}). \tag{C.5}$$

The momentum equation can be simlified greatly by looking only at the components perpendicular to the equilibrium magnetic field.

$$mn_0 \frac{\partial \mathbf{v}_{\perp \mathbf{1}}}{\partial t} = -\nabla_\perp \left(P_{\perp 1} + \frac{\mathbf{B_1} \cdot \mathbf{B_0}}{4\pi} \right) + \nabla \cdot \left(\epsilon_0 \frac{\mathbf{B_0 B}_{\perp \mathbf{1}}}{4\pi} \right) \tag{C.6}$$

If we do likewise with the induction equation, Equation (C.5), we obtain:

$$\frac{\partial \mathbf{B}_{\perp \mathbf{1}}}{\partial t} = \nabla_\parallel \times \left(\mathbf{v}_{\perp \mathbf{1}} \times \mathbf{B_0} \right). \tag{C.7}$$

Taking the curl of Equation (C.4) conveniently eliminates the pressure term. Unfortunately, since we have changed from a pure gradient in Equation (C.4) to a perpendicular gradient in Equation (C.6), this trick does not work anymore. However, with a slight modification using $\nabla_\perp \times$ in place of the curl we can acheive the same effect. This transforms Equations (C.6) and (C.5) into two vector equations, and two unknowns, $\mathbf{v}_{\perp \mathbf{1}}$ and $\mathbf{B}_{\perp \mathbf{1}}$. We therefore have a closed set of equations.

If we now assume a perturbation of the form,

$$A = A_0 e^{i\mathbf{k}\cdot\mathbf{x} + \gamma t}, \tag{C.8}$$

after taking the "perpendicular" curl, Equation (C.6) becomes

$$\begin{aligned} i\gamma m n_0 \mathbf{k}_\perp \times \mathbf{v}_{\perp \mathbf{1}} &= -\epsilon_0 \mathbf{k}_\perp \times \left[\mathbf{k} \cdot \left(\frac{\mathbf{B_0 B}_{\perp \mathbf{1}}}{4\pi} \right) \right] \\ &= -\frac{\epsilon_0 k_\parallel B_0}{4\pi} \mathbf{k}_\perp \times \mathbf{B}_{\perp \mathbf{1}}, \end{aligned} \tag{C.9}$$

while Equation (C.7) becomes

$$\gamma \mathbf{B}_{\perp \mathbf{1}} = i\mathbf{k}_\parallel \times \left(\mathbf{v}_{\perp \mathbf{1}} \times \mathbf{B_0} \right). \tag{C.10}$$

Substituting Equation (C.10) into Equation (C.9), we obtain an equation with only $\mathbf{v}_{\perp\mathbf{1}}$.

$$\gamma^2 m n_0 \mathbf{k}_\perp \times \mathbf{v}_{\perp\mathbf{1}} = -\frac{\epsilon_0 k_\parallel B_0}{4\pi} \mathbf{k}_\perp \times \left[\mathbf{k}_\parallel \times (\mathbf{v}_{\perp\mathbf{1}} \times \mathbf{B_0})\right]. \tag{C.11}$$

This can be written a bit more cleanly as

$$\gamma^2 \mathbf{k}_\perp \times \mathbf{v}_{\perp\mathbf{1}} = -\epsilon_0 c_A^2 k_\parallel \mathbf{k}_\perp \times \left[\mathbf{k}_\parallel \times \left(\mathbf{v}_{\perp\mathbf{1}} \times \hat{\mathbf{b}}\right)\right]. \tag{C.12}$$

where $c_A^2 = B_0^2/4\pi m n_0$, and $\hat{\mathbf{b}} = \mathbf{B_0}/B_0$. If we then use the vector identity, $\mathbf{A} \times (\mathbf{B} \times \mathbf{C}) = \mathbf{A} \cdot \mathbf{CB} - \mathbf{A} \cdot \mathbf{BC}$, we can simplify further.

$$\gamma^2 \mathbf{k}_\perp \times \mathbf{v}_{\perp\mathbf{1}} = -\epsilon_0 c_A^2 k_\parallel^2 \mathbf{k}_\perp \times \mathbf{v}_{\perp\mathbf{1}} \tag{C.13}$$

This equation generates the dispersion relation:

$$\gamma^2 = -\epsilon_0 c_A^2 k_\parallel^2 \tag{C.14}$$

We can see here that when ϵ_0 is negative, we obtain a real value for the growth rate, and thus it is unstable to the firehose instability. If $\epsilon_0 = 1$, Equation (C.14) becomes the standard dispersion equation for Alfvén waves.

Appendix D

The Weibel Instability

When there is a pressure anisotropy in an arbitrary the direction in a plasma with a small magnetic field, such that $P_x > P_y$, an instability known as the Weibel instability can develop. The Weibel instability is a linear instability that can be derived from kinetic theory using the Vlasov equation and Maxwell's equations, implementing an anisotropic velocity distribution. We will look into a derivation of the instability based on one from Krall and Trivelpiece[25]. The two relevant equations to begin the derivation are the Vlasov equation,

$$\frac{\partial f_\alpha}{\partial t} + \mathbf{v} \cdot \nabla f_\alpha + (\mathbf{E} + \mathbf{v} \times \mathbf{B}/c) \cdot \nabla_{\mathbf{v}} f_\alpha = 0, \tag{D.1}$$

and the wave equation based on Maxwell's equations,

$$\nabla \times (\nabla \times \mathbf{E}) = -\frac{1}{c^2}\frac{\partial^2 \mathbf{E}}{\partial t^2} + \frac{4\pi}{c^2}\frac{\partial \mathbf{J}}{\partial t} \tag{D.2}$$

The α subscript represents the species of interest, for instance electrons or ions. $\nabla_{\mathbf{v}}$ is the gradient in velocity space.

We start with the equilibrium conditions, $\mathbf{E_0} = \mathbf{B_0} = 0$, and the distribution function $f_\alpha = f_\alpha\left(v_x^2, v_y^2, v_z^2\right)$. Taking only the first order terms in $\mathbf{E}$, $\mathbf{B}$, and f_α, we assume a perturbation of the form,

$$A = A_0 e^{i\mathbf{k}\cdot\mathbf{x}+\gamma t}. \tag{D.3}$$

From this we are left with the first order equations,

$$-i\omega f_{\alpha 1} + i\mathbf{v}\cdot\mathbf{k} f_{\alpha 1} + \frac{q_\alpha}{m_\alpha}\left(\mathbf{E_1} + \frac{\mathbf{v}\times\mathbf{B_1}}{c}\right)\cdot\nabla_{\mathbf{v}} f_{\alpha 0} = 0, \tag{D.4}$$

and

$$-\mathbf{k}\times(\mathbf{k}\times\mathbf{E_1}) = \frac{\omega^2}{c^2}\mathbf{E_1} + \frac{4\pi}{c^2}\frac{\partial \mathbf{J_1}}{\partial t}. \tag{D.5}$$

These two equations can be combined, by using the definition of $\mathbf{J}$,

$$\mathbf{J} = \sum_\alpha q_\alpha n_{\alpha 0}\int d^3\mathbf{v}\mathbf{v} f_\alpha \tag{D.6}$$

and we thus obtain,

$$-\mathbf{k}\times(\mathbf{k}\times\mathbf{E_1}) = \frac{\omega^2}{c^2}\mathbf{E_1} + \sum_\alpha \frac{4\pi q_\alpha^2 n_{\alpha 0}}{m_\alpha c^2}\int d^3\mathbf{v}\mathbf{v}\frac{\omega\left(\mathbf{E_1} + \mathbf{v}\times\mathbf{B_1}/c\right)}{\omega - \mathbf{v}\cdot\mathbf{k}}\cdot\nabla_{\mathbf{v}} f_{\alpha 0}. \tag{D.7}$$

Using Faraday's law we can substitute, $\omega\mathbf{B_1}/c = \mathbf{k}\times\mathbf{E_1}$, and use some vector identities.

$$k^2\mathbf{E_1} - \mathbf{k}\cdot\mathbf{E_1}\mathbf{k} - \frac{\omega^2}{c^2}\mathbf{E_1} - \sum_\alpha \frac{\omega_{p\alpha}^2}{c^2}\int d^3\mathbf{v}\mathbf{v}\frac{\omega\mathbf{E_1} + \mathbf{v}\cdot\mathbf{E_1}\mathbf{k} - \mathbf{v}\cdot\mathbf{k}\mathbf{E_1}}{\omega - \mathbf{v}\cdot\mathbf{k}}\cdot\nabla_{\mathbf{v}} f_{\alpha 0} = 0. \tag{D.8}$$

Now we can simply further remembering that integrating by parts, $\int d^3\mathbf{v}\mathbf{v}\mathbf{E_1}\cdot\nabla_{\mathbf{v}} f_{\alpha 0} = -\mathbf{E_1}$.

$$k^2\mathbf{E_1} - \mathbf{k}\cdot\mathbf{E_1}\mathbf{k} - \frac{\omega^2}{c^2}\mathbf{E_1} + \sum_\alpha \frac{\omega_{p\alpha}^2}{c^2}\mathbf{E_1} - \sum_\alpha \frac{\omega_{p\alpha}^2}{c^2}\int d^3\mathbf{v}\mathbf{v}\frac{\mathbf{v}\cdot\mathbf{E_1}\mathbf{k}}{\omega - \mathbf{v}\cdot\mathbf{k}}\cdot\nabla_{\mathbf{v}} f_{\alpha 0} = 0. \tag{D.9}$$

We now examine the $\hat{\mathbf{x}}$ component of this equation, which is one of the components perpendicular to $\mathbf{k} = k\hat{\mathbf{y}}$. Notice the terms with components of the electric field, E_{y1} and E_{z1}, drop out because we integrate over an odd function in v_x. The distribution function is an even function in v_x. Now that we are left with an equation entirely consisting of E_{x1} terms, we arrive at the dispersion relation.

$$k^2c^2 - \omega^2 + \sum_\alpha \omega_{p\alpha}^2 + \sum_\alpha \omega_{p\alpha}^2\int d^3\mathbf{v}\frac{kv_x^2\partial f_{\alpha 0}/\partial v_y}{kv_y - \omega} = 0 \tag{D.10}$$

We will examine the integral for a particular species, and thus drop the α subscripts. The integral can be cleaned up by using integration by parts, and then separated into three integrals, I_x, I_y, and I_z.

$$\int d^3\mathbf{v} \frac{k v_x^2 \partial f_{\alpha 0}/\partial v_y}{k v_y - \omega} = \int d^3\mathbf{v} \frac{v_x^2 f_{\alpha 0}}{(v_y - \omega/k)^2} = I_x I_y I_z \tag{D.11}$$

For a standard double Maxwellian particle distribution,

$$f = \left(\frac{m}{2\pi T_x}\right)^{1/2} \left(\frac{m}{2\pi T}\right) \exp\left[-\frac{m}{2T_x} v_x^2 - \frac{m}{2T}\left(v_y^2 + v_z^2\right)\right]. \tag{D.12}$$

At this point we have made the assumption that the $\mathbf{k}$ of the system is perpendicular to the direction of the anisotropy. We can substitute the distribution function from Equation (D.12) into Equation (D.11) and thus generate each of the integrals.

$$I_x = \int dv_x v_x^2 \left(\frac{m}{2\pi T_x}\right)^{1/2} \exp\left(-\frac{mv}{2T_x} v_x^2\right) = \frac{T_x}{m} \tag{D.13}$$

$$I_y = \int dv_y \left(\frac{m}{2\pi T}\right)^{1/2} \frac{1}{(v_y - \omega/k)^2} \exp\left(-\frac{m}{2T} v_y^2\right) = -\frac{m}{T}\left[1 + \xi\, \mathrm{Z}\left(\xi\right)\right] \tag{D.14}$$

$$I_z = \int dv_z \left(\frac{m}{2\pi T}\right)^{1/2} \exp\left(-\frac{m}{2T} v_z^2\right) = 1 \tag{D.15}$$

where

$$\xi = \frac{\omega}{k\sqrt{2T/m}}, \tag{D.16}$$

and Z is the plasma dispersion function,

$$\mathrm{Z}(\xi) = \frac{1}{\sqrt{\pi}} \int_{-\infty}^{\infty} \frac{\exp(-x^2) dx}{x - \xi}. \tag{D.17}$$

Note that the temperature in the $\hat{\mathbf{z}}$ direction does not show up in the integrated solution. The instability generated by the difference in temperature between the $\mathbf{k}$ direction and the enhanced temperature direction. If $\mathbf{k}$ were in the enhanced

temperature direction, $T_{\alpha z}$ would equal $T_{\alpha x}$, and we could do the same analysis but with $T_{\alpha x} < T_\alpha$.

We can now substitute our calculated integral into Equation (D.10).

$$k^2c^2 - \omega^2 + \sum_\alpha \omega_{p\alpha}^2 \left(1 - \frac{T_{\alpha x}}{T_\alpha}\right) - \sum_\alpha \omega_{p\alpha}^2 \frac{T_{\alpha x}}{T_\alpha} \xi_\alpha \, \mathrm{Z}\left(\xi_\alpha\right) = 0 \tag{D.18}$$

When $T_{\alpha x}$ is large enough compared to T_α, ω^2 becomes negative generating an unstable mode. The terms involving ξ_α also depend on ω, which makes it more difficult to determine when the system is unstable. It turns out that by using the Penrose criterion for stability, we can find that the mode is unstable when

$$\frac{T_{ex}}{T_e} - 1 > \frac{k^2c^2}{\omega_{pe}^2}. \tag{D.19}$$

The electron temperature dominates because $\omega_{pe} \gg \omega_{pi}$. For a temperature anisotropy with $T_{ex} > T_e$ and $\mathbf{k}$ perpendicular to the anisotropy, the Weibel instability can form. On the other hand, if $T_{ex} < T_e$, or equivalently $\mathbf{k}$ is parallel to the enhanced temperature, the system is stable. The Weibel instability is thus expected to occur with $\mathbf{k}$ perpendicular to the enhanced temperature direction. To calculate the growth rate of the Weibel instability, Equation (D.18) can be solved numerically.

Bibliography

[1] A. Akasofu. Auroral substorms: Paradigm shifts in research. *EOS*, 91(31):1, 2010.

[2] Steven A. Balbus and John F. Hawley. A powerful local shear instability in weakly magnetized disks. I. Linear analysis. *The Astrophysical Journal*, 376:214, 1991.

[3] S. D. Bale, J. C. Kasper, G. G. Howes, E. Quataert, C. Salem, and D. Sundkvist. Magnetic fluctuation power near proton temperature anisotropy instability thresholds in the solar wind. *Phys. Rev. Lett.*, 103(21):211101, Nov 2009.

[4] K. W. Behannon, L. F. Burlaga, J. T. Hoeksema, and L. W. Klein. Spatial variation and evolution of heliospheric sector structure. *J. Geophys. Res.*, 94:1245–1260, 1989.

[5] Ludwig Biermann and Arnulf Schlüter. Cosmic radiation and cosmic magnetic fields. ii. origin of cosmic magnetic fields. *Phys. Rev.*, 82:863–868, Jun 1951.

[6] J. Birn. Geospace environmental modeling (GEM) magnetic reconnection challenge. *J. Geophys. Res.*, 106:3715, 1999.

[7] M. Brittnacher, K. B. Quest, and H. Karimabadi. A new approach to the linear theory of single-species tearing in two-dimensional quasi-neutral sheets. *J. Geophys. Res.*, 100(A3):3551–3562, 1995.

[8] L. F. Burlaga, N. F. Ness, and M. H. Acuna. Magnetic fields in the heliosheath and distant heliosphere: Voyager 1 and 2 observations during 2005 and 2006. *Astrophys. J.*, 668:1246–1258, 2007.

[9] L. F. Burlaga, N. F. Ness, M. H. Acua, J. D. Richardson, E. Stone, and F. B. McDonald. Observations of the heliosheath and solar wind near the termination shock by Voyager 2. *The Astrophysical Journal*, 692(2):1125, 2009.

[10] P. Cassak, M. A. Shay, and J. F. Drake. A catastrophe model for the onset of fast reconnection. *Phys. Rev. Lett.*, 95:235002, 2005.

[11] A. Czechowski, S. Grzedzielski, and M. Strumik. Fermi I electron acceleration by magnetic reconnection exhausts on closely stacked current sheets near the heliopause. *AIP Conf. Proc.*, 1216:588, 2010. Twelfth International Solar Wind Conference.

[12] W. Daughton, H. Karimabadi, and J. Scudder. Fully kinetic simulations of undriven magnetic reconnection with open boundary conditions. *Phys. Plasmas*, 13:072101, 2006.

[13] Charles Day. Spacecraft probes the site of magnetic reconnection in earth's magnetotail. *Physics Today*, 54:16.

[14] J. F. Drake, H. Che, M. A. Shay, and M. Swisdak. Electron acceleration from contracting magnetic islands during reconnection. *Nature*, 443:553, 2006.

[15] J. F. Drake, M. Opher, M. Swisdak, and J. N. Chamoun. A magnetic reconnection mechanism for the generation of anomalous cosmic rays. *Astrophys. J.*, 709:963, 2010.

[16] J. F. Drake, M. Swisdak, K. M. Schoeffler, B. N. Rogers, and S. Kobayashi. Formation of secondary islands during magnetic reconnection. *Geophys. Res. Lett.*, 33:L13105, 2006.

[17] J. W. Dungey. Interplanetary magnetic field and the auroral zones. *Phys. Rev. Lett.*, 6, 1961.

[18] H. P. Furth, J. Killeen, and M. N. Rosenbluth. Finite-resistivity instabilities of a sheet pinch. *Phys. Fluids*, 6(4):459, April 1963.

[19] E. G. Harris. On a plasma sheet separating regions of oppositely directed magnetic field. *Nuovo Cim.*, 23:115, 1962.

[20] A. Hasegawa. Drift mirror instability in the magnetosphere. *Phys. Fluids*, 12:2642, 1969.

[21] Petr Hellinger, Pavel Travnicek, Justin C. Kasper, and Alan J. Lazarus. Solar wind proton temperature anisotropy: Linear theory and wind/swe observations. *Geophys. Res. Lett.*, 33:L09101, 2006.

[22] J. D. Huba. NRL plasma formulary, 2006.

[23] Homa Karimabadi, William Daughton, and Kevin B. Quest. Physics of saturation of collisionless tearing mode as a function of guide field. *J. Geophys. Res.*, 110(A03214):1–15, 2005.

[24] K. Knizhnik, J. F. Drake, and M. Swisdak. The acceleration of ions in solar flares during magnetic reconnection. *Astrophys. J.*, 743:L35, 2011.

[25] N.A. Krall and A.W. Trivelpiece. *Principles of plasma physics*. San Francisco Press, 1986.

[26] Stamatios M. Krimigis, Edmond. C Roelof, Robert B. Decker, and Matthew E. Hill. Zero outward flow velocity for plasma in a heliosheath transition layer. *Nature*, 474:361, 2011.

[27] A. Lazarian and M. Opher. A model of acceleration of anomalous cosmic rays by reconnection in the heliosheath. *Astrophys. J.*, 703:8–21, 2009.

[28] R. P. Lin et al. RHESSI observations of particle acceleration and energy release in an intense solar gamma-ray line flare. *ApJ*, 595:L69–L76, 2003.

[29] Wei Liu, Vahe' Petrosian, Brian R. Dennis, and Yan Wei Jiang. Double coronal hard and soft x-ray source observed by RHESSI: evidence for magnetic reconnection and particle acceleration in solar flares. *The Astrophysical Journal*, 676:704, 2008.

[30] Yi-Hsin Liu, M. Swisdak, and J. F. Drake. The Weibel instability inside the electron-positron Harris sheet. *Phys. of Plasmas*, 16(042101):1–10, 2009.

[31] N. F. Loureiro, A. A. Schekochihin, and S.C. Cowley. Instability of current sheets and formation of plasmoid chains. *Phys. Plasmas*, 14:100703, 2007.

[32] San Lu, Quanming Lu, Xi Shao, Peter H. Yoon, and Shui Wang. Weibel instability and structures of magnetic island in anti-parallel collisionless magnetic reconnection. *Phys. of Plasmas*, 18:072105, 2011.

[33] S. Markidis, P. Henri, G. Lapenta, A. Divin, M. V. Goldman, D. Newman, and S. Eriksson. Collisionless magnetic reconnection in a plasmoid chain. *Nonlinear Processes in Geophysics*, 19(1):145–153, 2012.

[34] A. Masters, J. P. Eastwood, M. Swisdak, M. F. Thomsen, C. T. Russell, N. Sergis, F. J. Crary, M. K. Dougherty, A. J. Coates, and S. M. Krimigis. The importance of plasma β conditions for magnetic reconnection at saturn's magnetopause. *Geophys. Res. Lett.*, 39:L08103, 2012.

[35] D. E. McKenzie and S. L. Savage. Quantitative examination of supra-arcade downflows in eruptive solar flares. *Astrophys. J.*, 697:1569–2009, 2009.

[36] Kazumi Nishimuta, S. Peter Gary, Hui Li, and Sirling A. Colgate. Magnetic reconnection in a force-free plasma: Simulations of micro- and macroinstabilities. *Phys. of Plas.*, 10(2):347.

[37] M. Øieroset, R. P. Lin, T. D. Phan, D. E. Larson, and S. D. Bale. Evidence for electron acceleration up to 300keV in the magnetic reconnection diffusion region in the earth's magnetotail. *Phys. Rev. Lett.*, 89:195001–1–4, 2002.

[38] M. Oka, T.-D. Phan, S. Krucker, M. Fujimoto, and I. Shinohara. Electron acceleration by multi-island coalescence. *arXiv*, 2010.

[39] National Research Council (U.S.). Committee on Solar and Space Physics. *Exploration Of The Outer Heliosphere And The Local Interstellar Medium: A Workshop Report*. National Academies Press, 2004.

[40] M. Opher, F. Alouani Bibi, G. Toth, J. D. Richardson, V. V. Izmodenov, and T. I. Gombosi. A strong, highly-tilted interstellar magnetic field near the solar system. *Nature*, 462:1036, 2009.

[41] M. Opher, J. F. Drake, M. Swisdak, K. M. Schoeffler, J. D. Richardson, R. B. Decker, and G. Toth. Is the magnetic field in the heliosheath laminar or a turbulent bath of bubbles? *Astrophys. J.*, 734:71, 2011.

[42] E. N. Parker. Sweet's mechanism for merging magnetic fields in conducting fluids. *J. Geophys. Res.*, 62:509, 1957.

[43] E. N. Parker. Dynamics of the interplanetary gas and magnetic fields. *Astrophys. J.*, 128:664, 1958.

[44] H. E. Petschek. Magnetic field annihilation. In W. N. Ness, editor, *AAS/NASA Symposium on the Physics of Solar Flares*, page 425. NASA, Washington, DC, 1964.

[45] T. D. Phan, J. T. Gosling, M. S. Davis, R. M. Skoug, M. Øieroset, R. P. Lin, R. P. Lepping, D. J. McComas, C. W. Smith, H. Reme, and A. Balogh. A magnetic reconnection x-line extending more than 390 earth radii in the solar wind. *Nature*, 439:175, 2006.

[46] P. L. Pritchett. Onset and saturation of guide-field magnetic reconnection. *Phys. of Plas.*, 12:062301, 2005.

[47] J. D. Richardson, J. C. Kasper, J. W. Belcher, and A. J. Lazarus. Cool heliosheath plasma and deceleration of the upstream solar wind at the termination shock. *Nature*, 454:63, 2008.

[48] C. T. Russell and R. C. Elphic. Icee observations of flux transfer events at the dayside magnetopause. *Geophys. Res. Lett.*, 6:33, 1979.

[49] R. Samtaney, N. F. Loureiro, D. A. Uzdensky, A. A. Schekochihin, and S. C. Cowley. Formation of plasmoid chains in magnetic reconnection. *Phys. Rev. Lett.*, 103:105004, 2009.

[50] Takayoshi Sano, Shu-ichiro Inutsuka, Neal J. Turner, and James M. Stone. Angular momentum transport by magnetohydrodynamic turbulence in accretion disks: Gas pressure dependence of the saturation level of the magnetorotational instability. *Astrophys. J.*, 605:321–339, 2004.

[51] Sabrina L. Savage, David E. McKenzie, and Katharine K. Reeves. Reinterpretation of supra-arcade downflows in solar flares. *Astrophys. J. Lett.*, 747:L40, 2012.

[52] K. M. Schoeffler, J. F. Drake, and M. Swisdak. The effects of plasma beta and anisotropy instabilities on the dynamics of reconnecting magnetic fields in the heliosheath. *Astrophys. J.*, 743:70, 2011.

[53] K. M. Schoeffler, J. F. Drake, and M. Swisdak. Scaling of the growth rate of magnetic islands in the heliosheath. *Astrophys. J. Lett.*, 750:L30, 2012.

[54] R. Schreier, M. Swisdak, J. F. Drake, and P. A. Cassak. Three-dimensional simulations of the orientation and structure of reconnection x-lines. *Phys. of Plas.*, 17:110704, 2010.

[55] P. Sharma, G. Hammett, E. Quataert, and J. Stone. Shearing box simulations of the mri in a collisionless plasma. *Astrophys. J.*, 637:952–967, 2006.

[56] M. A. Shay, J. F. Drake, B. N. Rogers, and R. E. Denton. The scaling of collisionless, magnetic reconnection for large systems. *Geophys. Res. Lett.*, 26:2163, 1999.

[57] M. A. Shay, J. F. Drake, and M. Swisdak. Two-scale structure of the electron dissipation region during collisionless magnetic reconnection. *Phys. Rev. Lett.*, 99:155002, 2007.

[58] M. A. Shay, J. F. Drake, M. Swisdak, W. Dorland, and B. N. Rogers. Inherently three-dimensional magnetic reconnection: A mechanism for bursty bulk flows? *Geophys. Res. Lett.*, 30(6):1345, doi:10.1029/2002GL016267, 2003.

[59] N. R. Sheeley, H. P. Warren, and Y.-M. Wang. The origin of postflare loops. *Astrophys. J.*, 616:1224, 2004.

[60] L. S. Shepherd and P. A. Cassak. Comparison of secondary islands in collisional reconnection to hall reconnection. *Phys. Rev. Lett.*, 105:015004, Jul 2010.

[61] Jacob B. Simon, John F. Hawley, and Kris Beckwith. Simulations of magnetorotational turbulence with a higher-order Godunov scheme. *Astrophys. J. Lett.*, 690:974, 2009.

[62] Lorenzo Sironi and Anatoly Spitkovsky. Acceleration of particles at the termination shock of a relativistic striped wind. *The Astrophysical Journal*, 741(1), 2011.

[63] J. A. Slavin, M. F. Smith, E. L. Mazur, D. N. Baker, E. W. Hones, Jr., T. Iyemori, and E. W. Greenstadt. ISEE 3 observations of traveling compression regions in the Earth's magnetotail. *J. Geophys. Res.*, 98(A9):15425–15446, 1993.

[64] Edward J. Smith. The heliospheric current sheet. *J. Geophys. Res.*, 106(A8):15,819–15,831, 2001.

[65] E. C. Stone, A. C. Cummings, F. B. McDonald, B. C. Heikkila, N. Lal, , and W. R. Webber. Voyager 1 explores the termination shock region and the heliosheath beyond. *Science*, 309:2017–2020, 2005.

[66] P. A. Sweet. The neutral point theory of solar flares. In B. Lehnert, editor, *Electromagnetic Phenomena in Cosmical Physics*, page 123. Cambridge University Press, New York, 1958.

[67] Erich S. Weibel. Stable orbits of charged particles in an oscillating electromagnetic field. *Phys. Rev.*, 114(1):18–21, Apr 1959.

[68] P. Wu, D. Winske, S. P. Gary, N. A. Schwadron, and M. A. Lee. Energy dissipation and ion heating at the heliospheric termination shock. *J. Geophys. Res.*, 114:A08103, 2009.

[69] Masaaki Yamada. Progress in understanding magnetic reconnection in laboratory and space astrophysical plasmas. *Phys. Plasmas*, 14:058102, 2007.

[70] G. P. Zank. Interaction of the solar wind with the local interstellar medium: a theoretical perspective. *Space Science Reviews*, 89:413–688, 1999.